מכון ויצמן למדע
WEIZMANN INSTITUTE OF SCIENCE

עבודת גמר (תזה) לתואר
דוקטור לפילוסופיה

מוגשת למועצה המדעית של
מכון ויצמן למדע
רחובות, ישראל

Thesis for the degree
Doctor of Philosophy

Submitted to the Scientific Council of the
Weizmann Institute of Science
Rehovot, Israel

"במתכונת "רגילה
In a "Regular" Format

מאת
מקסים נגליס

By
Maxim Naglis

היווצרות Φ מזון בהתנגשויות של p+p, d+Au ו- Au+Au בעזרת הגלאי PHENIX ב- RHIC

Φ meson production in p+p, d+Au and Au+Au collisions at RHIC using the PHENIX detector

מנחה: יצחק צרויה

Advisor: Itzhak Tserruya

כסלו תש"ע

November 2009

Dedication

I would like to dedicate this thesis to my parents, for instilling a curiosity for science and learning and to my wife Anna, for encouraging me and convincing me to believe in myself and for her patience and tolerance for everything I do.

Acknowledgments

The work presented in this thesis has been carried out within the PHENIX collaboration, during my period as a Ph.D. student at the Department of Particle Physics, Weizmann Institute of Science, from 2004 to 2009. I wish to express my dearest thanks and gratitude to all those who helped make this dissertation possible.

First I would like to thank my thesis supervisor Prof. Itzhak Tserruya for his invaluable guidance, support and for all the opportunities he has provided over the years of my Ph.D. studies. His encouragement, critical remarks and guidance were essential for the successful completing of this work.

I am sincerely thankful to Prof. Zeev Fraenkel for his constructive comments and encouragement. I also like to express my gratitude to Dr. Ilia Ravinovich for his dedication and extensive help during the HBD R&D, construction and commissioning. I appreciate Lev Shekhtman who shared his insight and expertise in handling and operating GEM detectors. I would like to extend my thanks to Alexander Kozlov, Alexander Cherlin, Anand Kumar Dubey and Deepali Sharma for many lovely discussions (not only about science) and a broad spectrum of help and support with daily tasks and issues in the laboratory.

I am very thankful to Sasha Milov, Victor Riabov and Yuri Riabov for the pleasure of working with them, their significant help on the ϕ meson analysis and for the really friendly relations.

Thanks also go to Prof. Michael Hass and Prof. Ehud Duchovni for their attention to my work, feedbacks and encouragement at the "milestones" along the way.

I would like to acknowledge the support by the Israel Science Foundation, the MINERVA Foundation and the Nella and Leon Benoziyo Center of High Energy Physics Research.

Many thanks to my friends Alexey, Vasily, Timur, Marija and Larik for the great time we spent together.

And a special thank you to my wife Anna, my parents Alexey and Olga and to my brother Artem, who have given me their love and support throughout my graduate studies.

Abstract

This thesis comprises two parts. The first part details the measurements of ϕ meson production in the K^+K^- decay channel in p+p, d+Au and Au+Au collisions at $\sqrt{s_{NN}} = 200$ GeV using the PHENIX detector at the Relativistic Heavy-Ion Collider (RHIC). The second part presents a report on the Hadron Blind Detector (HBD) upgrade project for the PHENIX experiment at RHIC.

The suppression of hadrons with high transverse momentum in ultra-relativistic heavy ion collisions with respect to expectations from scaled p+p results is one of the most interesting findings at RHIC. A clear difference between the suppression patterns of baryons (p, $\Lambda(1115)$) and light mesons (π, η) is observed in the intermediate p_T range suggesting that the suppression is governed by the number of valence quarks rather than the mass of the hadron. The ϕ meson, which is as heavy as the proton and $\Lambda(1115)$ baryon, but carrying two quarks, differentiates between hadron mass and number of constituent quark effects. Moreover, being an almost pure $s\bar{s}$ state, it provides insight on the effects of the constituent quark flavour and mass on the suppression pattern.

The ϕ meson production is studied using three different techniques involving different levels of kaon identification, which have very different sources of systematic uncertainties and therefore provide a valuable consistency check. Moreover, the concurrent use of these techniques allows to extent the measurements over a wide p_T range from 0.9 GeV/c to 7.0 GeV/c in $p+p$, 1.45 GeV/c to 5.1 GeV/c in d+Au and 1.1 GeV/c to 7.0 GeV/c in Au+Au.

This thesis presents results on ϕ meson production in p+p, d+Au and Au+Au collisions at $\sqrt{s_{NN}} = 200$ GeV including transverse momentum spectra, ϕ meson rapidity density dN/dy and nuclear modification factors R_{dA}, R_{AA} and R_{CP}, studied as a function of centrality. The $\phi \rightarrow K^+K^-$ meson dN/dy values in p+p and Au+Au collisions are compared with results obtained in the $\phi \rightarrow e^+e^-$ decay channel. The results in both decay channels are in agreement although the dielectron results have large errors. The relative enhancement of the ϕ meson production in Au+Au with respect to p+p changes from ~ 1.7

in peripheral to ~ 4 in central collisions. The R_{dA} and R_{AA} are studied in comparison with other particles. The amount of suppression for the ϕ meson in Au+Au collisions is found to be smaller than for π^0 and η mesons and larger than for baryons in the intermediate p_T region ($1 < p_T < 4.5$ GeV/c) suggesting a quark flavor/mass dependence of the hadron suppression. The ϕ meson R_{dA} in minimum bias d+Au is consistent with unity and agrees better with the R_{dA} of other mesons than with that of the proton. The effect of collision geometry on the ϕ meson production is studied by comparing the R_{AA} in Au+Au and Cu+Cu collisions at the same energy. The results indicate that the ϕ meson production in A+A collisions depends mainly on the number of participating nucleons N_{part}, i.e. the system size.

The HBD is a novel windowless Čerenkov detector, that was built as upgrade of the PHENIX detector. Its primary purpose is to tag electrons originating from π^0 Dalitz decays and photon conversions by their small opening angle in the field free region surrounding the collision vertex. This upgrade brings a new qualitative dimension to the measurement of electron-positron pairs from the decays of the light vector mesons ρ, ω and ϕ and the low-mass pair continuum ($m_{e^+e^-} < 1$ GeV/c^2). A description of the HBD concept, a summary of the comprehensive R&D program that was carried out to demonstrate the concept validity, and a description of the mechanical design and construction procedures of the detector are presented along with the first results obtained from the HBD. Preliminary results obtained so far reveal performance comparable to that anticipated: we observe 20 photoelectrons per incident electron traversing the HBD, single electron efficiency close to 90% and significant improvement in the signal-to-background ratio for the measurements of the low-mass e^+e^- continuum.

Contents

List of Figures

Chapter 1

Introduction

The important thing in science is not so much to obtain new facts as to discover new ways of thinking about them.

WILLIAM LAWRENCE BRAGG

1.1 Quarks, gluons and quark-gluon plasma

In 1961 Gell-Mann [1] and Ne'eman [2] independently introduced a hadron classification scheme based on the $SU(3)$ symmetry. The scheme allowed to systematize the wealth of by then discovered baryons and mesons and was predictive as well as descriptive. Few years later, in 1964 the quark model was proposed independently by Gell-Mann [3] and Zweig [4]. The model postulated the existence of three types of spin 1/2 quarks: **u**, **d** and **s** with electric charges +2/3, -1/3 and -1/3, respectively. In this model baryons (antibaryons) are made up of three quarks (antiquarks) and mesons consist of a quark and an antiquark[1]. Inelastic electron-nucleon scattering results, and results from neutrino-scaterring, demonstrated that indeed the constituent quarks are fermions carrying a fractional electric charge of either +2/3 or -1/3.

The discovery of baryons containing three identical quarks and therefore violating the Pauli exclusion principle led to the introduction of a new quantum number, the color charge, to the model. A quark's color can take one of three values, called red, green, and blue. An antiquark can take one of three anticolors, called antired, antigreen, and antiblue. A baryon consists of a red, a green and a blue quark to form a colour-neutral (white) particle, while a meson is composed of a color and its anti-color quark-antiquark pair, also giving a net colour of white. Only color-neutral particles are observed in nature.

[1] Later the quark model was extended with the discoveries of **c** [5, 6], **b** [7] and **t** [8, 9] quarks.

The quarks interact strongly by exchanging massless gluons. There are eight spin-1 gluons which carry color charge [10]. As gluons carry a color charge themselves, they can also interact with each other. The first direct experimental evidence of gluons was found in 1979 when three-jet events were observed at the electron-positron collider PETRA at DESY[11].

The quark structure of the hadrons became the generally accepted view by the end of the 1970's. The field theory describing the strong interaction of quarks and gluons is called Quantum Chromodynamics (QCD). QCD successfully describes two extreme scenarios in a unified treatment:

1. At short distances or large momentum transfer, Q, the strong interaction coupling constant α_s decreases logarithmically, i.e. quarks and gluons are weakly coupled:

$$\alpha_s(Q^2) \approx \frac{1}{b\ln(Q^2/\Lambda^2_{QCD})} \xrightarrow[Q^2\to\infty]{} 0, \tag{1.1}$$

   where Q is the quark momentum transfer, Λ_{QCD} is a renormalization scale factor (energy scale $Q^2 \approx \Lambda^2_{QCD}$ where α_s diverges to infinity) and b is a constant that depends on the number of active quark flavours. This property is known as asymptotic freedom[1]. At sufficiently high Q (hard processes), the coupling strength is weak enough for perturbative QCD to be computationally valid.

2. At large distances or small Q (soft processes), the coupling constant α_s gets stronger thereby resulting in the phenomena of quark confinement. Soft processes can not be described by perturbative QCD and are usually treated by lattice QCD (lQCD) calculations, where the theory is formulated on a discrete lattice of space-time points.

Under extreme conditions of energy density, lattice QCD calculations [12] predict a phase transition from ordinary hadronic matter to a deconfined state known as the quark-gluon plasma (QGP) [13]. Fig. 1.1 shows lQCD results on thermodynamic variables such as the energy density (ε) and pressure (p) calculated as a function of temperature (T) for different numbers of active quark flavors. Both, the energy density and the pressure dependence on temperature clearly reveal a stepwise increase at a critical temperature $T_c \sim 170$ MeV. The Stefan-Boltzmann ideal gas limit for each case, also shown in Fig. 1.1 is found to be above the values calculated in the lattice indicating that the QGP can not be considered as a free gas of weakly interacting gas of quarks and gluons at $T \approx T_c$ [12].

In the deconfined state quarks and gluons are no longer bound to hadrons, they can move freely inside the volume occupied by the deconfined matter, much larger than the

[1] Gross, Wilczek and Politzer won the 2004 Nobel prize in Physics "for the discovery of asymptotic freedom in the theory of the strong interaction".

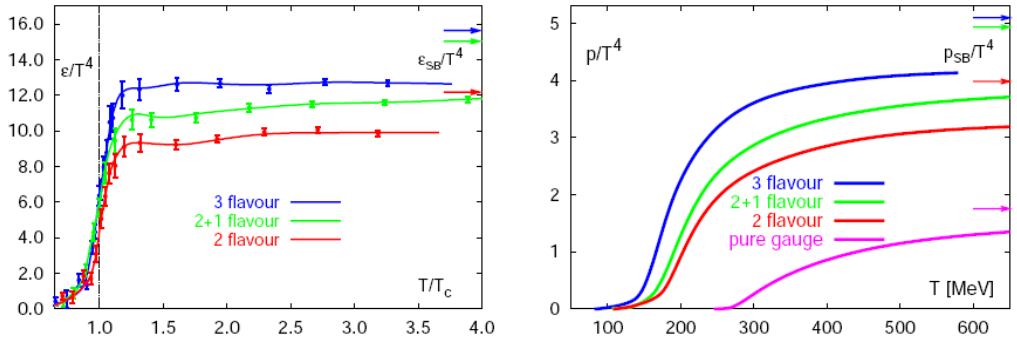

Figure 1.1: Lattice QCD results: energy density as function of T/T_c (left) and pressure as function of temperature (right), both scaled by T^4, for different numbers of active quark flavors [12]. Arrows indicate the Stefan-Boltzmann ideal gas limits for each case.

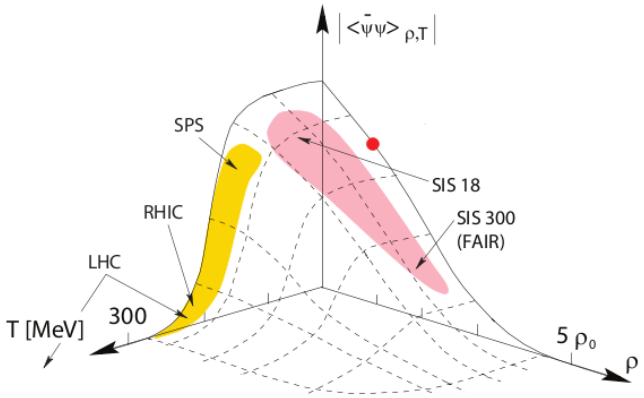

Figure 1.2: Dependence of the quark condensate on temperature T and nuclear density ρ [14]. The location of normal nuclear matter is shown with the red dot.

volume of a hadron.

In addition to the phase transition to a deconfined phase, numerical simulations of QCD on the lattice also predict the restoration of chiral symmetry (CSR). In the QCD ground state (vacuum) chiral symmetry is spontaneously broken by a quark-antiquark condensate $\langle\bar{\psi}\psi\rangle \neq 0$. A quark traversing the vacuum interacts with the quark condensate. This interaction is considered as the most likely reason for the origin of the constituent quark masses of the order of 300 MeV, as opposed to the current mass of the light **u**, **d** quarks which is ∼5-10 MeV. As the density and/or temperature of matter increases, the quark condensate becomes closer to zero as depicted in Fig. 1.2, and in the limit of zero current quark mass, chiral symmetry is restored. It is not clear whether there are two distinct phase transitions, leading to deconfinement and to chiral symmetry restoration, which occur at similar conditions of temperature and density or there is only one phase transition.

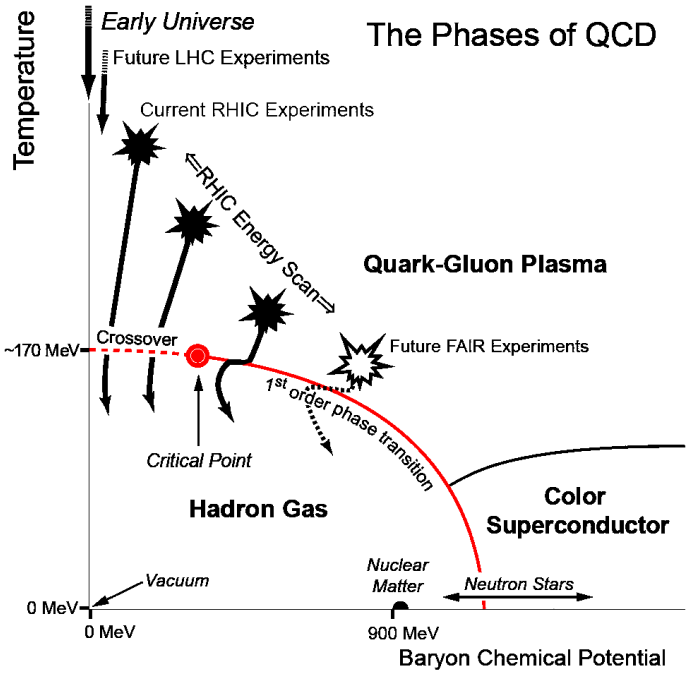

Figure 1.3: A contemporary view of the QCD phase diagram [15].

A contemporary view of the QCD phase diagram is shown in Fig. 1.3. The vertical axis in the figure is the temperature, and the horizontal axis represents the baryon chemical potential, μ_B, which determines the energy required to add or remove a baryon at fixed pressure and temperature and reflects the net baryon density of the matter. Below the phase boundary (shown in red) the matter is confined in the form of a hadron gas, and above the phase boundary, the matter is in the QGP phase. Conjectures about the regions probed by existing and future accelerators are indicated. The nature of the phase transition is unknown. The lattice QCD predictions crucially depend on the values of the quark masses and on the number of active quark flavours included in the calculation. For the most realistic calculations [16, 17], incorporating three non-degenerate quarks (the two light **u** and **d** quarks the heavier strange quark **s**) with masses relevant on the scale of the critical temperature, T_c, the transition seems to be of the crossover type for values of the baryon chemical potential μ_B below 400 MeV and of first order above, with a critical point separating them.

The observation of deconfinement and chiral symmetry restoration, and the study of the dynamics of the deconfined phase have important consequences, both for the understanding of QCD and also for cosmology. It is believed that QGP was the state that existed in the early universe some $\sim$10 μs after the Big Bang. The energy density of interest is about 2-3 GeV/fm^3. It can be reached by heating matter to a temperature of about $T_c \approx$170 MeV at zero baryon density, or by compressing cold nuclear matter to baryon

densities in the range $5 \cdot \rho_0 < \rho_c < 10 \cdot \rho_0$, where $\rho_0 \sim 0.15$ GeV/fm^3 is the density of matter in the ground state, or by combination of heating and compression. Relativistic heavy ion collisions provide a unique opportunity to create the conditions for QGP formation in the laboratory.

1.2 Relativistic heavy-ion collisions

A relativistic heavy-ion (RHI) collision is a complex process. One distinguishes several stages along the collision: pre-equilibrium, thermal and chemical equilibrium of partons, formation of QGP (hereinafter we assume that the energy density created in the collision reaches the critical value necessary for quark-gluon plasma formation), QGP-hadron gas mixed phase, a gas of hot interacting hadrons, and finally, a freeze-out state when the produced hadrons no longer interact with each other. The space-time evolution of a heavy-ion collision is depicted in Fig. 1.4. The times and temperatures for the different phases are taken from [18].

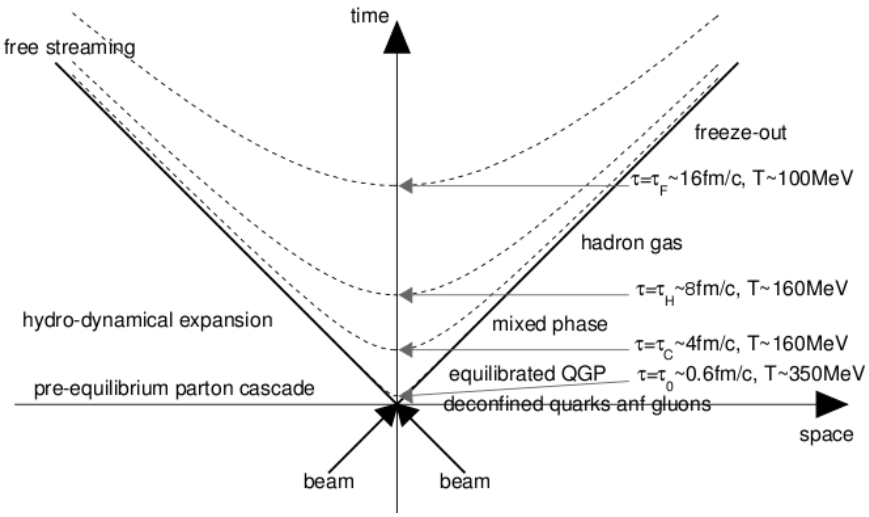

Figure 1.4: Space-time evolution of a nucleus-nucleus collision [19].

In the pre-equilibrium phase the dynamics of partonic matter can be described as a cascade of freely colliding partons. If the system is long-lived enough to become both in thermal and chemical equilibrium then such system is commonly referred to as the quark-gluon plasma ($\tau = \tau_0$). The QGP evolution is usually modelled according to relativistic hydrodynamics. After the QGP is formed, the system expands and cools down. At $\tau = \tau_c$, as the system reaches the critical temperature T_c, hadronization takes place. The system then enters into a mixed phase where the phase transition from deconfined to confined

matter occurs. When all of the QGP has converted into hadrons ($\tau = \tau_h$), the hadron gas expands and cools till the freeze-out temperature ($\tau = \tau_f$) is reached. The hadrons cease to interact and stream out of the collision region at freeze-out temperature.

1.3 Experimental observables

A comprehensive review of the experimental observables and the current status of the experimental RHI physics falls out of the scope of this thesis. In this section the discussion is limited to the topics that are most relevant to this thesis.

1.3.1 Strangeness enhancement

The strangeness content of the colliding nuclei is negligible, consequently all measured strange particles must have been produced during the collision. The enhancement of strangeness production was proposed as one of the possible signatures of QGP formation [20–22]. The high parton density and the lower energy threshold for $s\bar{s}$ pair production in the quark-gluon plasma ($E_{th} = 2m_s \approx 300$ MeV) in comparison to the hadron gas ($E_{th} \gtrapprox 540$ MeV[1]) leads to an increase of strangeness production in the plasma. This expectation has been confirmed by QCD calculations on the lattice [23].

Experimentally one can study the strangeness enhancement by looking for an increase in the production of hadrons containing strangeness with increasing number of participants from proton-proton to nucleus-nucleus collisions. Experimental data, both at SPS and RHIC, shown in Fig. 1.5, confirm the theoretical expectations [24–27]. There is no enhancement observed in p+Pb collisions, while in Pb+Pb and Au+Au collisions one sees a clear enhancement of the strange and multi-strange baryon yields, which are found to increase with centrality and strangeness content. In central Au+Au collisions the Ω yield per participant is a factor of $\sim$10 higher compared to that in p+p.

The features observed in the experimental data can be interpreted using the statistical model for particle production imposing the canonical constraints of strangeness conservation in small systems [28, 29]. The model predictions agree with the beam energy dependence and the strangeness content dependence observed in the data, but fail to reproduce the absolute amounts and the centrality dependence of the enhancements. The production of strange particles provides a means to check whether chemical equilibrium is achieved in the system. If the measured strangeness yields are still lower than full equilibrium predictions, then only partial equilibrium is achieved and this partial equilib-

[1] The lowest E_{th} of approximately 540 MeV for $s\bar{s}$ pair production in a hadron gas is for $\pi + N \rightarrow \Lambda + K$ and $\pi + \bar{N} \rightarrow \bar{\Lambda} + \bar{K}$ reactions.

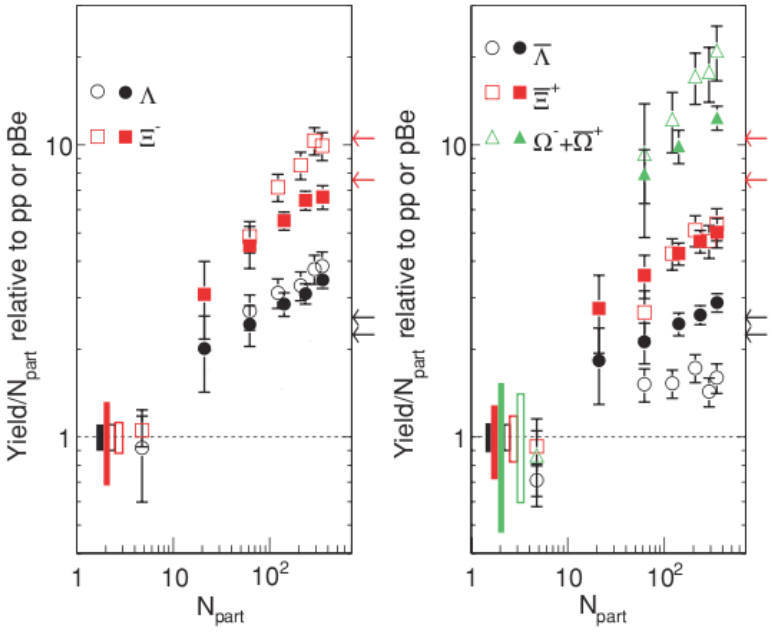

Figure 1.5: Enhancement of strange and multi-strange baryons at SPS and RHIC [24]. The solid symbols are for Au+Au at $\sqrt{s_{NN}}$=200 GeV and the open symbols are for Pb+Pb at $\sqrt{s_{NN}}$=17.3 GeV. Boxes at unity show the combined statistical and systematic uncertainties in the p+p (p+Be) data. Error bars on the data points represent those from the heavy ion data. The arrows on the right (red for Ξ, black for Λ) mark canonical model predictions, see text for details.

rium can be quantified by a multiplicative strangeness undersaturation factor γ_s for each strange quark in a hadron [30]. The γ_s factors as a function of centrality deduced from hadron multiplicities within a statistical-thermal model [31] indicate that full strangeness equilibration is reached only in central Au+Au collisions at 130 and 200 GeV.

Systematic studies of the strangeness enhancement for different particle types, beam energies and system sizes put additional constraints on the models and may help to discriminate between the different scenarios of the enhancement.

1.3.2 Chiral symmetry restoration

The dynamics of the strong interaction is governed by the QCD Lagrangian which can be expressed as:

$$\mathcal{L} = -\frac{1}{4} G^a_{\mu\nu} G^a_{\mu\nu} - \sum_n \bar{\psi}_n i \not{D} \psi_n - \sum_n m_n \bar{\psi}_n \psi_n \tag{1.2}$$

where ψ_n is the spin-$\frac{1}{2}$ quark-field of flavour n and mass m_n. The field strength tensor is $G^a_{\mu\nu} = \partial_\mu A^a_\nu - \partial_\nu A^a_\mu + g f^{abc} A^b_\mu A^c_\nu$ and the covariant derivative acting on the quark field is $i\not{D}\psi = \gamma^\mu \left(i\partial_\mu + g A^a_\mu \frac{\lambda^a}{2} \right) \psi$. Here, A^a_μ represents a gluon field with color index $a = 1, \ldots, 8$,

γ^μ are the Dirac matrices, λ^a are the Gell-Mann matrices, $g=\sqrt{4\pi\alpha_s}$ is the coupling constant of the strong interaction and f^{abc} are the structure constants of the $SU(3)$ group. The first term of the Lagrangian describes the gluon-gluon interactions, the second includes interactions between quarks and gluons, and the last term corresponds to the free quarks of masses m_n at rest. In this discussion we focus on the three light quarks flavours (**u**, **d** and **s**).

The Lagrangian is invariant under local $SU(3)$ gauge transformations, i.e. under arbitrary rotations in color space. If the masses of the quarks are equal, $m_{\rm u} = m_{\rm d} = m_{\rm s}$, then the theory is also invariant under arbitrary flavor rotations of the quark fields. If the quark masses are not just equal, but equal to zero, then the flavor symmetry is enlarged. The quark fields can be decomposed into a left- and a right-handed components $\psi_{L,R} = \frac{1}{2}(1 \pm \gamma_5)\psi$. In terms of these L/R fields the fermionic part of the Lagrangian can be rewritten as

$$\mathcal{L} = \sum_n (\bar{\psi}_L i\not{D}\psi_L + \bar{\psi}_R i\not{D}\psi_R) + \sum_n m_n(\bar{\psi}_L\psi_R + \bar{\psi}_R\psi_L), \tag{1.3}$$

and in the limit of massless quarks ($m_{\rm u}$=$m_{\rm d}$=$m_{\rm s}$=0), does not have coupling between left and right handed fields. The latter results in the invariance of the Lagrangian under independent flavor transformations of the left and right handed fields:

$$\psi_L \rightarrow e^{-i\theta_L}\psi_L \quad \text{and} \quad \psi_R \rightarrow \psi_R \tag{1.4a}$$

$$\psi_L \rightarrow \psi_L \quad \text{and} \quad \psi_R \rightarrow e^{-i\theta_R}\psi_R \tag{1.4b}$$

This chiral symmetry conserves the quark helicity[1] in the strong interactions and also makes the hadronic chiral partners degenerate in mass.

In reality, the masses of the **u**, **d** and **s** quarks are not zero. Nevertheless, since $m_{\rm u}, m_{\rm d} \ll m_{\rm s} < \Lambda_{QCD}$, the QCD Lagrangian possesses an approximate $SU(3)_L \times SU(3)_R$ chiral symmetry. However, the observation of the mass splitting of chiral partners, shown in Fig. 1.6, implies a spontaneous breaking of the chiral symmetry down to $SU(3)_V$ due to a non-vanishing vacuum expectation value of the chiral condensate $\langle\bar{\psi}\psi\rangle \neq 0$. According to the Goldstone theorem [32] the breaking of $SU(3)_L \times SU(3)_R \rightarrow SU(3)_V$ leads to the appearance of an octet of massless Goldstone bosons ($\pi^\pm$, π^0, $K^\pm$, K^0, $\bar{K^0}$, η). In turn, the $SU(3)_V$ flavor symmetry is broken explicitly by the difference between the masses of the **u**, **d** and **s** quarks, and the Goldstone bosons of the spontaneous symmetry breaking acquire a finite mass.

As the density and/or temperature of a hadronic system increase, the quark condensate "melts", and chiral symmetry gets approximately restored. The dynamics of the

[1] Helicity is the sign of the spin projection on the momentum direction, of a quark.

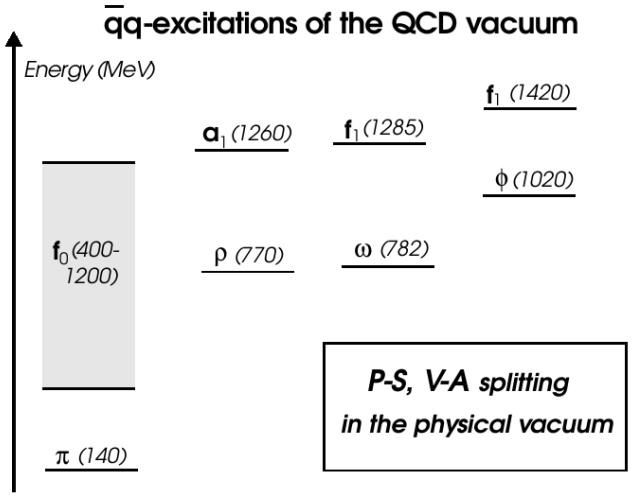

Figure 1.6: Experimentally observed spectrum of low-mass mesons [33].

breaking and partial restoration of chiral symmetry is of great interest in nuclear physics [14, 34, 35]. Unfortunately, the chiral condensate is not an observable and one needs suitable probes to explore the dependence of its magnitude on temperature and density. The change in the chiral condensate reflects a change in the vacuum and as a consequence one expects a change in the hadron spectral function. The Brown-Rho conjecture [36] of a universal scaling law of hadron masses with the quark condensate, as well as the Hatsuda-Lee prediction based on QCD sum-rules [37] of a linear decrease of vector-meson masses with baryon density provided a way to experimentally detect the approximate restoration of chiral symmetry.

In-medium modifications of the light vector mesons (ρ, ω and ϕ) spectral functions are an excellent tool to detect and study the chiral symmetry breaking/restoration transition. The ρ meson is best suited for this. Due to its much shorter lifetime (τ_ρ=1.3 fm/c) compared with typical fireball lifetimes of $\sim$10 fm/c, the ρ mesons will predominantly decay inside the fireball. As their leptonic decay is unaffected by further rescattering, the invariant mass of the lepton pair shall reflect possible modifications of the ρ spectral shape (broadening and/or shifted mass). In-medium effects are also expected for the ω and ϕ. However, since ω and ϕ have much longer lifetimes compared to ρ, only a fraction of them decays inside the fireball making their observation much more difficult. An alternative way to observe in-medium effects on the ϕ meson is to compare the branching ratio of the ϕ decays into kaon and lepton pairs. This will be further discussed in Section 1.4.

Measurements at the SPS performed by the NA45/CERES and NA60 experiments show clear evidence of in-medium modifications of the ρ meson in Pb+Au and In+In collisions at 158 AGeV/c [38, 39]. The results favor the broadening of the resonance

rather than the dropping of its mass when close to the phase boundary.

1.3.3 Nuclear modification of particle production

Before RHIC started operation it was predicted that high-p_T partons would lose energy by induced gluon radiation while traversing the hot and dense matter produced in ultra-relativistic heavy ion collisions [40–47]. This parton energy loss would manifest itself in a suppression of the high-p_T yield of hadrons produced from the fragmentation of these partons, and in a significant softening and broadening of the jets ("jet quenching"). Medium-induced effects on particle production can be quantified with the nuclear modification factor:

$$R_{AA}(p_T) = \frac{d^2N_{AA}/dydp_T}{N_{coll} \times d^2N_{pp}/dydp_T}, \tag{1.5}$$

where $d^2N_{AA}/dydp_T$ and $d^2N_{pp}/dydp_T$ are the differential yields per event in nucleus-nucleus and p+p collisions, respectively, and N_{coll} is the number of binary nucleon-nucleon collisions averaged over the impact parameter or centrality range selected in the A+A collisions. Sometimes, the ratio of central to peripheral yields, scaled by the corresponding numbers of binary nucleon-nucleon collisions, R_{CP}, is also used as a measure of the nuclear modification of particle production:

$$R_{CP}(p_T) = \frac{N_{coll}^{peripheral} \times d^2N_{AA}^{central}/dydp_T}{N_{coll}^{central} \times d^2N_{AA}^{peripheral}/dydp_T} \tag{1.6}$$

The ratio R_{CP} does not require the measurement of a p+p reference spectrum, but it is affected by possible nuclear effects in peripheral collisions. In the absence of medium-induced effects, the yield of high-p_T particles is expected to scale with N_{coll}, resulting in $R_{AA} = 1$ and $R_{CP} = 1$ at high p_T. In the low p_T region the yield is not expected to scale with N_{coll} but with N_{part} and reflects the bulk properties of the system. The p_T-scale where N_{coll} scaling holds is another physical observable which is addressed in the measurements.

One of the main discoveries at RHIC was the observation of the predicted suppression of high-p_T hadrons first in Au+Au collisions at $\sqrt{s_{NN}}$ = 130 GeV [50–52] and later at 200 GeV [53–56]. A control experiment performed in d+Au collisions at $\sqrt{s_{NN}}$ = 200 GeV showed no indication of hadron suppression [57–60]. This result together with the observation of no suppression for direct photons in Au+Au at high p_T [61, 62] ruled out initial-state and cold nuclear matter effects as being the cause for the hadron suppression observed in Au+Au collisions. Fig. 1.7 shows the R_{AA} for π^0 in central and peripheral

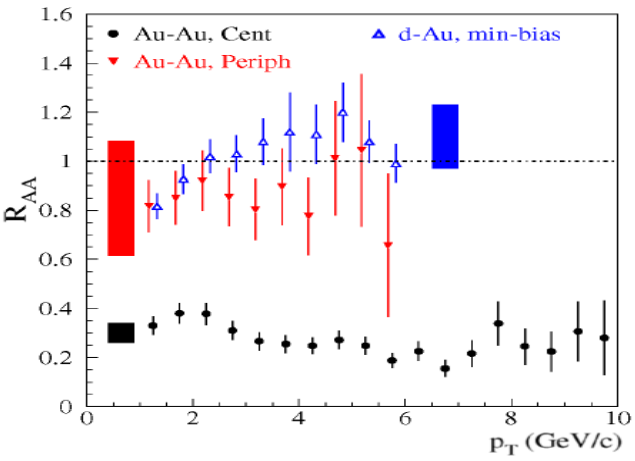

Figure 1.7: Nuclear modification factor R_{AA} as function of p_T for π^0 in central (black) and peripheral (red) Au+Au collisions and in minimum bias d+Au collisions (blue) [48].

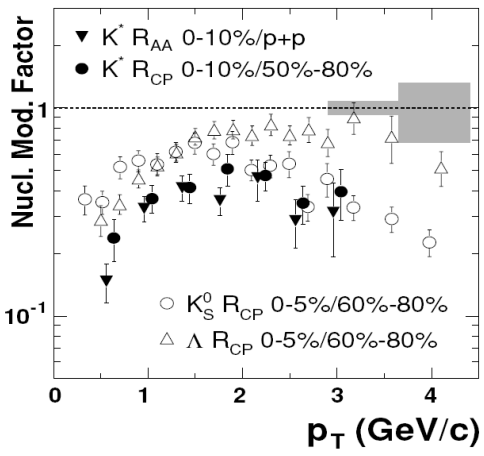

Figure 1.8: Nuclear modification factors R_{AA} and R_{CP} as function of p_T for $K(892)^*$ compared to the R_{CP} for K^0_S and Λ [49].

Au+Au collisions and in minimum bias d+Au collisions.

Surprisingly, contrary to the strong suppression of pions, protons and antiprotons were found to be enhanced at intermediate $p_T \approx 2-5$ GeV/c in Au+Au collisions [63]. Further studies of identified hadron production reveal that despite a factor of about 4 difference in mass, η mesons [64] follow the suppression pattern of neutral pions [65] over the entire p_T range of the measurements. Measurements by the STAR collaboration indicate that at higher p_T ($\gtrsim 5$ GeV/c) the nuclear modification factor of protons is getting similar to that of pions [66]. STAR also reports a separation of the R_{CP} patterns for K^0_S and $K(892)^*$ mesons from the that of Λ baryon [49, 67] shown in Fig. 1.8 (note that $m_{K(892)^*} \approx m_\Lambda$). The data suggest that particle production in the intermediate p_T range is governed by the number of valence quarks rather than the mass of the hadron.

1.4 Probing the deconfined phase with the ϕ meson

The ϕ meson was first seen in bubble chamber experiment at Brookhaven National Laboratory (BNL) in 1962 through the reactions $K^- + p \rightarrow \Lambda + \phi \rightarrow \Lambda + K^+ + K^-$ and $K^- + p \rightarrow \Lambda + \phi \rightarrow \Lambda + K^0 + \bar{K}^0$ [69]. The ϕ meson is composed of a strange quark-antiquark pair, $s\bar{s}$. The major properties of the ϕ meson and it's main decay modes are listed in Table 1.4. Being a bound state with hidden flavour, the ϕ meson production and decay obey the Okubo-Zweig-Iizuka (OZI) rule[1] [4, 70, 71]. The OZI rule implies suppression of the strong interaction when the final state can only be reached via

[1] Also known as the quark-line rule.

Quark content	$\mathbf{s\bar{s}}$
Quantum numbers, $I^G(J^{PC})$	$0^-(1^{--})$
Mass, (MeV/c^2)	$m = 1019.455 \pm 0.020$
Full width, (MeV/c^2)	$\Gamma = 4.26 \pm 0.04$
Decay mode	**Branching ratio**
K^+K^-	$(49.1 \pm 0.6)\%$
$K^0_L K^0_S$	$(34.0 \pm 0.5)\%$
$\rho\pi + \pi^+\pi^-\pi^0$	$(15.4 \pm 0.5)\%$
$\eta\gamma$	$(1.295 \pm 0.025)\%$
$\pi^0\gamma$	$(1.23 \pm 0.1)\times 10^{-3}$
e^+e^-	$(2.98 \pm 0.04)\times 10^{-4}$
$\mu^+\mu^-$	$(2.85 \pm 0.19)\times 10^{-4}$

Table 1.1: ϕ-meson properties from PDG [68].

quark-antiquark pair annihilation. Fig. 1.9 illustrates diagrams for the OZI suppressed $\phi \to \pi^+\pi^-\pi^0$ and the OZI allowed $\phi \to K^+K^-$ decays. QCD explains the OZI suppression for the $\phi \to 3\pi$ decay as follows. In the $\phi \to 3\pi$ process the initial and final state are connected by gluons. Moreover, since gluons carry color and ϕ is colorless there must be more than one gluon involved in the process to conserve all strong interaction quantum numbers. Since the ϕ meson is fairly massive ($\sim$1 GeV) the gluons must be energetic ("hard") and therefore due to asymptotic freedom, the coupling constant for each gluon will be small. Thus the amplitude for the $\phi \to \pi^+\pi^-\pi^0$ decay will be small as it depends on α_s^3. Although the amplitude for $\phi \to K^+K^-$ also involves gluon exchange, it will not be suppressed as these gluons are low energy ("soft") and therefore α_s is large here.

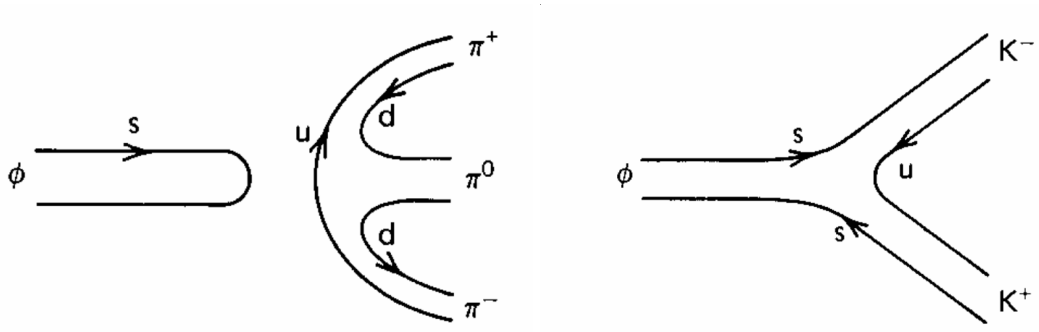

Figure 1.9: The diagrams of the $\phi \to \pi^+\pi^-\pi^0$ (left) and $\phi \to K^+K^-$ (right) decays.

The ϕ meson has a number of features that make it a valuable probe of the medium created in high energy heavy-ion collisions. As the ϕ is composed solely of $\mathbf{s}$ and $\bar{\mathbf{s}}$ quarks, its production is sensitive to the abundance of strange quarks in the system. In the dense partonic medium formed in heavy-ion collisions, strange quark pairs will be

copiously produced via gluon-gluon fusion [21, 72] (see also Section 1.3.1). During the hadronization phase, the ϕ meson can be formed via coalescence of $\mathbf{s}$ and $\bar{\mathbf{s}}$ quarks, bypassing the OZI suppression rule. Enhanced production of the ϕ meson in heavy-ion collisions was proposed as a signature of QGP formation by Shor [73].

As mentioned in Section 1.3.2, modifications of the ϕ meson spectral function could signal the restoration of chiral symmetry. The ϕ peak in the mass spectrum is well separated from the other resonances and has a narrow decay width as well, thus providing an experimentally clean signal. The fraction of primordial ϕ mesons is $\sim$100% as there are almost no feed-downs from the higher mass resonances. Moreover, the ϕ has a small cross-section with non-strange hadrons [73] and therefore it is immune to hadronic final state effects. The natural lifetime of the ϕ mesons is $\tau \approx 44$ fm/c, large compared with the lifetime of the fireball of $\sim$ 10 fm/c, but small enough for a significant fraction of them to decay inside the hot and dense interaction region. The e^+e^- and $\mu^+\mu^-$ decay channels are preferable over hadronic decay channels. The dileptons interact with the medium only electromagnetically, thus carrying clean information about the ϕ meson properties at the time of their production whereas the hadronic decay particles could be affected by final-state interactions in the medium. Experimentally a spectral shape analysis of the dilepton mass spectrum is not an easy task. Even if an excellent mass resolution of the order of one percent can be achieved, the presence of a large combinatorial background makes these measurements very challenging [74]. A more promising way to discern these effects is offered by the simultaneous measurement, within the same apparatus, of the ϕ meson yield through the e^+e^- (or $\mu^+\mu^-$) and K^+K^- decay channels. The ϕ meson mass is close to twice the kaon mass[1] and therefore the $\phi \rightarrow K^+K^-$ decay rate is very sensitive to spectral shape modifications of either the ϕ or the kaon [75, 76]. A comparison of the hadronic *vs.* leptonic branching ratios $\Gamma(\phi \rightarrow K^+K^-)/\Gamma(\phi \rightarrow e^+e^-)$ is considered as a powerful tool to probe chiral symmetry restoration.

Measurements of the nuclear modification factor of the ϕ meson can help to understand hadron production at intermediate p_T. With a mass comparable to the proton and $\Lambda(1115)$ baryon, but carrying two quarks, the ϕ meson differentiates between particle mass and number of constituent quark effects. Moreover, being an almost pure $\mathbf{s\bar{s}}$ state, it allows to study the influence of quark flavor composition on the suppression pattern. From a measurement of the ϕ meson R_{CP} by the PHENIX experiment [77] shown in Fig. 1.10, it seems that the ϕ behaves in a way more similar to the pions than to the protons. The large errors of the measurement did not allowed to draw any other conclusion.

[1] $m_\phi - 2m_K \simeq 32$ MeV.

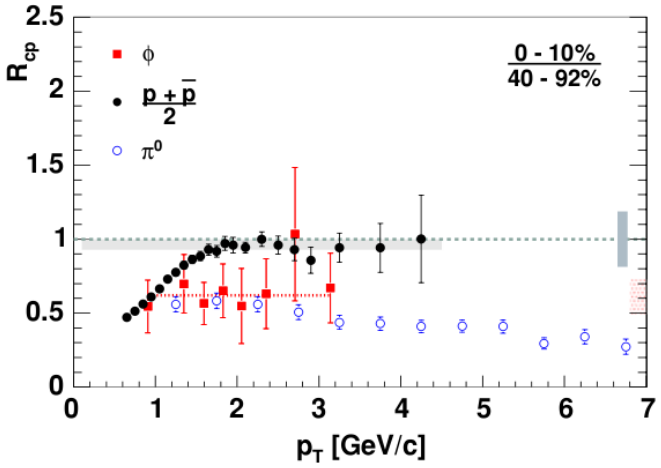

Figure 1.10: N_{coll}-scaled central to peripheral ratio, R_{CP}, for $(p+\bar{p})/2$, π^0, and ϕ [77].

1.5 Thesis outline

This thesis comprises two parts. The first part attempts a systematic study of the ϕ meson production in the K^+K^- decay channel in p+p, d+Au and Au+Au collisions at $\sqrt{s_{NN}}$=200 GeV using the PHENIX detector at RHIC. As discussed in Section 1.4 ϕ is a valuable probe of the medium created in high energy heavy-ion collisions. The results presented in this thesis include the transverse momentum spectra, the ϕ meson rapidity density and the nuclear modification factors R_{dA}, R_{AA} and R_{CP} studied as a function of centrality. The R_{AA} of the ϕ is compared with the R_{AA} of other particles and with the the R_{AA} of the ϕ obtained in Cu+Cu collisions [78]. The ϕ meson yields obtained in the K^+K^- channel are compared with those obtained in the e^+e^- decay channel [79].

The precision of the $\phi \rightarrow e^+e^-$ [79] and low-mass dilepton continuum measurements [80] performed by PHENIX is limited by a huge combinatorial background originating from unrecognized γ-conversions and π^0 Dalitz decays. In order to overcome this problem a Hadron Blind Detector (HBD) was developed and built. A report on the HBD upgrade project for the PHENIX experiment at RHIC is presented in the second part of this thesis.

The outline for the thesis is as follows. Chapter 2 gives a brief description of the RHIC accelerator facility and the PHENIX detector. Chapter 3 contains details of the analysis methods and techniques. In Chapter 4 we present and discuss the results of the analysis. Finally, Chapter 5 provides a description of the HBD concept and the results of the comprehensive R&D program to demonstrate its validity. It also includes a description of the mechanical design and construction procedures of the detector installed in PHENIX as well as first performance results of the HBD.

Chapter 2

Experimental apparatus

2.1 The Relativistic Heavy Ion Collider

The Relativistic Heavy Ion Collider (RHIC) [81], located at Brookhaven National Laboratory, is currently the world's highest energy collider of heavy nuclei. It is able to realize A+A collisions for a wide variety of nuclei up to 100 GeV per nucleon, p+p collisions with spin-polarized proton beams up to 250 GeV, and also asymmetric collisions like d+Au or p+Au.

A schematic layout of the RHIC accelerator complex is shown in Fig. 2.1. The RHIC complex consists of Tandem Van de Graaff, Linear Accelerator (LINAC), Heavy Ion Transfer Line (HILT), AGS-to-RHIC Transfer Line (ATR), Booster synchrotron, Alternating Gradient Synchrotron (AGS) and RHIC main rings. RHIC is an intersection storage ring particle accelerator. It has two independent hexagonally shaped rings with a circumference of $\sim$3.8 km, one for a clockwise and the other for counter-clockwise travelling beam. The rings are designed to cross at the middle of the six relatively straight sections allowing the particles to collide. Of the six interaction points, four have been occupied by experiments, designed to study heavy ion collisions: STAR [82], PHOBOS [83], BRAHMS [84] and PHENIX [85]. STAR and PHENIX are still active, while PHOBOS and BRAHMS have completed their operation after 2005 and 2006, respectively.

Since the pilot run in 1999 and up to the middle of 2009 RHIC had four operating periods (runs) with Au+Au collisions, two d+Au runs, a Cu+Cu run and six polarized protons runs. The collision species, energy, and integrated luminosity of the various runs are listed in Table 2.1. The analysis presented in this thesis is based on the the p+p data from Run-5, the d+Au data from Run-3, and the Au+Au data from Run-4, all taken at $\sqrt{s_{NN}} = 200$ GeV.

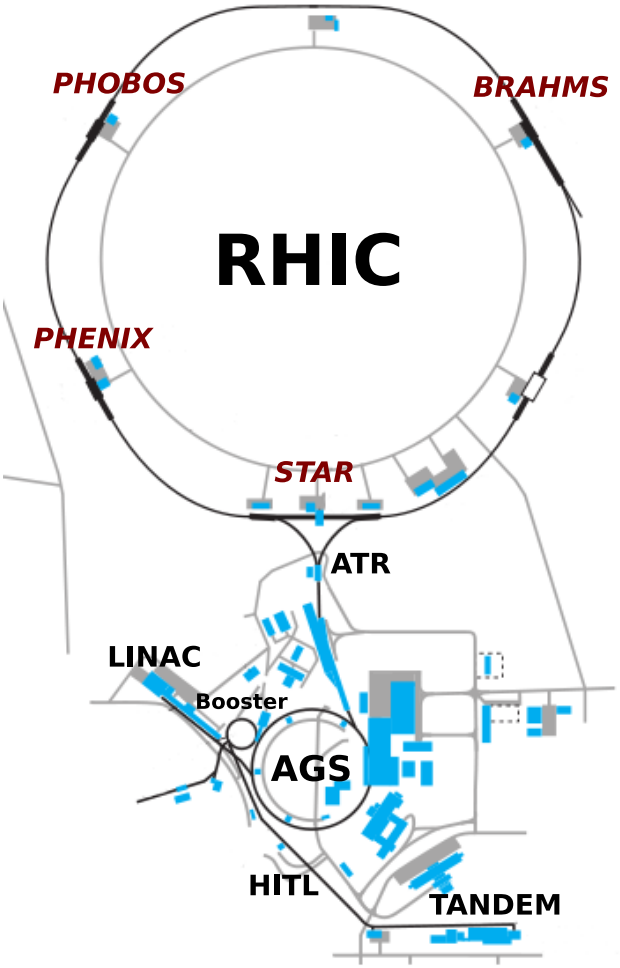

Figure 2.1: The RHIC complex schematic layout.

2.2 The PHENIX detector

The layout of the PHENIX detector as used in Run-7 is shown in Fig. 2.2. The PHENIX detector comprises four spectrometer arms. The two central arms (East and West) are instrumented to detect electrons, photons and charged hadrons. They cover $|\eta| < 0.35$ in pseudo-rapidity and 90° in azimuthal angle. The two forward (muon) arms (North and South) are instrumented to detect muons. They have full azimuthal coverage for $1.2 < |\eta| < 2.4$. There are three magnets in PHENIX: the Central Magnet provides an axial magnetic field for the central arms while the Muon Magnets produce a radial field for the muon arms. A set of inner coils in the central magnet, installed for Run-4, allows to perform measurements with different magnetic field configurations in the central arms. Prior to the installation of the inner coils in the first tree runs (Run-1, Run-2 and Run-3), all data were taken with only the outer coils of the Central Magnet powered ("0+"

RUN	Year	Species	$\sqrt{s_{NN}}$ (GeV)	$\int Ldt$
Run-1	2000	Au+Au	130	1 μb^{-1}
Run-2	2001/2002	Au+Au	200	24 μb^{-1}
		Au+Au	19	
		p+p	200	0.15 pb^{-1}
Run-3	2002/2003	d+Au	200	2.74 nb^{-1}
		p+p	200	0.35 pb^{-1}
Run-4	2003/2004	Au+Au	200	241 μb^{-1}
		Au+Au	62.4	9 μb^{-1}
Run-5	2004/2005	Cu+Cu	200	3.06 nb^{-1}
		Cu+Cu	62.4	0.19 nb^{-1}
		Cu+Cu	22.4	2.7 μb^{-1}
		p+p	200	3.78 pb^{-1}
Run-6	2005/2006	p+p	200	10.7 pb^{-1}
		p+p	62.4	0.1 pb^{-1}
Run-7	2006/2007	Au+Au	200	725 μb^{-1}
Run-8	2007/2008	d+Au	200	81 nb^{-1}
		p+p	200	5.7 pb^{-1}
		Au+Au	9.2	
Run-9	2008/2009	p+p	500	$\sim$14 pb^{-1}
		p+p	200	$\sim$16 pb^{-1}

Table 2.1: RHIC running periods and integrated luminosity delivered to the PHENIX experiment.

mode). The effective magnetic field integral in this configuration is equal to $\int Bdl =$ 0.78 T·m. Taking data in the mode where both the outer and inner coils are energized to have adding fields ("++" or "−−" mode) gives a better momentum resolution due to the larger effective magnetic field integral of $\int Bdl = 1.15$ T·m. In the mode with opposite coil polarity ("+−" or "−+" mode), which provides an effective magnetic field integral of $\int Bdl = 0.43$ T·m, the magnetic field in the vertex region is cancelled up to a radial distance of $\sim$60 cm, which is essential for the operation of the HBD detector (see Chapter 5). The left panel of Fig. 2.3 shows the magnetic field lines for the "++" Central Magnet coils operation mode and the right panel shows the same for the "+−" mode.

The central arms contain a tracking system consisting of Drift Chambers (DC) and Pad Chambers (PC) [86]. There are two types of Electro-Magnetic Calorimeters (EMCal), one made of lead-glass (PbGl) and the other made of lead and scintillator material (PbSc), for measuring the energy of electrons and photons. There is also a Ring-Imaging Čerenkov Counter (RICH) for electron identification and a set of Time-Of-Flight detectors (TOF) and Aerogel Čerenkov Counters (ACC) for charged hadron identification. These subsys-

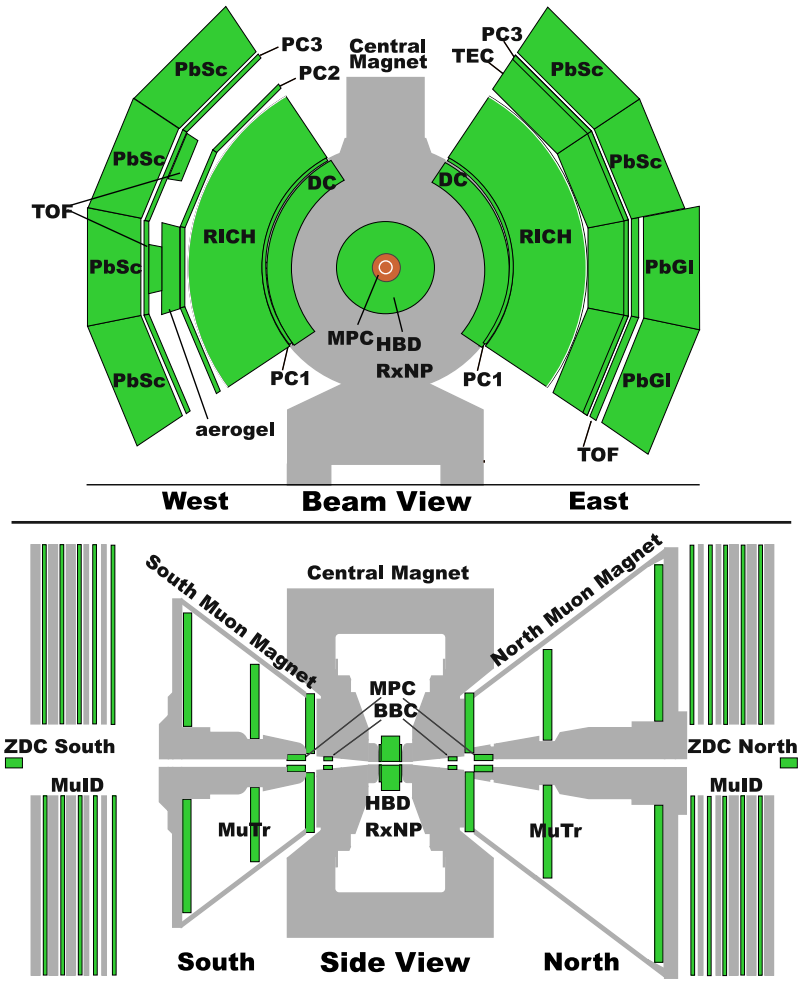

Figure 2.2: Configuration of the PHENIX detector in Run-7.

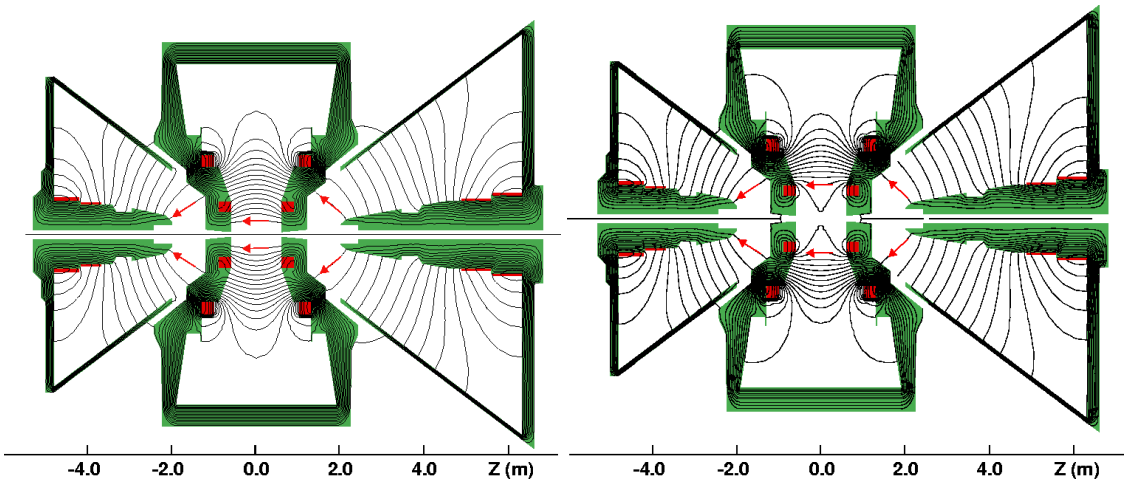

Figure 2.3: Magnetic field lines in the PHENIX detector, for the two central magnet coils in "++" (left) and "+−" (right) modes.

tems, together with the initial time information measured in the Beam-Beam Counters (BBC) are capable to identify hadrons, electrons and photons over a large momentum range. The HBD for the measurement of low mass dileptons was commissioned in Run-7 and used for physics in Run-9. The Zero Degree Calorimeters (ZDC) and the BBC are dedicated subsystems that determine the collision vertex and event centrality and also provide the minimum bias interaction trigger.

The analysis described in this report utilizes mainly the BBC, ZDC, DC, PC, EMCal and TOF subsystems of the PHENIX detector.

2.3 Global event characterization

2.3.1 Global detectors

Two systems are used to determine the global event information such as the time and location along the beam axis of the collision, and the collision centrality: two identical arrays of Čerenkov counters (BBC) [87, 88] and a pair of zero-degree calorimeters (ZDC) [89]. The BBC and ZDC located around the beam direction at ± 1.44 m and ± 18.25 m respectively, are shown in the bottom panel of Fig. 2.2. Each BBC is made of 64 meshed dynode photomultiplier tubes (Hamamatsu R6178) equipped with quartz Čerenkov radiators. The ZDC are small transverse area hadron calorimeters that measure the total energy of the spectator neutrons emitted from nuclear fragments after a collision[1]. The ZDC detectors consist each of alternating layers of tungsten and quartz Čerenkov fibers arranged in ribbons and placed at zero degrees.

2.3.2 Collision centrality determination

The event centrality reflects the degree of overlap between the two colliding nuclei and their impact parameter. Both, the total BBC charge and the total energy of spectator neutrons measured by the ZDC are sensitive to the impact parameter of the collision. A schematic figure of a nuclear collision is shown in Fig. 2.4. The centrality is determined from the charge measured by the BBC correlated with the energy of spectator neutrons deposited in the ZDC, as shown in Fig. 2.5. One can define a certain number of centrality bins using two-dimensional angular cuts. The contour lines for these cuts are decided by the origin at $[Q_0,0]$ and requiring the same number of events in each centrality bin. There is a certain freedom in choosing the origin Q_0, however this has only little effect on the

[1] Charged particles are bended away from the ZDC by the beam dipole magnets

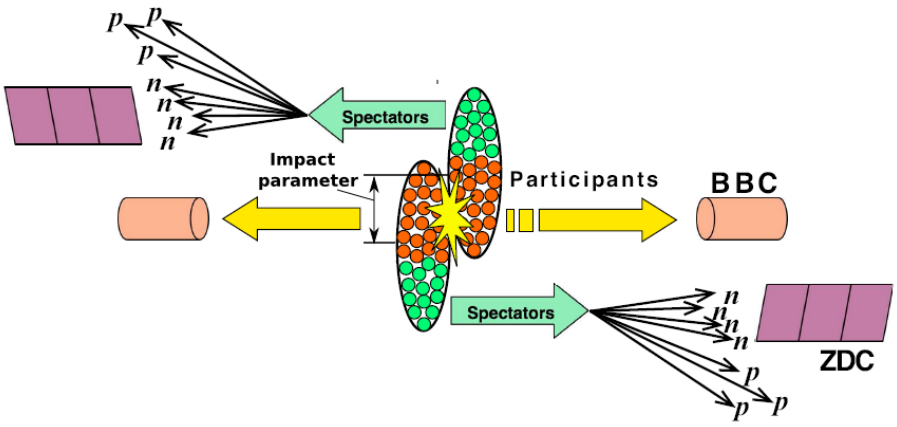

Figure 2.4: Centrality measurement.

centrality definition and will be discussed later. For the case shown in Fig. 2.5, Q_0 is equal to 0.3 in the arbitrary units of the figure.

In high energy nuclear physics the number of nucleon-nucleon collisions (N_{coll}) and the number of participant nucleons (N_{part}) are commonly used to characterize the centrality of the collision. The relation between the impact parameter, N_{coll} and N_{part} can be calculated with a Monte Carlo simulation based on the Glauber model formalism [90]. The Glauber model approximates the heavy ion collision as a superposition of individual nucleon-nucleon interactions assuming that the nucleons travel in straight line trajectories. The distribution of the nucleons in coordinate space is usually determined in this model by a Woods-Saxon distribution:

$$\rho(r) = \frac{1}{1+e^{\frac{r-r_n}{d}}}, \tag{2.1}$$

where r_n is the nuclear radius and d is the diffuseness parameter. For the gold nucleus r_n and d are taken to be 6.38 fm and 0.54 fm, respectively [91]. The responses of the BBC and ZDC detectors in Au+Au collisions were studied using Glauber Monte-Carlo simulations for different values of the impact parameter. The centrality classes are then determined using the same method as for real data. The Glauber simulation results on N_{coll} and N_{part} for the centrality bins used in the analysis discussed in this thesis are shown in Table 2.2. The results for N_{part} and N_{coll} vary by less than 1% in central and semi-central collisions and by approximately 10% in very peripheral collisions depending on the choice of the Q_0 value. The larger errors in N_{part} and N_{coll} quoted in Table 2.2 come from model uncertainties. More details about the relation between centrality, N_{part} and N_{coll} can be found in [92].

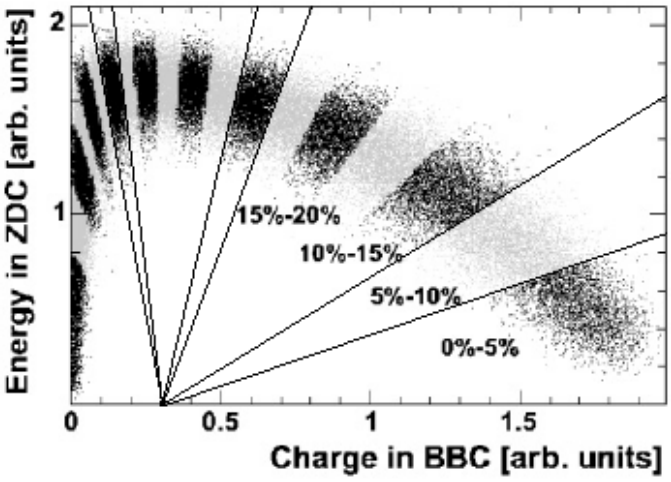

Figure 2.5: Different centrality classes based on the ZDC vs. BBC distribution.

Centrality, %	N_{part}	N_{coll}
MB	109.1 ± 4.1	257.8 ± 25.4
0−10	325.2 ± 3.3	955.4 ± 93.6
10−20	234.6 ± 4.7	602.6 ± 59.3
20−30	166.6 ± 5.4	373.8 ± 39.6
30−40	114.2 ± 4.4	219.8 ± 22.6
40−50	74.4 ± 3.8	120.3 ± 13.7
50−60	45.5 ± 3.3	61.0 ± 9.9
60−93	14.5 ± 2.5	14.5 ± 4.0

Table 2.2: The centrality classes and the corresponding average numbers of nucleon-nucleon collisions and participants for Au+Au collisions at $\sqrt{s_{NN}} = 200$ GeV.

2.3.3 Vertex position determination

The collision time with respect to the RHIC clock is measured independently by BBC^{North} and BBC^{South}, via the average timing of the hits in these detectors. The half-sum of the resulting t_{BBC}^{North} and t_{BBC}^{South} is used as the reference time t^0 for the time-of-light measurements, while their difference is used for the determination of the z-coordinate of the collision vertex z_{vtx} by:

$$z_{vtx} = \frac{c}{2}(t_{BBC}^{North} - t_{BBC}^{South}) \tag{2.2}$$

where c is the speed of light. The BBC time resolution of 52±4 ps allows to achieve a vertex resolution in the z-direction of 1.2 cm in p+p and 0.3 cm in central Au+Au collisions.

2.4 Charged particles tracking

2.4.1 Central arm tracking detectors

The particle trajectory is reconstructed using the DC and PC1 subsystems. The multi-wire low mass PHENIX DC [93] consists of two cylindrically shaped chambers, identical in design, each covering 90° in azimuth and $|\eta| < 0.35$. The DC extends between 2.02 m and 2.46 m in the radial direction and have a length of 1.8 m in the z-direction. Each arm of the DC consists of a cylindrical titanium frame supporting wire nets, confined by mylar windows. The gas volume is filled with a 50%/50% mixture of argon and ethane. Each frame is divided in 20 identical sectors, called keystones, each covering 4.5° in azimuth. There are six layers of wire modules in each keystone running in the z-direction: X1, U1, V1, X2, U2, and V2, each of which contains 4 anode and 4 cathode planes. The X1 and X2 wires run in parallel to the beam to perform precise track measurements in r-ϕ plane. The U1, V1, U2 and V2 wires have stereo angles of about 6° relative to the X wires providing a measurement of the z-coordinate of the track. Fig. 2.6 shows a schematic view of one arm of the DC, the wire structure of one DC keystone and the relative arrangement of the U, V and X wire layers.

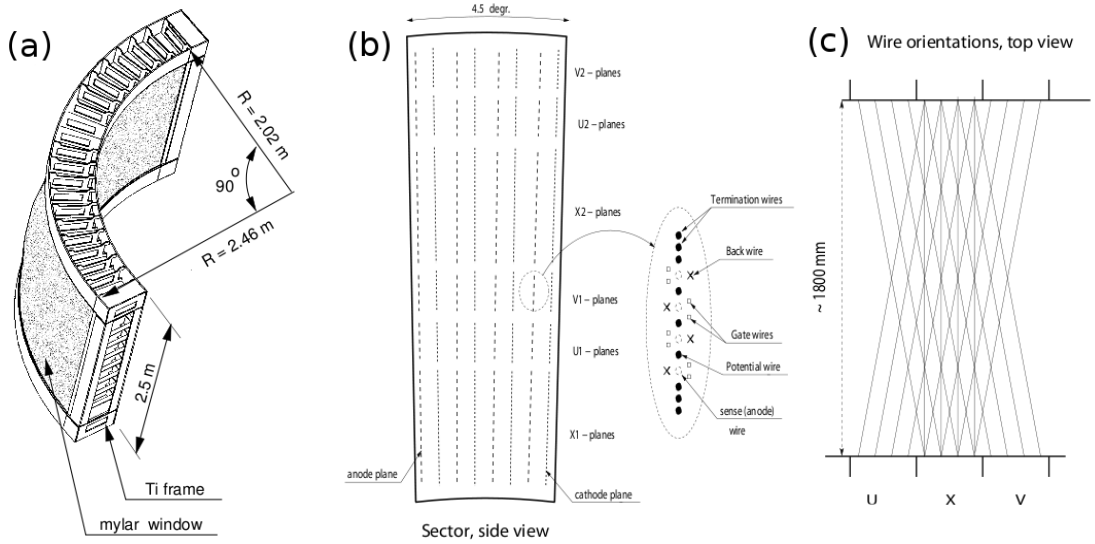

Figure 2.6: (a) Schematic view of one arm of the PHENIX DC subsystem. (b) Wire structure of a DC keystone. (c) The relative arrangement of the U, V and X wire layers.

The PHENIX PC [94] are multi-wire proportional chambers with a cathode pad read-out. They provide a three dimensional coordinate measurement of the track position. There are three layers of Pad Chambers in the West arm (PC1, PC2 and PC3) and two layers in the East arm (PC1 and PC3). PC1, PC2 and PC3 layers are located at radii

of 249 cm, 419 cm and 499 cm from the interaction point, respectively. Each PC layer consist of eight sectors. Each PC1 sector covers 11.25° in azimuth and $|\eta| < 0.35$ in pseudo-rapidity. PC2 and PC3 sectors have a square shape for better mechanical rigidity and cover each 22.5° in azimuth and 1/2 of the central arm acceptance in pseudo-rapidity ($-0.35 < \eta < 0$ or $0 < \eta < 0.35$). A schematic 3D view of the PC subsystem is shown in Fig. 2.7. Each chamber contains a single plane of wires inside a gas volume confined between two cathode planes. One of the cathode planes is substructured into a fine array of pixels, and the other one is solid copper. The operating gas for the PC is a 50%/50% mixture of argon and ethane (same as for the DC). The basic readout element is a pad formed by nine non-neighboring pixels shown in the left panel of Fig. 2.8. Three pixels from three neighboring pads form a "cell" as shown by the red contour in the right panel of Fig. 2.8, which uniquely identifies the location of the track. The interleaved pad plane design provides a fine position resolution of about 1.7 mm in the z-direction while reducing the total number of readout channels . The PC1 is essential for the track reconstruction and determination of the three dimensional momentum of a particle. The PC2 and PC3 help to reject background in the outer detectors.

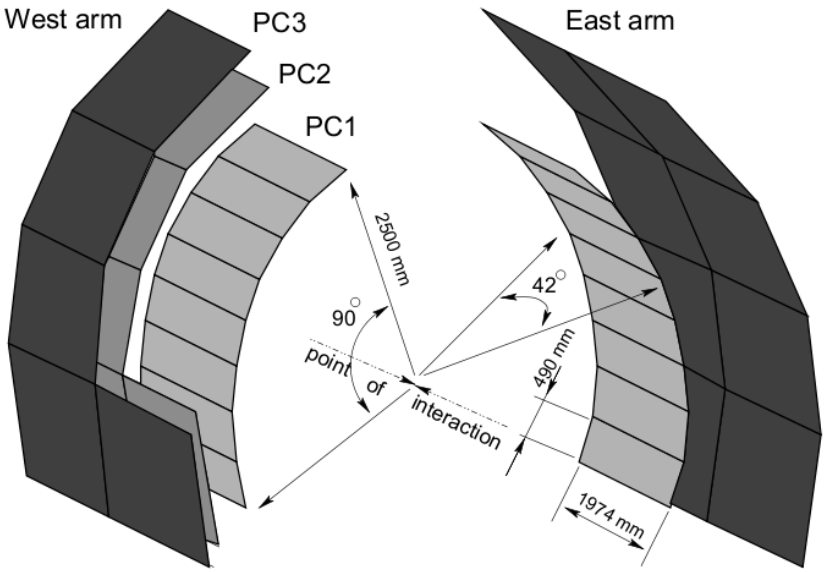

Figure 2.7: Schematic view of the PHENIX PC subsystem. Several sectors of PC3 and PC2 in the West arm are removed for clarity.

2.4.2 Track reconstruction

Fig. 2.9 shows the track trajectory of a charged particle travelling in the axial magnetic field of the central arms in the $x-y$ (left panel) and $z-r$ (right panel) planes and provides

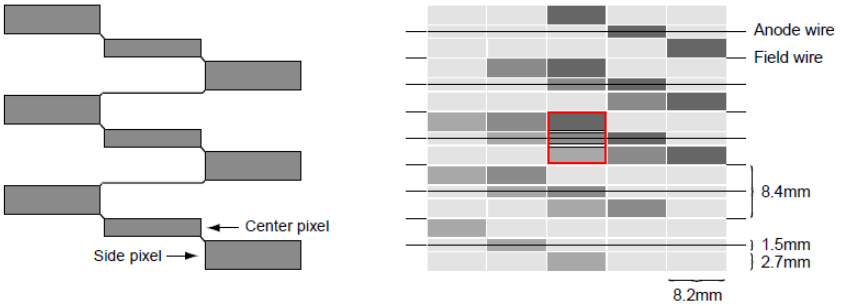

Figure 2.8: The pad and pixel geometry (left). A "cell" defined by three pixels from tree neighboring pads is shown by the red contour in the center (right).

a schematic illustration of the variables relevant for track characterization:

- z_{vtx} - interaction vertex position along the z axis.
- α - inclination of the track w.r.t. an infinite momentum track at the DC reference radius of 220 cm in the $x-y$ plane.
- δ - inclination of the track w.r.t. an infinite momentum track at the DC reference radius of 220 cm in the $z-r$ plane.
- β - track's polar angle at the reference radius of 220 cm.
- θ_0 - track's polar angle at the vertex.
- ϕ_0 - track's azimuthal angle at the vertex.
- ϕ - azimuthal angle of the infinite momentum track.
- θ - polar angle of the infinite momentum track.
- *zed* - z coordinate at which the track crosses the DC reference radius of 220 cm.

First, all hits from the X1 and X2 wires of the DC projected to the $x-y$ plane are used to define the ϕ and α angles for all track candidates. This is done using a combinatorial Hough transform technique under the assumption that tracks are straight in the DC and come from the vertex. The next step is background tracks removal. A real track is required to have at least 8 X1, X2 wires hits associated to it, otherwise it is discarded. A track association is done by an iterative fitting approach, weighting hits according to their deviation from the straight line guess of the trajectory. The farther from the straight line guess the hit is - the smaller the weight it gets and therefore the fit is not disturbed by hits from noise or other tracks. Each hit is allowed to correspond only to a single track and normally the closest track candidate is chosen. Then, information about z_{vtx} measured by BBC, reconstructed clusters in the PC1 and hits in the UV wires of the DC is utilized to reconstruct the track in the $z-r$ plane. If there is an unambiguously associated cluster in the PC1 within 2 cm from the projection of the track candidate to the PC1 plane, the *zed*

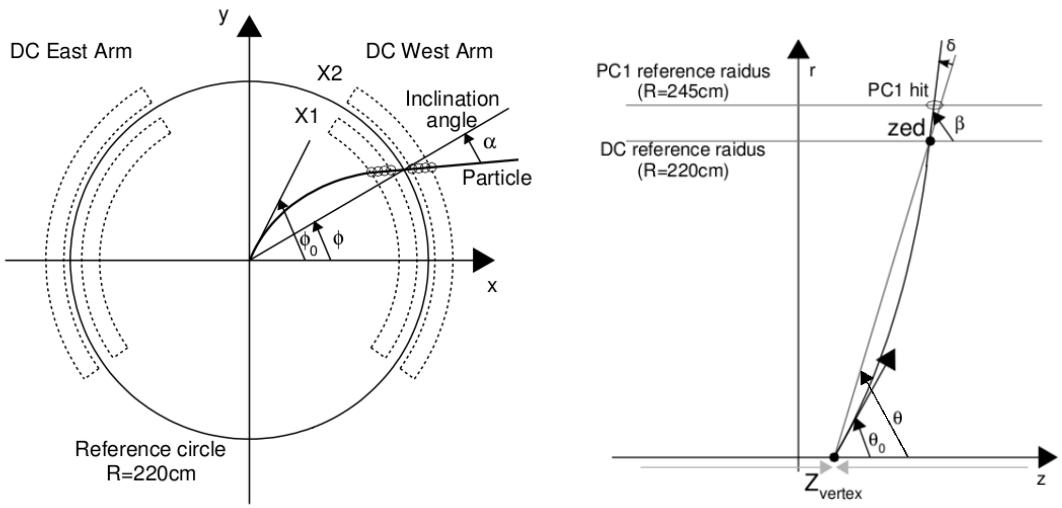

Figure 2.9: Illustration of the variables used for track definition.

of the track is defined by the z-coordinate of this cluster and z_{vtx}. If no cluster is found, or if there is ambiguity in the cluster association, then the hits from the UV wires of the DC are used to determine *zed*. More details about the track reconstruction technique in the PHENIX central arm can be found in [95].

The quality of the reconstructed track is given by a 6-bit variable evaluated using:

$$Q_{track} = A \times 2^0 + B \times 2^1 + C \times 2^2 + D \times 2^3 + E \times 2^4 + F \times 2^5 \tag{2.3}$$

where A, B, C, D, E and F are quality bits defined as follows:

- A = 1 if X1 plane is used.
- B = 1 if X2 plane is used.
- C = 1 if there are hits in UV plane.
- D = 1 if there are hits in UV plane and their choice is unique.
- E = 1 if there are clusters in PC1.
- F = 1 if there are clusters in PC1 and their choice is unique

otherwise the bits are set to 0. Note that the A and B bits cannot be zero at the same time, because of the requirement of at least 8 hits in the X1, X2 planes for real tracks mentioned above. The best quality is a Q_{track} value equal to 63, the second best case is Q_{track} =31. The track quality values are summarized in Table 2.3. Fig. 2.10 shows track quality distributions as seen in Run-3 d+Au, Run-4 Au+Au and Run-5 p+p collisions. In the analyses described in this thesis only tracks with quality equal to 31 and 63 are used (sometimes tracks with quality 51 are also used).

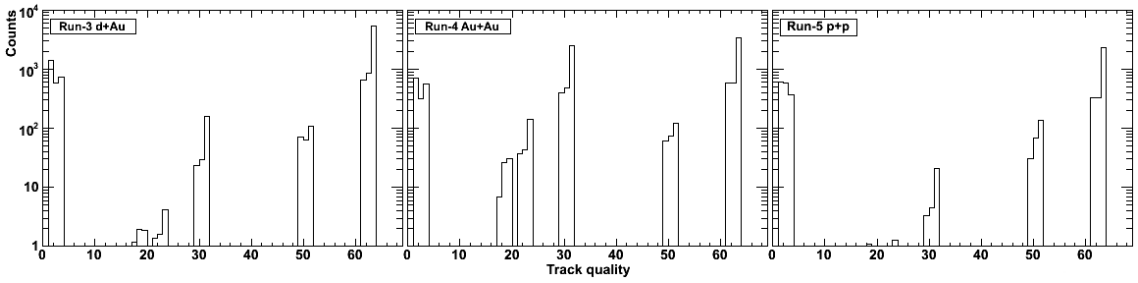

Figure 2.10: Track quality distributions as seen in Run-3 d+Au, Run-4 Au+Au and Run-5 p+p collisions. The distributions have been normalized to have same the integral.

Comment	A	B	C	D	E	F	Q_{track}
$\mathrm{PC1}^{found}_{unique}$ & $\mathrm{UV}^{found}_{unique}$	1	0	1	1	1	1	61
	0	1	1	1	1	1	62
	1	1	1	1	1	1	63
$\mathrm{PC1}^{found}_{unique}$ & no UV	1	0	0	0	1	1	49
	0	1	0	0	1	1	50
	1	1	0	0	1	1	51
$\mathrm{PC1}^{found}_{ambiguous}$ & $\mathrm{UV}^{found}_{unique}$	1	0	1	1	1	0	29
	0	1	1	1	1	0	30
	1	1	1	1	1	0	31
$\mathrm{PC1}^{found}_{ambiguous}$ & UV^{found}	1	0	1	0	1	0	21
	0	1	1	0	1	0	22
	1	1	1	0	1	0	23
$\mathrm{PC1}^{found}_{ambiguous}$ & no UV	1	0	0	0	1	0	17
	0	1	0	0	1	0	18
	1	1	0	0	1	0	19

Table 2.3: Summary of the DC track quality.

2.4.3 Momentum determination

An exact analytical solution for the momentum of the charged particles traversing the magnetic field region of the central arms cannot be determined due to the complexity and non-uniformity of the field. Instead, look-up tables derived from simulation are adopted to determine the particle momentum. A four-dimensional field-integral $f(p, r, \theta_0, z_{vtx})$ is calculated by passing particles through the measured magnetic field map shown in Fig. 2.11. For each grid point defined by the total particle momentum p, the radius r, the polar angle θ_0 and the z coordinate of the event vertex z_{vtx} the value of the field-integral is obtained by numerical integration.

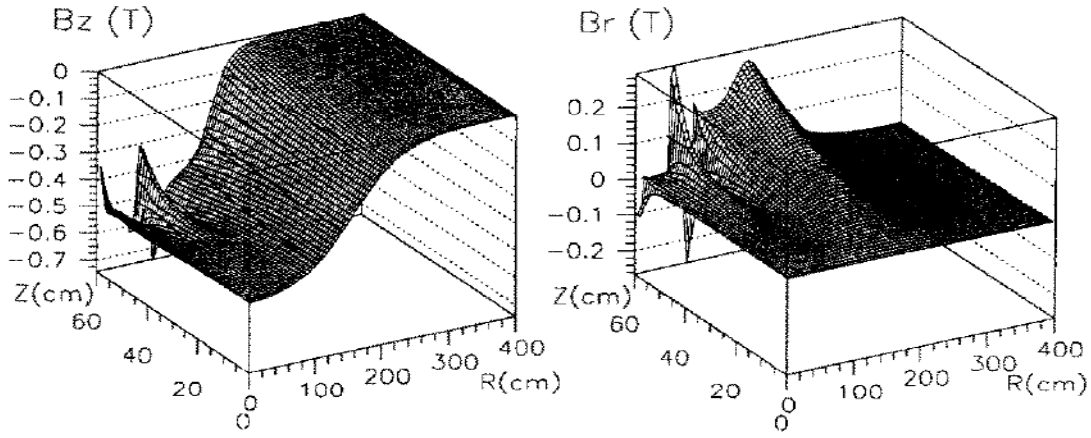

Figure 2.11: The central arm magnetic field map. The z (left) and radial (right) components of the magnetic field are plotted as function of z and R.

The field-integral $f(p,r,\theta_0,z_{vtx})$ at a given radius r varies linearly with the ϕ angle:

$$\phi = \phi_0 + \frac{q}{p} f(p,r,\theta_0,z_{vtx}) \tag{2.4}$$

Under the assumption that all tracks originate from the event vertex, an iterative procedure is used to find the true momentum:

1. Make an initial estimate of the momentum from the angles α and θ as measured by DC/PC1.
2. Perform a four-dimensional polynomial interpolation of the field-integral to extract $f(p,r,\theta_0,z_{vtx})$ value for each hit associated to the track.
3. Perform a fit in ϕ *vs.* f to determine q/p and ϕ_0.
4. Repeat the procedure starting form step 2 plugging the extracted q/p and ϕ_0 values into Eq. 2.4.

Typically, less than four iterations are necessary for convergence on the p and ϕ_0 values. A similar procedure is used in the $z-r$ plane to find the value of the θ_0 angle.

The momentum resolution is given by:

$$\delta p/p = \sigma_{ms} \oplus \sigma_{DC} \cdot p(GeV/c) \ , \tag{2.5}$$

where σ_{ms} is the contribution due to multiple scattering and σ_{DC} is the intrinsic momentum resolution of the DC. The measured value of σ_{DC} scales with the magnetic field strength and was found to be $\sim 1.1\%$ and 0.76% in Run-3 ("0+" field configuration) and Run-4 ("++" or "−−" field configuration), respectively. The multiple scattering term σ_{ms} is equal to 0.7%.

2.4.4 Track association

For particles that were not created in the collision (decay products, shower particles, γ-conversions), there are instances where the point of origin is displaced with respect to the collision vertex by several centimeters. In these cases the track is assigned a wrongly reconstructed momentum, since the momentum determination algorithm assumes that all tracks originate from the collision vertex, as mentioned in Section 2.4.3. Tracks with wrong momentum are considered as background tracks and need to be taken out from the pool of tracks. The matching cuts in ϕ and z to the outer detectors are used to remove the background tracks. It is convenient to express the matching cuts in p_T-independent and particle charge independent reduced variables. In order to do that we construct matching distributions $\Delta\phi = \phi_{hit} - \phi_{proj}$ and $\Delta z = z_{hit} - z_{proj}$ distributions as a function of the track's transverse momentum separately for positive and negative tracks. Here, ϕ_{proj} and z_{proj} are the coordinates of the track projection onto the detector plane, and ϕ_{hit} and z_{hit} are the coordinates of the hit closest to the track projection. The matching distributions are fitted with a Gaussian function plus a second order polynomial function for background and the reduced matching variables are defined as:

$$n_\phi = (\Delta\phi - \phi_0)/\sigma_\phi \qquad\qquad n_z = (\Delta z - z_0)/\sigma_z, \tag{2.6}$$

where ϕ_0, z_0 are the mean values, and σ_ϕ, σ_z are the sigma values of the Gaussian fits to the $\Delta\phi$ and Δz distributions respectively. Fig. 2.12 shows typical matching distributions for the PC3, EMCal and TOF subsystems and fits used to calculate the reduced variables. The matching cuts used in this work can be found in Table 3.2.

2.5 Charged particle identification

The TOF serves as the most precise particle identification (PID) device for charged hadrons in PHENIX [96]. The TOF counter consists of 10 TOF walls, forming a "T"-profile with 8 panels on the upper part of the "T" and 2 panels on the lower part as shown in Fig. 2.13. One TOF wall consists of 96 segments, each equipped with a plastic scintillator slat oriented along the $r-\phi$ direction with phototubes at both ends. The plastic scintillator used is Bicron BC404, 1.5 cm in width and 1.5 cm in depth.The PMTs are Hamamatsu R3478S with a diameter of 3/4 inch. The TOF counter is located in the East arm, ∼5.0 m away from the vertex (see Fig. 2.2). Both, the upper and bottom parts of the TOF cover 22.5° in azimuth, while in pseudorapidity the upper part extends over $|\eta|$ <0.35, and the bottom part has a factor of 4 smaller coverage of $|\eta|$ <0.00875. With a time resolution $\sigma_t \simeq 130$ ps it allows to achieve reliable pion-kaon and kaon-proton separations up to

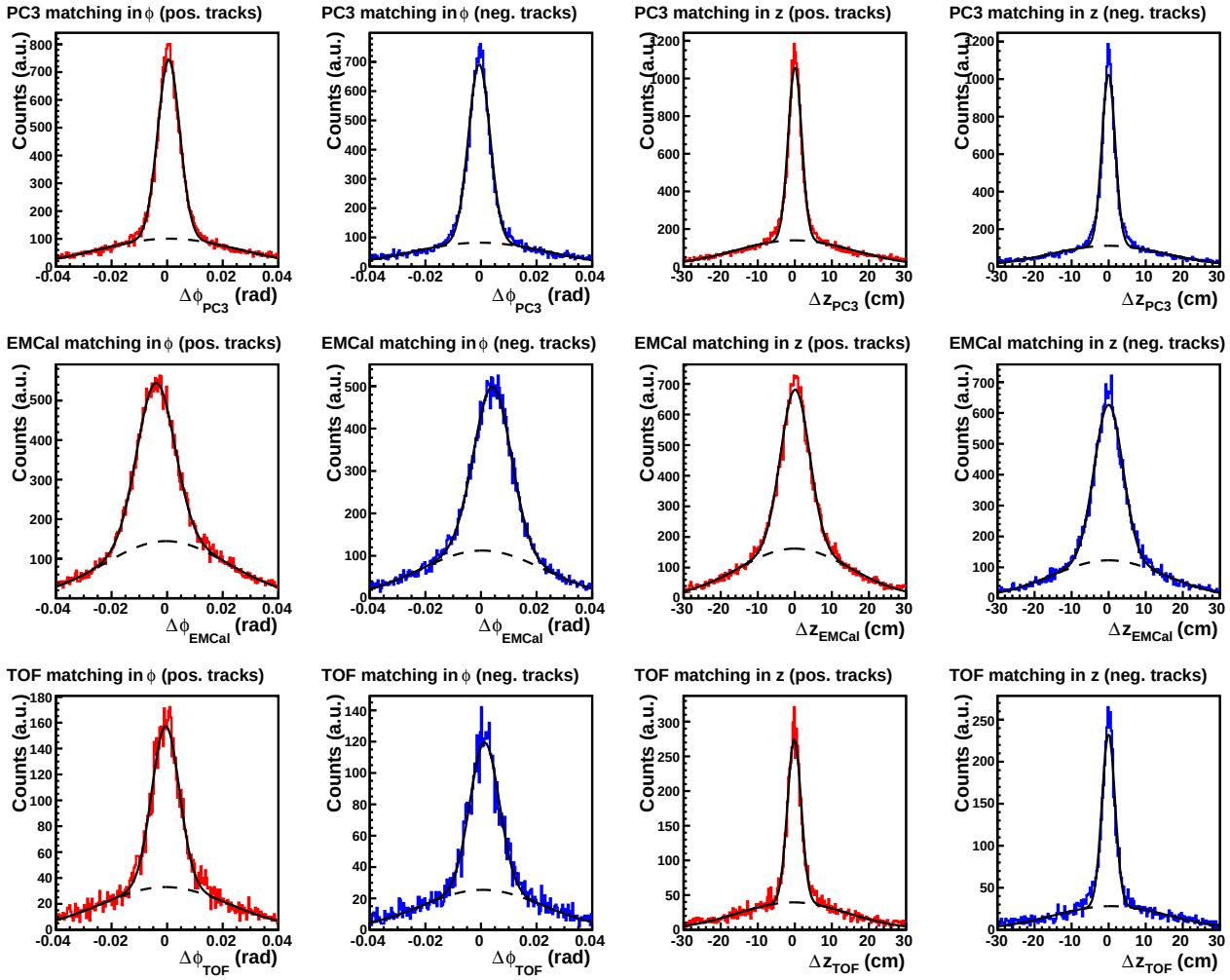

Figure 2.12: Track matching to PC3 (top), EMCal (middle) and TOF (bottom) along the ϕ and z coordinates for positive (red) and negative (blue) tracks. All distributions are for the momentum bin $0.5-0.6$ GeV/c. The EMCal and PC3 distributions are for sector 0. Solid lines represent the fits used to calculate reduced variables (see text), dashed lines indicate the residual background estimated from these fits.

$p_T = 2.5$ GeV/c and $p_T = 4$ GeV/c, respectively. The particle separation capabilities of the TOF subsystem are illustrated in Fig. 2.14.

The knowledge of the time-of-flight t_{TOF}, measured by the TOF and BBC, along with the momentum p, determined by the DC, and the flight path-length from the collision vertex to the track projection onto the TOF plane L, calculated from the reconstructed particle trajectory, allows to estimate the square of the particle mass using the following relation:

$$m^2 = \frac{p^2}{c^2}\left[\left(\frac{t_{TOF}}{L/c}\right)^2 - 1\right] \tag{2.7}$$

The charged particle identification is performed using cuts in m^2 and momentum

Figure 2.13: The TOF wall mounted in PHENIX.

space. One could notice in the bottom panel of Fig. 2.14 that the width of the m^2 distributions for pions, kaons and protons vary with momentum. The widths and the mean positions of the m^2 distributions for each particle species are obtained for each p_T bin by fitting the vicinity of each peak in the distributions with a Gaussian function as shown in Fig. 2.15. The momentum-dependence of the width can be understood as a sum of several contributions:

$$\sigma^2_{m^2}(p) = \frac{\sigma^2_\alpha}{K_1^2}(4m^4p^2) + \frac{\sigma^2_{ms}}{K_1^2}\left[4m^4\left(1+\frac{m^2}{p^2}\right)\right] + \frac{\sigma_t^2 c^2}{L^2}\left[4p^2(m^2+p^2)\right], \tag{2.8}$$

where σ_α is the angular resolution, σ_{ms} is the multiple scattering term, σ_t is the overall time-of-flight resolution, m^2 is the centroid of the m^2 distribution for each particle species, c is the speed of light, and K_1 is the magnetic field integral constant term of 101.0 mrad GeV. The parameters σ_α, σ_{ms} and σ_t are obtained by simultaneous fit of the width as a function of momentum with Eq. 2.8 for six particles: π^+, π^-, K^+, K^-, p and $\bar{p}$ and for the Run-5 p+p data they are σ_α = 1.116 mrad, σ_{ms} = 0.96 mrad·GeV, and $\sigma_t \simeq$ 130 ps. There are variables *IsPi*, *IsK*, and *IsP* commonly used in PHENIX that define the number of σ_{m^2} by which the present track's m^2 deviates from the presumption that the track itself is a pion, kaon or proton, respectively.

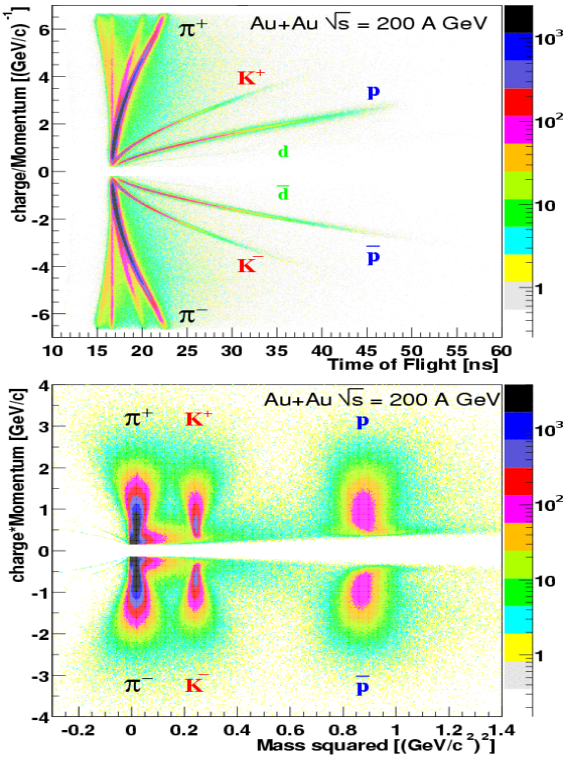

Figure 2.14: Particle identification by the TOF. Top: charge/momentum versus time-of-flight. Bottom: charge×momentum versus mass squared.

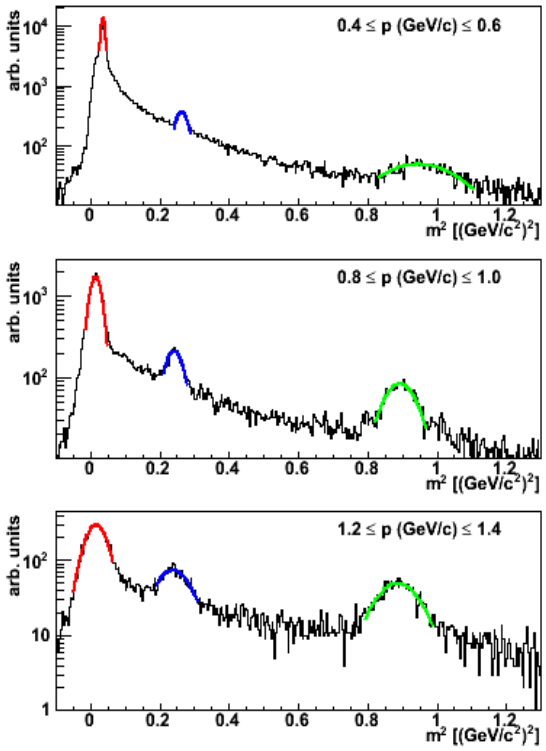

Figure 2.15: Mass-squared distribution for tracks passing through TOF for three momentum bins. Solid lines represent the fits with a Gaussian function used to determine the widths and the mean positions of the peaks corresponding to pions, kaons and protons.

2.6 Minimum Bias trigger

The total inelastic cross sections of p+p, d+Au and Au+Au collisions are equal to $\sigma_{inel}^{p+p} = 42 \pm 3$ mb, $\sigma_{inel}^{d+Au} = 2260 \pm 100$ mb and $\sigma_{inel}^{Au+Au} = 6850 \pm 540$ mb, respectively [64].

The minimum bias (MB) trigger used for p+p and d+Au collisions was a coincidence between the BBC^{North} and BBC^{South} with at least one hit in each arm and z_{vtx} within 30 cm of the nominal interaction point. In p+p collisions the MB trigger cross section was measured via the van der Meer scan technique [97] and found to be $\sigma_{BBC}^{p+p} = 23.0 \pm 9.7$ mb [98, 99]. The measured σ_{BBC}^{p+p} corresponds to 55.0±5% of the inelastic p+p cross section. In d+Au collisions the MB trigger cross section was measured to be $\sigma_{BBC}^{d+Au} = 1.99 \pm 5.2$ b [100] using the photodissociation of the deuteron as a reference [101]. The measured σ_{BBC}^{d+Au} corresponds to 88±4% of the inelastic d+Au collisions.

In Au+Au collisions the trigger condition was a coincidence between the BBC^{North}, BBC^{South}, ZDC^{North}, ZDC^{South} with at least two hits in each BBC arm, at least one neu-

tron detected in each ZDC arm, and z_{vtx} within 38 cm of the nominal interaction point. Simulation studies showed that this trigger is inefficient only for very peripheral collisions and records $92.2^{+2.5}_{-3.0}$% of the inelastic Au+Au cross section.

It is obvious that the probability at which the MB trigger fires, based on the conditions outlined above, depends on the event multiplicity. In particular this "trigger bias" is important for low multiplicity p+p and d+Au collisions. Processes like single- or double diffractive scattering produce far fewer hits in the BBC compared to a collision involving a hard parton scattering and therefore are more likely to fail in generating a trigger. Data taken with an unbiased clock trigger indicate that the BBC fires on 79% of p+p and 94% of d+Au of events[1] with tracks in the central arm acceptance. These fractions are taken as the trigger bias ε_{bias}. In central d+Au or in peripheral Au+Au collisions the event multiplicity is already high enough for the MB trigger not being biased.

To obtain the invariant yield of particles in p+p (dAu) collisions, the measured yield of particles must be corrected for the fraction of events missed by the MB trigger and for the trigger bias. The correction factor $\varepsilon_{BBC}/\varepsilon_{bias}$ is equal to 0.55/0.79 and 0.88/0.94 for minimum bias p+p and d+Au collisions, respectively.

2.7 PHENIX data acquisition system

The PHENIX data acquisition (DAQ) system [102, 103] processes the signals from each detector subsystem, produces the trigger decision, and stores the triggered data. The interaction rate at design luminosity of RHIC varies from a few kHz for Au+Au central collisions to approximately 500 kHz for minimum bias p+p collisions. One Au+Au event event is typically 200 kbytes and a p+p event is 60 kbytes in size. The PHENIX DAQ was designed to handle these high interaction rates and event sizes with the provision to accommodate future improvements in the luminosity. The schematic of the PHENIX DAQ system is shown in Fig. 2.16.

The DAQ utilizes several types of electronics modules: Master Timing Module (MTM), Granule Timing Module (GTM), Global Level-1 Trigger (GL1), Local Level-1 Trigger (LL1), Front End Module (FEM), Data Collection Modules (DCM). All of them are pipelined and synchronized with the RHIC beam clock[2], and overall the system has dead-time-less features.

The PHENIX subsystems are sampled on each beam crossing, every 106 ns (9.4 MHz). Data cannot be digitized at such a high rate, so the analog response from each subsystem

[1] In d+Au collisions, this fraction varies from 85% to 100% from peripheral to central collisions.

[2] The RHIC beam clock provide a central time signal synchronized with the ion (proton) bunches in the RHIC rings (Yellow Clock and Blue Clock) to each experiment.

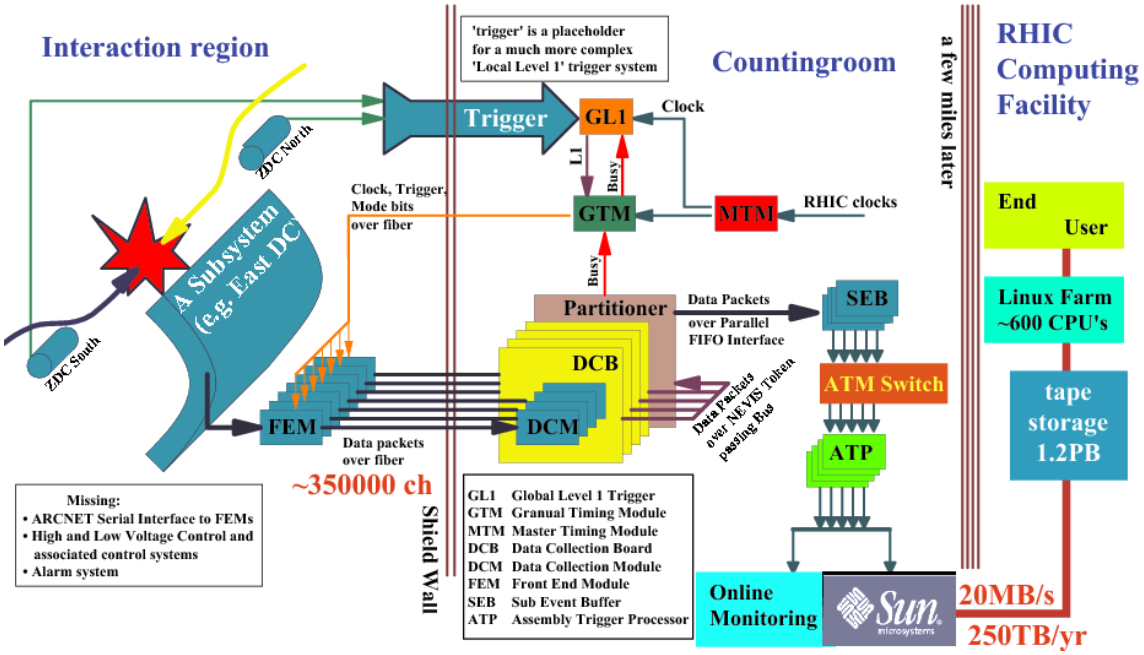

Figure 2.16: Block diagram of the PHENIX DAQ.

is transferred by cables to the FEMs, which are located near the detectors in the beam intersecting region. The transferred data are processed by Front End Electronics (FEE), that buffers the data of 40 beam bunch crossings to wait for the decision of GL1. The MTM receives the 9.4 MHz RHIC clock and delivers it to the GTM and GL1. The LL1 system communicates directly with a few fast detectors such as BBC, EMCal and RICH. Subsystem specific LL1 modules process the input data from the corresponding detector and produce a set of reduced-bit input for each RHIC beam crossing and sends it to the GL1. The GL1 then makes a trigger decision based on the assembled bits from the various LL1 subsystems, the DAQ busy signal and the trigger scale-down counter. Whenever a beam crossing satisfies the trigger criteria, the GTM delivers the clock, the control commands, and an event accept signal to the FEMs of each detector. After receiving the accept signal, each FEM starts to digitize the data. The triggered data fragments from the FEMs are transferred to the DCMs via optical fibers. The DCMs perform zero suppression, error checking and data reformatting. The formatted data are compressed and sent to the PHENIX Event Builder (EvB). The EvB consists of 39 Sub Event Buffers (SEBs), Asynchronous Transfer Mode (ATM) switch and 52 Assembly Trigger Processors (ATPs). The EvB receives many parallel data streams from the DCMs, assembles the data fragments from each stream into complete events and provides an environment for the higher level triggers to operate. Finally accepted events are transmitted to the PHENIX Online Con-

trol System (ONCS) for temporary storage in the “buffer boxes”. The data in the “buffer boxes” are used for online quality monitoring and calibration processes. Later on the data are transferred to the RHIC Computing Facility (RCF) for permanent storage on tapes.

Chapter 3

Data analysis

3.1 Overview

The studies of the ϕ meson production via the K^+K^- decay channel in Au+Au, d+Au and p+p collisions at $\sqrt{s_{NN}} = 200$ GeV , which are the main topic of this report, have been performed using data from three years of RHIC operations: Run-3, Run-4 and Run-5. The Run-5 high statistics p+p dataset provides the baseline for comparison with the d+Au and Au+Au measurements. The d+Au data collected in Run-3, and the high statistics Au+Au dataset of Run-4 serve to study cold and hot, nuclear matter effects, respectively. The integrated luminosities for these three datasets can be found in Table 2.1.

There were no major changes in the configuration of the PHENIX detector during the Run-3, Run-4 and Run-5 data taking periods other than the installation of the inner coils in the central magnet for Run-4 (also used in all subsequent runs). During Run-3 only the outer coils of the Central Magnet were energized ("0+" mode) giving an effective field integral of $\int Bdl = 0.78$ T·m. In Run-4 and Run-5 the inner coils were turned on ("++" or "−−" mode) increasing the magnetic field strength. The effective magnetic field integral in Run-4 and Run-5 was equal to $\int Bdl = 1.15$ T·m, resulting in better momentum resolution as compared to Run-3 (see Section 2.4.3).

Most of the analysis steps are very similar for all three datasets. Some changes result from improvements in the analysis procedures, others are due to the change in the magnetic field configuration between Run-3 and subsequent runs. The main differences between the analyses are in the methodology used to reconstruct the invariant mass spectra of ϕ mesons. Three different techniques were used. The first ("no PID") does not require identification of charged tracks in the final state and assumes that all tracks are kaons. The second ("one kaon PID") requires identification of only one kaon in the TOF subsystem . In the third technique ("two kaons PID") both kaons are identified in the TOF

subsystem. The examples of the invariant mass spectra obtained with the tree techniques for similar p_T bins are presented in Fig. 3.1.

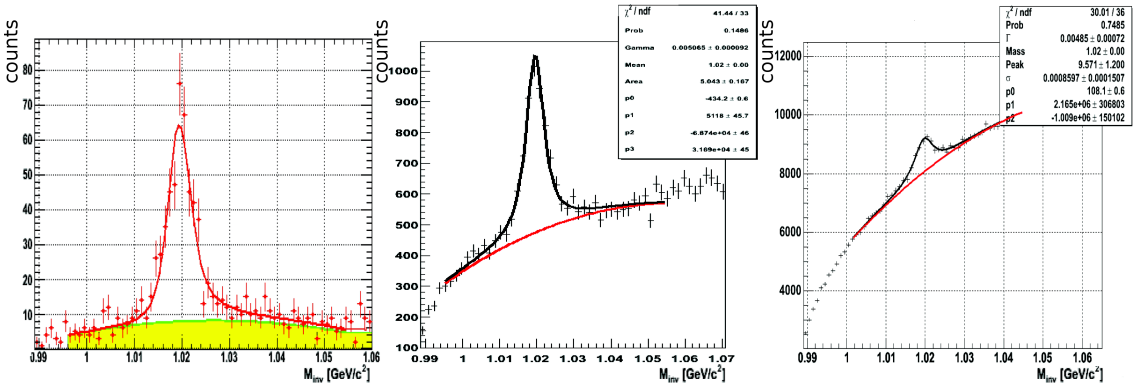

Figure 3.1: Invarainat mass spectra of K^+K^- pairs obtained in p+p collisions using the tree analysis techniques: "two kaons PID" (left), "one kaon PID" (center) and 'no PID" (right).

Each technique has its advantages and disadvantages. Both techniques with kaon identification have a more favorable signal-to-background ratio compared to the "no PID" technique, resulting in a more pronounced ϕ meson peak in the invariant mass distribution. However, due to the small acceptance of the TOF detector and its poor capability to identify kaons at $p_T > 2.5$ GeV/c (see Section 2.5), these techniques require high statistics data samples and have a limited p_T reach. The "no PID" technique allows us to extend the measurements towards higher p_T as it has substantially larger acceptance and a phase space volume available for daughter kaons not limited by the PID. At the same time, it suffers from a significantly larger combinatorial background, which precludes measurements below $p_T \simeq 2.5$ GeV/c in Au+Au collisions. The three analysis techniques have a significant overlap in p_T and very different sources of systematic uncertainties providing a valuable consistency check.

The summary of analyses is given in Table 3.4.

Species	N_{evt} analyzed	p_T (GeV/c)	Method
p+p	$1.44 \cdot 10^9$	1.3−7.0	"no PID"
	$1.50 \cdot 10^9$	0.9−4.5	"one kaon PID"
d+Au	$63 \cdot 10^6$	1.45−5.1	"no PID"
Au+Au	$824 \cdot 10^6$	2.45−7.0	"no PID"
	$722 \cdot 10^6$	1.1−3.95	"two kaons PID"

Table 3.1: Number of events analyzed and p_T range accessible for the measurements for different $\phi \rightarrow K^+K^-$ analyses.

Each analysis begins with detailed data quality assurance studies. These include the determination of dead, noisy and inactive detector areas in DC/PC1, PC3/EMCal and TOF, discussed in Section 3.2. The next step is event filtering based on the required trigger and event vertex conditions followed by single track selection creteria. After that, tracks are combined into pairs and selection conditions for pairs are applied. The single and pair cuts used in the analyses are summarized in Section 3.3. The pair analysis, described in Section 3.4, includes subtraction of the combinatorial background (see Section 3.4.1 and Section 3.4.2) and raw ϕ meson yield extraction (see Section 3.4.3). Section 3.5 presents corrections, that need to the be applied to the raw data in order to obtain absolutely normalized invariant transverse momentum spectra for the ϕ meson. Single particle Monte Carlo $\phi \rightarrow K^+K^-$ simulations used to derive the correction for limited detector acceptance and limited reconstruction efficiency are described in Section 3.6. Finally, Section 3.11 discusses the evaluation of systematic uncertainties.

3.2 Data quality studies

It is crucial to know exactly the relative performance of all subsystems used in the analysis for every run. For this purpose on a run-by-run basis a number of quality control histograms is collected along with the information used for particle yields extraction. The procedures used to select "good" runs do not differ much from data sample to data sample, so the description below is based on a single example for every type of data filtering.

DC/PC1 To control the DC/PC1 performance in every run we accumulate 2D histograms showing the DC/PC1 occupancy in the α[1] *vs.* wire net number (*board*) space for the East and West arms separately, scaled by the number of minimum bias events in the run. The relation between the *board* number and the azimuthal angle ϕ is given by:

$$\text{EAST arm} : board = (3.72402 - \phi + 0.008047\cos(\phi + 0.87851))/0.01963496 \quad (3.1a)$$

$$\text{WEST arm} : board = (0.573231 + \phi - 0.0046\cos(\phi + 0.05721))/0.01963496 \quad (3.1b)$$

The usage of a hardware related coordinates as *board* (wire net) number, allows an easy identification of malfunctioning detector parts. Regions in the α *vs.* *board* space corresponding to dead, half-dead or problematic regions in the DC-PC1 are completely removed from the analysis. The origin of the dead areas is traced down to hardware problems either in the DC or in the PC1 and confirmed by the logbook. The effect of the fiducial cuts is illustrated in Fig. 3.2.

[1] For the definition of α see Section 2.4.2

After applying the fiducial cuts, we project the DC/PC1 occupancy histograms on the *board*-axis and and normalize the resulting *board* distributions (for the East and West arms) in every run to represent the same integrals and then divide by the corresponding distributions in a reference run. The ratios are fitted to a constant function. Fig. 3.3 shows the fit parameter (*const*) and the fit quality χ^2/NDF for every run. The good runs are selected according to the following criteria:

- $0.96 < const < 1.04$
- $\chi^2/NDF < 2$

PC3/EMCal As mentioned in Section 2.4.4, a valid DC/PC1 track is required to have a matching hit in PC3 or in the EMCal. To control the PC3/EMCal performance in every run we estimate the probability for a charged track in the acceptance of PC3/EMCal to have a 4σ matching hit in one of the detectors. The probability is calculated separately for each EMCal sector acceptance as the ratio of the number of tracks counted in the sector acceptance satisfying the 4σ PC3/EMCal matching condition to the number of tracks counted without any matching requirement. The probability for a charged track to have a 4σ matching to PC3/EMCal is shown in Fig. 3.4. We rejected runs which had a probability different by more than 2% from the mean value of the probability measured in any of the eight sectors (the $\pm 2\%$ bands are indicated by the red lines in Fig. 3.4).

TOF To control the TOF performance we look at the deviation of the average number of kaons per event in each run from the average number of kaons per event in all runs within a given time period. We consider four time periods in Run4, indicated as R1, R2, R3, R4 in the bottom panel of Fig. 3.5, where the detector performance was found approximately constant by looking at the average number of kaons per event in each period. The mean and sigma of the distribution of the average number of kaons per event for each period was determined by fitting it with a Gaussian function. Only runs having an average number of kaons per event within 4σ from the mean of the period are accepted. The 4σ bands are shown by the blue dotted lines in the bottom panel of Fig. 3.5.

3.3 Event selection, single track and pair cuts

This section discusses and summarizes the cuts used in the various $\phi \rightarrow K^+K^-$ analyses described in this thesis.

Collision vertex cut The collision vertex is determined by the BBC's on an event-by-event basis as described in Section 2.3.3. Fig. 3.6 shows the z_{vtx} distributions as seen

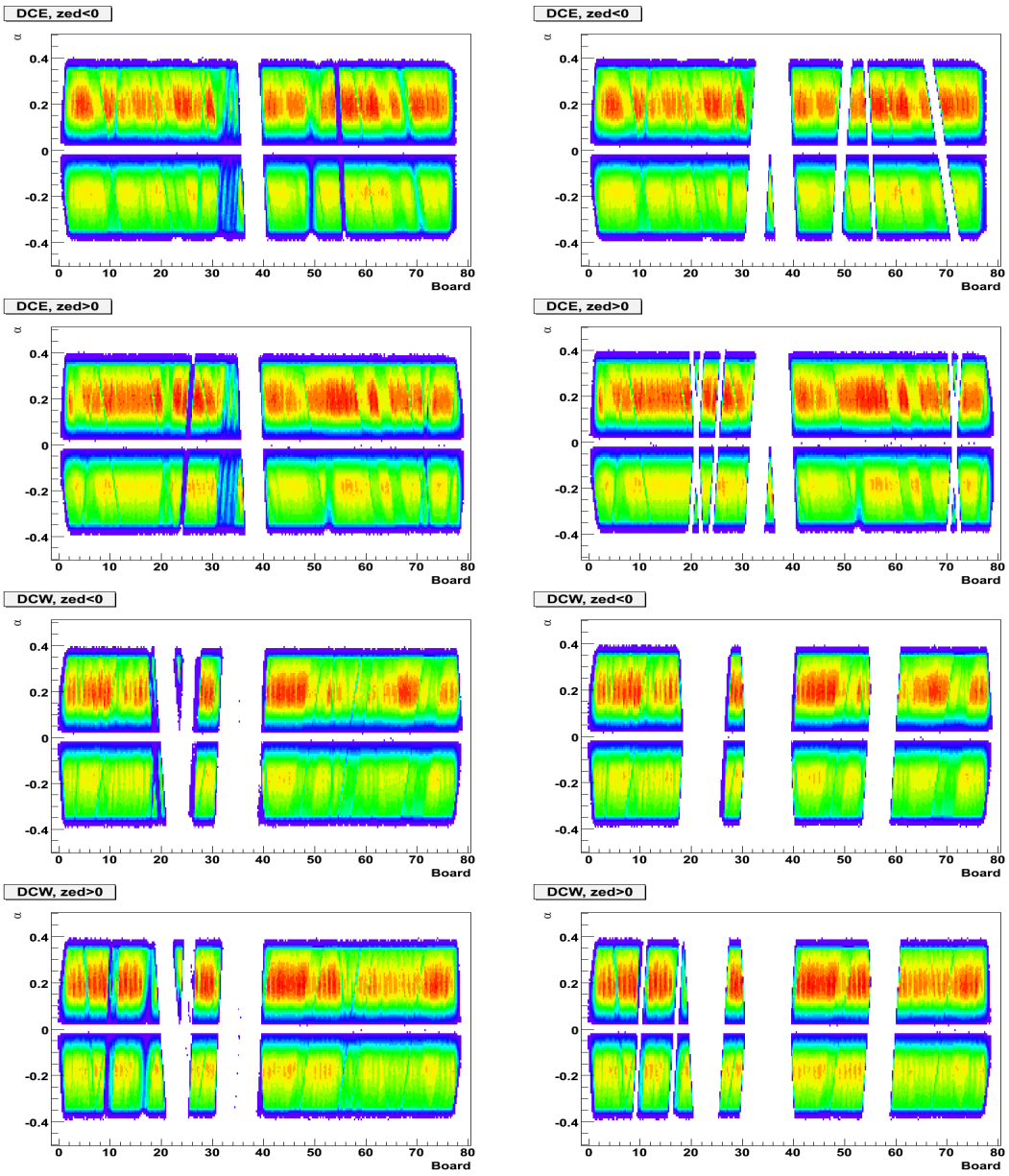

Figure 3.2: DC/PC1 occupancy control histograms before (left) and after (right) fiducial cuts in the Run-4 Au+Au data set. DCE stands for the DC East arm, and DCW for the DC West arm.

in Run-3 d+Au, Run-4 Au+Au and Run-5 p+p collisions. An offline vertex cut $|z_{vtx}| < 30$ cm was applied in every analysis to reduce the probability for produced particles to interact with the material of the central magnet cones. For the Au+Au case the vertex distribution has an offline vertex cut of ± 30 cm applied at the data production level.

Fiducial cuts The fiducial cuts were introduced in order to avoid distortion of the particle distribution near the edges and the dead regions of the detectors through the runs. Fiducial cuts were derived for each data set separately from the occupancy control his-

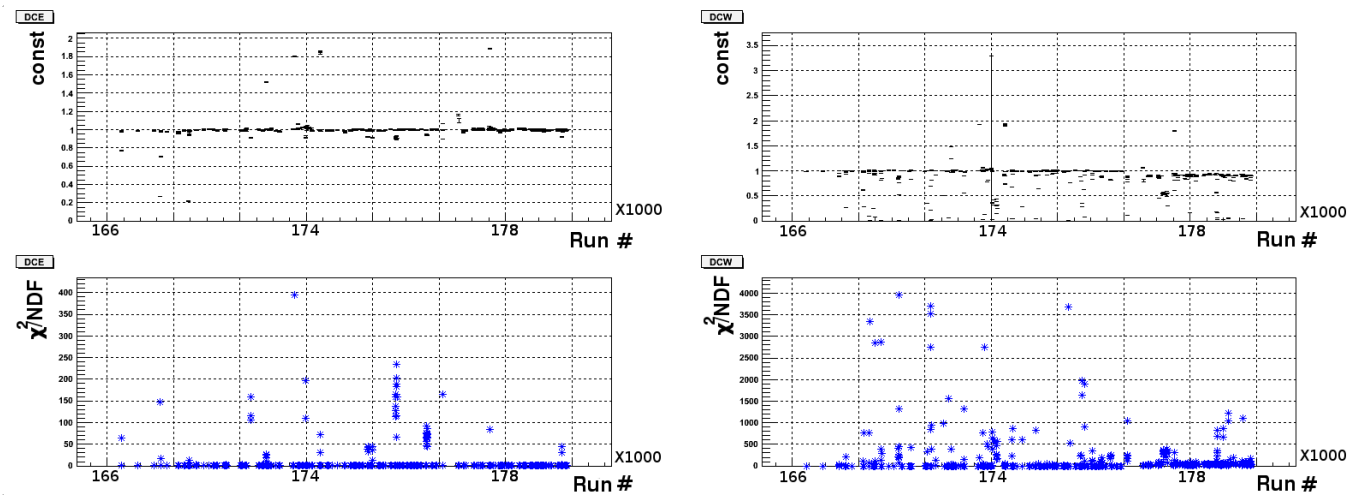

Figure 3.3: The fit parameter (top) and the fit quality (bottom) for the East (left) and West (right) DC arms.

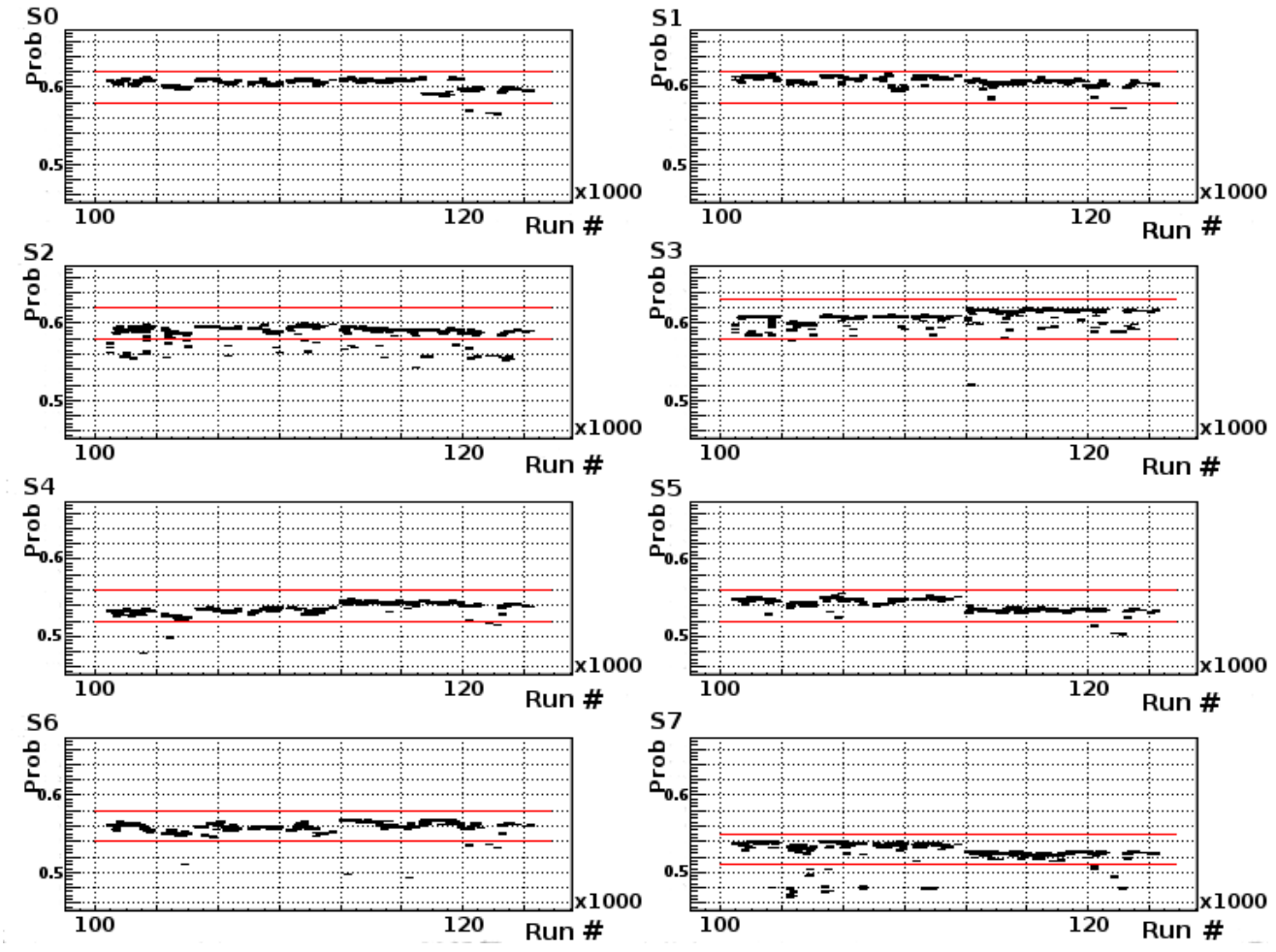

Figure 3.4: The probability for a charged track to have a 4σ matching hit in PC3/EMCal for the eight PC3/EMCal sectors.

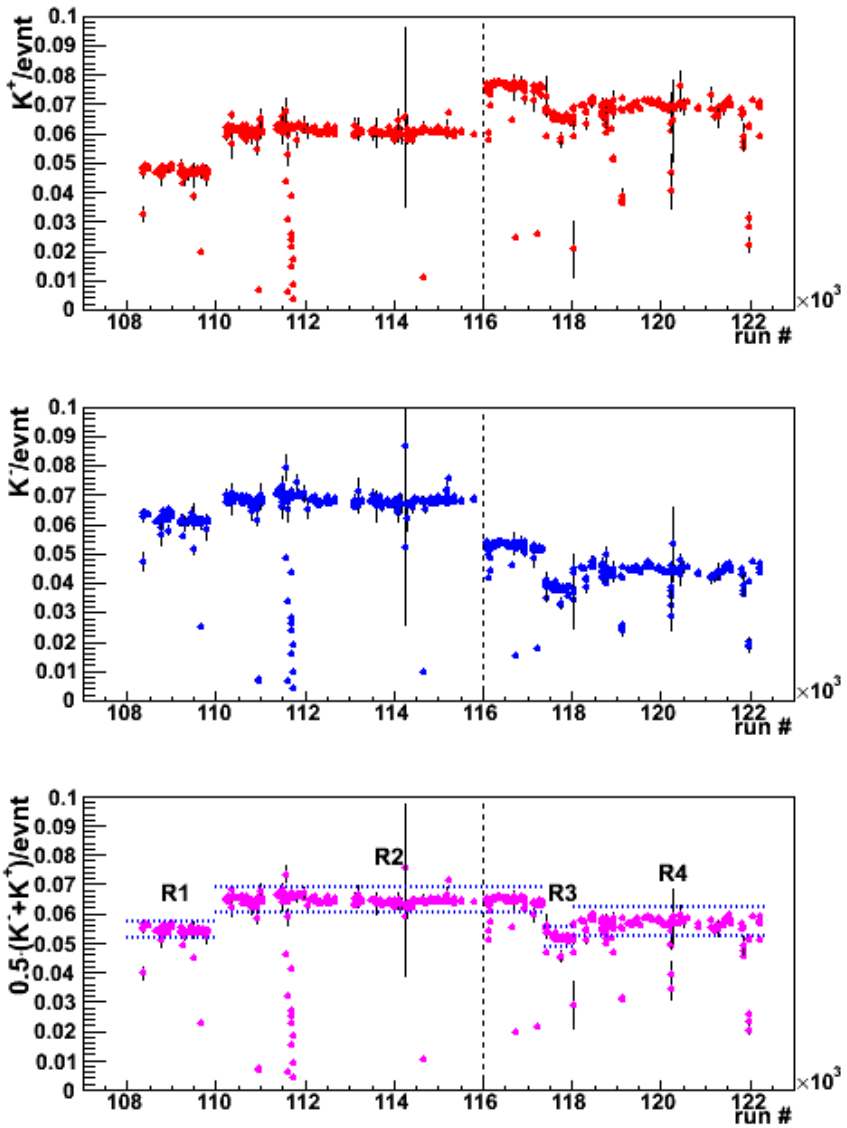

Figure 3.5: Average number of K^+ , K^- and $(K^+ + K^-)/2$ per event and per run. Dashed lines indicates the switch of the magnetic field from "++" to "−−".

tograms for DC/PC1 and TOF subsystems. The effect of fiducial cuts can be seen in Fig. 3.2 for the DC/PC1 acceptance.

Ghost rejection cut As an artifact of the tracking algorithm discussed in Section 2.4.2 it may happen that a particle trajectory gets reconstructed multiple times (usually not more than two), resulting in several tracks having very similar values for almost every parameter. Such tracks are called "DC ghosts" and normally one or both "ghost" tracks are rejected from the analysis. The small difference in ϕ and *zed* (see Section 2.4.2) between "ghost" tracks was used to identify them. Fig. 3.7 shows an example of the Δzed vs. $\Delta\phi$ distributions for any pair of tracks in the DC in the Run-3 *d*+Au data indicating

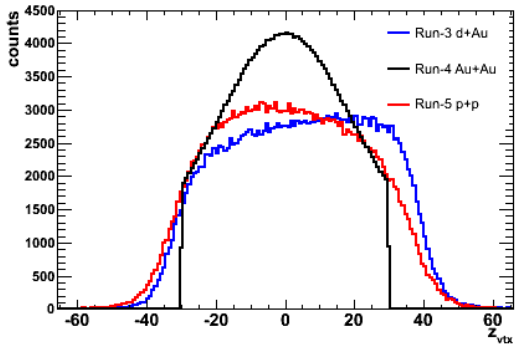

Figure 3.6: The z_{vtx} distributions in Run-3 d+Au (blue), Run-4 Au+Au (black) and Run-5 p+p (red) collisions. The distributions have been normalized to have same integral.

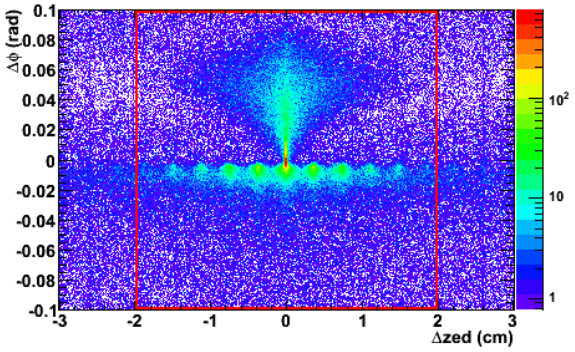

Figure 3.7: Δzed vs. $\Delta\phi$ for pairs of tracks in the DC obtained in Run-3 d+Au "no PID" analysis. The structure in the center of the figure is due to the "DC ghost" phenomenon. The red contour represents the cut boundaries.

the cut boundaries by the red contour. Somewhat more complicated p_T-dependent cuts proposed in [104] were used in Run-4 Au+Au "no PID" analysis (see Table 3.2).

Intruder rejection cut In the $\phi \rightarrow K^+K^-$ analysis of Run-2 Au+Au data [105] it was found that pairs made of opposite sign kaon tracks sharing the same TOF hit result in a spurious extra yield in the invariant mass spectrum of K^+K^- pairs near the region of the ϕ meson peak. The timing information for tracks hitting the same slat in the TOF is corrupted, and should not be used for particle identification, therefore in the Run-4 Au+Au "two kaons PID" analysis both members of the pair were rejected. A similar effect was also observed when two tracks share the same tower in the EMCal, but never when one track is identified in the TOF and the other one in the EMCal [105].

"Sailors" and "same arm" cuts Given the acceptance of the PHENIX central arm, we differentiate between the two different decay topologies possible for a neutral particle decaying into two charged "daughters" illustrated in Fig. 3.8 for $\phi \rightarrow K^+K^-$. If one looks at a pair of oppositely charged tracks from a neutral particle decay in the plane perpendicular to the magnetic field, then the topology where the decay tracks bend away from each other (or first bend toward each other until they cross and then bend away from each other, with the crossing point lying in front of the DC reference radius) is called "sailors" and shown in the left panel, and the topology where the tracks bend toward each other, but with the crossing point lying behind the DC reference radius is called "cowboys", shown in the right panel.

The selection criterion for "sailors" or "cowboys" pairs relies on the values of the track azimuthal angles ϕ measured at the DC reference radius. As illustrated in Fig. 3.8, for the

given magnetic field direction, the ϕ angle for K^- is larger than for K^+ for "sailors", whereas the opposite is true for "cowboys".

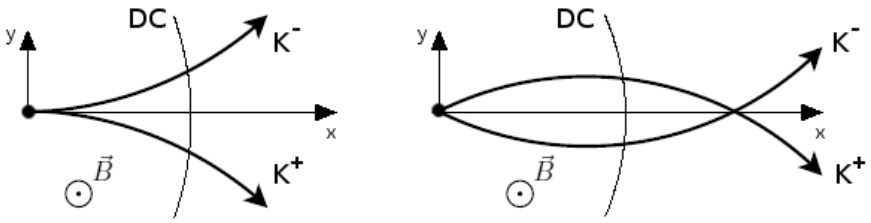

Figure 3.8: "Sailors" (left) and "cowboy" (right) topologies of $\phi \rightarrow K^+K^-$ decay.

Fig. 3.9 shows the correlation between the ϕ angles of negative and positive tracks from all unlike-sign pairs for Run-5 *p*+*p* data in the right panel and from single particle $\phi \rightarrow K^+K^-$ simulation in the left panel (done with the same "−−" magnetic field configuration as in the data). There are several regions that we can distinguish on these plots indicated by roman numbers:

I Tracks are in opposite arms, "cowboys".
II Both tracks are in the West arm, "cowboys".
III Both tracks are in the West arm, "sailors".
IV Both tracks are in the East arm, "cowboys".
V Both tracks are in the East arm, "sailors".
VI Tracks are in opposite arms, "sailors".

It is evident from Fig. 3.9, that in the data all unlike-sign pairs (right panel) uniformly populate the detector acceptance in all six regions, while in the simulation pairs from the ϕ meson decay (left panel) are dominantly concentrated in the regions III and V. With a relatively simple pair cut like selecting only pairs of the "sailors" type or requiring both tracks to be in the same arm, one can effectively reduce the amount of combinatorial pairs by a factor of 2. At the same time the ϕ signal remains almost unaffected.

Explanations for the **track quality cut**, **matching cut** and **PID cut** can be found in Section 2.4.2, Section 2.4.4 and Section 2.5, respectively. The summary of all cuts used for event selection, track selection, as well as pair cuts is presented in Table 3.2.

3.4 Pair analysis and extraction of ϕ meson raw yields

Since there is no way to distinguish kaons from ϕ meson decay from other kaons, all kaon tracks from each event passing the track selection requirements are combined into like-sign and unlike-sign pairs. For each track the components of the 3-momentum vector $\vec{p}$ are measured with the drift chamber (see Section 2.4.2 and Section 2.4.3) as:

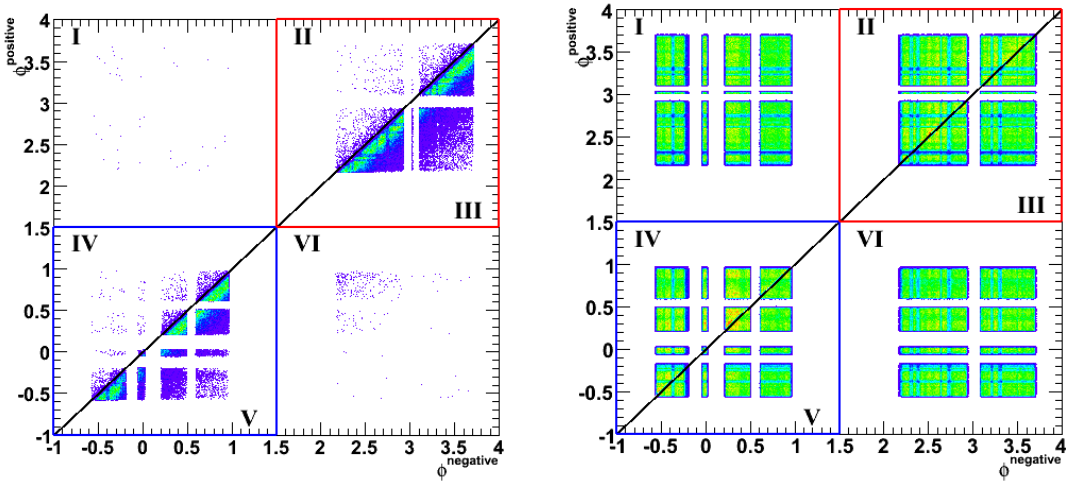

Figure 3.9: Correlation between the ϕ angles of negative and positive tracks from all unlike-sign pairs for Run-5 p+p data (right) and same for single particle $\phi \rightarrow K^+K^-$ simulation (left). Red (blue) lines outline the cuts applied to select pairs with both tracks in the West (East) acceptance. Black line represents the "sailors" cut: pairs to the left from the line are removed by the cut.

$$p_x = p \sin\theta_0 \cos\phi_0 \tag{3.2a}$$

$$p_y = p \sin\theta_0 \sin\phi_0 \tag{3.2b}$$

$$p_z = p \cos\theta_0 \tag{3.2c}$$

The invariant mass and the transverse momentum for the kaon pair is then calculated based on the 2-body decay kinematic as:

$$m^2_{KK} = (E_{K_1} + E_{K_2})^2 - (\vec{p}_{K_1} + \vec{p}_{K_2})^2 \tag{3.3a}$$

$$p^2_{T\ KK} = (p_{x\ K_1} + p_{x\ K_2})^2 + (p_{y\ K_1} + p_{y\ K_2})^2 \tag{3.3b}$$

where $E_{K_{1/2}} = \sqrt{\vec{p}^2_{K_{1/2}} + m^2_K}$ and $m_K = 0.43677$ GeV.

The foreground unlike-sign invariant mass spectrum contains both the ϕ meson signal and an inherent combinatorial background. The kinematic cuts like the sailors cut or one arm cut allow to substantially reduce the combinatorial background but do not fully eliminate it. To estimate the remaining combinatorial background one can apply an event-mixing technique or a fitting procedure. The first method was used in the Run-4 Au+Au "two kaons PID" analysis, and the second one in the analyses of p+p and d+Au data from Run-5 and Run-3 datasets, respectively. In Run-4 Au+Au "no PID" analysis

Cut description	Value	Analysis
Collision vertex	$\lvert z_{vtx}\rvert$ <30 cm	I, II, III, IV, V
Track quality	31 || 51 || 63	I, II, V
	31 || 63	III, IV
Fiducial	see Section 3.6.2	I, II, III, IV, V
p_T of tracks	$0.5\ \text{GeV}/c \leq p_T^{noPID} \leq 4.0\ \text{GeV}/c$	I
	$0.3\ \text{GeV}/c \leq p_T^{noPID} \leq 8.0\ \text{GeV}/c$	II, IV
	$0.3\ \text{GeV}/c \leq p_T^{PID} \leq 2.5\ \text{GeV}/c$	III
	$0.3\ \text{GeV}/c \leq p_T^{noPID} \leq 8.0\ \text{GeV}/c$ $0.35\ \text{GeV}/c \leq p_T^{PID} \leq 2.25\ \text{GeV}/c$	V
Matching	4σ matching in ϕ and z to the PC3 || EMCal (optional)	I, II, IV, V
	3σ matching in ϕ and z to the TOF	III
"Same arm"	(ϕ_1 >1.5 rad && ϕ_2 >1.5 rad) || (ϕ_1 <1.5 rad && ϕ_2 <1.5 rad)	I, II, IV
	(ϕ_1 <1.5 rad && ϕ_2 <1.5 rad)	V
Ghost rejection	$\lvert\Delta zed\rvert \leq 2$ cm && $\lvert\Delta\phi\rvert \leq 0.1$ rad	I
	($\lvert\Delta\phi + 0.065\Delta\alpha\rvert < 0.015$ rad) || ($\lvert\Delta\phi - 0.04\Delta\alpha\rvert < 0.015$ rad) || ($\lvert\Delta zed\rvert < 6.0$ cm && $\lvert\Delta\phi - 0.13\Delta\alpha\rvert < 0.015$ rad)	II
	$\lvert\Delta zed\rvert \leq 0.2$ cm && $\lvert\Delta\phi\rvert \leq 0.03$ rad	III
	$\lvert\Delta zed\rvert \leq 2$ cm && $\lvert\Delta\phi\rvert \leq 0.03$ rad	IV, V
Intruder rejection	$slat_1 \neq slat_2$	III
"Sailors"	$\phi_{positive} > \phi_{negative} + 0.5144 - 0.16 p_T + 0.0125 p_T^2$	I
	$\phi_{positive} > \phi_{negative}$, for "−−" magnetic field runs $\phi_{positive} < \phi_{negative}$, for "++" magnetic field runs	II
	$\phi_{positive} > \phi_{negative}$	IV, V
PID	$\lvert IsK\rvert < 2 \&\& \lvert IsPi\rvert > 2$ for both tracks from a pair	III
	$\lvert IsK\rvert < 3 \&\& \lvert IsPi\rvert > 3$ for at least one track from a pair	V

Table 3.2: Summary of cuts used in the various $\phi \to K^+K^-$ analyses: (I) Run-3 d+Au "no PID" , (II) Run-4 Au+Au "no PID", (III) Run-4 Au+Au "two kaons PID", (IV) Run-5 p+p "no PID" and (V) Run-5 p+p "one kaon PID".

a combination of both methods was used. The aim of the pair analysis is to extract the yield of ϕ mesons out of the yield of inclusive K^+K^- pairs. In all analyses, the raw yields

were extracted by integrating the invariant mass distribution in a window of ± 9 MeV/c^2 around the ϕ meson mass (1.019 GeV/c^2) after subtracting the combinatorial background.

3.4.1 Combinatorial background determined by the event-mixing technique

The event-mixing technique has been proposed by Kopylov [106] and later further developed by Drijard, Fischer, and Nakada [107] and L'Hote [108]. It is based on the fact that there are no physical correlations between unlike-sign tracks in artificially mixed events formed by combining positive charged tracks from one event and negative charged tracks from a different event. The event-mixing procedure generates unlike- and like-sign pair invariant mass spectra for real and mixed events. Under appropriate constraints of "event similarity"[1] the technique allows to reproduce the shape of the uncorrelated part of the combinatorial background.

Event mixing was done using 800 (40 centrality$\times$20 vertex) pools with a rolling buffer of N_{buff}=20 events in the Run-4 Au+Au "two kaons PID" analysis, and using 30 (10 centrality $\times$ 3 vertex) pools with a buffer of N_{buff}=15 events in the Run-4 Au+Au "no PID" analysis. The mixed event spectrum has to be normalized before it is subtracted from the measured one. For the normalization of the mixed event spectrum one can use several methods:

1. Normalize the mixed event unlike-sign mass distribution to the measured $2\sqrt{N_{++}N_{--}}$. The normalization factor α and its error $\Delta\alpha$ are given by:

$$\alpha = \frac{2\cdot\sqrt{N_{++}^{Real}\cdot N_{--}^{Real}}}{N_{+-}^{Mixed}} \qquad \Delta\alpha = \alpha\cdot\sqrt{\frac{1}{4}\left(\frac{1}{N_{++}^{Real}}+\frac{1}{N_{--}^{Real}}\right)+\frac{1}{N_{+-}^{Mixed}}}, \tag{3.4}$$

   where N_{++}^{Real}, N_{--}^{Real} represent the measured integral yield of like-sign pairs and N_{+-}^{Mixed} is the mixed event unlike-sign pair integral yield [109–111]. This method is rigorously valid in the absence of correlations in the like sign spectra.

2. Normalize the mixed event unlike-sign mass distribution to the measured unlike-sign mass distribution above some mass $m > m_0$. This is valid provided that there are no correlations in the measured unlike-sign mass spectrum above m_0.

3. The mixed event technique itself provides an absolute normalization. By construction, with a buffer size of N_{buff}, the normalization factor should be $2N_{buff}$. This is valid if the particle multiplicity in the event follows a Poisson distribution. It is

[1] In the present analyses, events are required to have similar centrality parameters and collision vertex positions.

known that in p+p and in heavy ion collisions the particle multiplicity follows a Negative Binomial distribution rather than a Poisson distribution [112], therefore this normalization is only approximately valid, the magnitude of the normalization distortion is ∼2-3%.

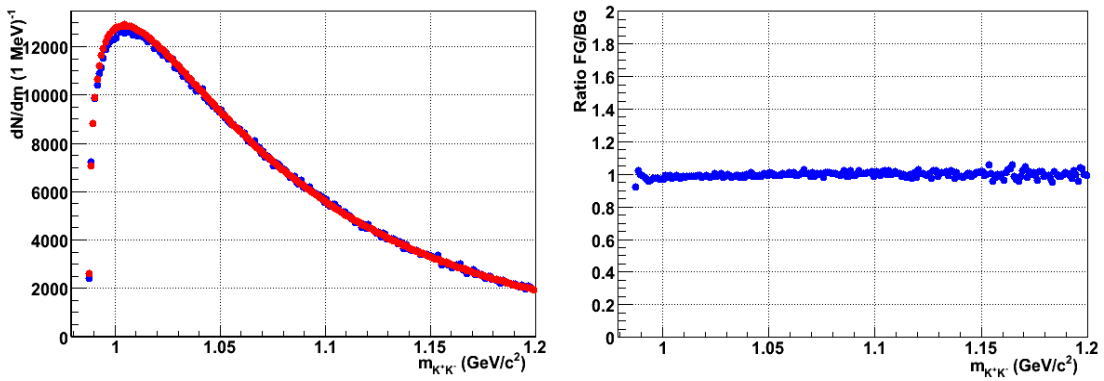

Figure 3.10: Measured (blue) and normalized mixed-event (red) invariant mass spectra of K^-K^- pairs (left) and their ratio obtained for the "++" magnetic field configuration in Run-4 "two kaon PID" analysis.

In the Run-4 "two kaons PID" analysis the first normalization method ($2\sqrt{N_{++}N_{--}}$) was adopted, and the second method was used as an estimate of the systematic error due to the subtraction of the combinatorial background.

In order to check that the mixed-event spectra has the same shape as the combinatorial background one can compare the normalized like-sign spectra of mixed events to the same of real events and their ratios. These ratios were always found to be flat and consistent with unity for all masses as demonstrated in Fig. 3.10 for the "++" magnetic field configuration. The observed deviation from one of less than 2% can be explained by possible correlations in the like-sign spectra from jets or from kaon misidentification.

Fig. 3.11 shows the measured and normalized mixed-event invariant mass spectra of K^+K^- and subtraction of the two, obtained in the Run-4 Au+Au "two kaons PID" analysis.

In the Run-4 Au+Au "no PID" analysis, for every p_T bin the unlike-sign mixed event mass distribution was normalized to the same event unlike-sign mass distribution in the mass range m_{inv} >1.35 GeV/c^2. An example of a real- and normalized mixed-event unlike-sign invariant mass distribution superimposed, and the spectrum resulting after subtracting the two for one of the p_T bins is shown in the left and right panels of Fig. 3.12, respectively. A substantial residual background is seen in the subtracted spectrum. It arises mainly from the abundant correlated pairs from other particle decays ($K^0_s \to \pi^+\pi^-$, $\Lambda \to p\pi^-$, $\rho \to \pi^+\pi^-$, $\omega \to \pi^0\pi^+\pi^-$, etc.) which is not accounted for by the mixed-event

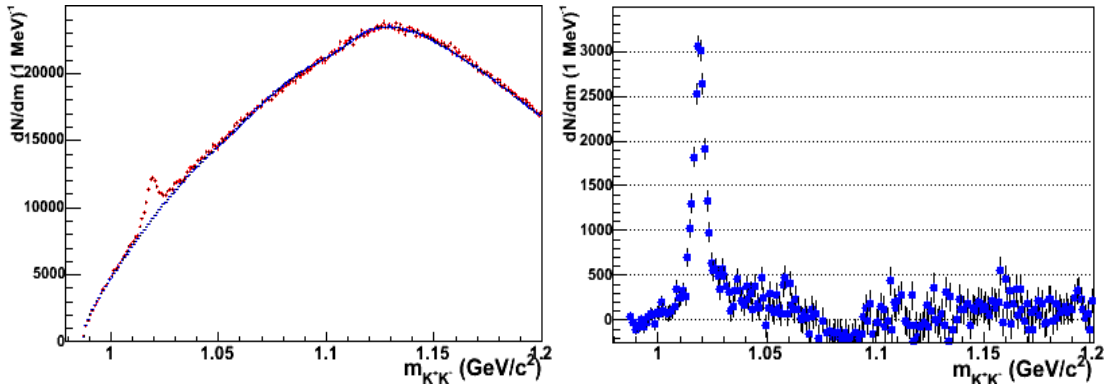

Figure 3.11: The measured (red) and normalized mixed-event (blue) invariant mass spectra of K^+K^- pairs (left) and the subtraction of the two (right) obtained in Run-4 "two kaons PID" analysis.

technique. The residual background is removed using the fitting technique described in the next section.

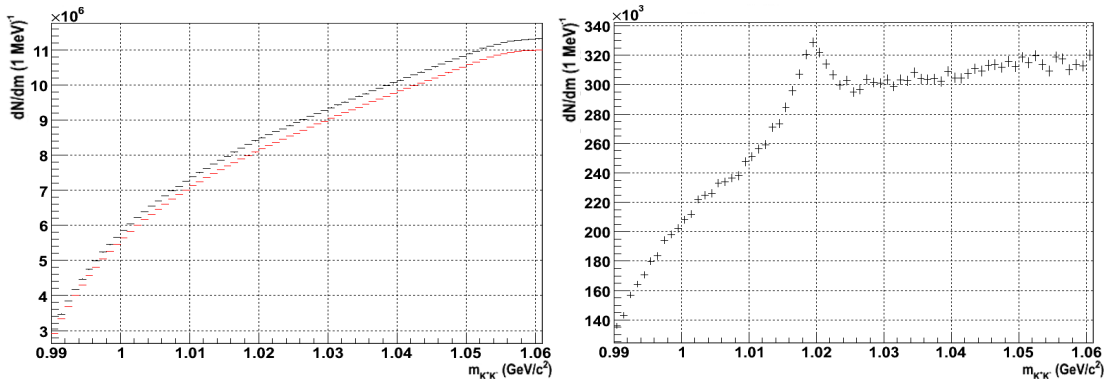

Figure 3.12: The measured (red) and normalized mixed-event (black) invariant mass spectra of K^+K^- pairs (left) and the subtraction of the two (right) for $2 < p_T < 3$ GeV/c obtained in Run-4 "no PID" analysis.

3.4.2 Combinatorial background determined by the fitting technique

In cases where the event-mixing technique is not applicable one can also estimate the combinatorial background by fitting the invariant mass distribution with a Breit-Wigner function for the signal convoluted with a Gaussian (with $\sigma = \sigma_{exp}$ to account for the detector mass resolution) and a polynomial function for the background.

The experimental mass resolution σ_{exp} is estimated by using the $\phi \rightarrow K^+K^-$ zero-width Monte Carlo simulation, described in Section 3.6.1 in which the ϕ meson has zero

width. An example of the reconstructed invariant mass distribution after passing through the entire analysis chain is shown in the left panel of Fig. 3.13. As one can see, the mass distribution has long non Gaussian tails which originate from in-flight decay of kaons. We therefore fit the mass distribution to a Gaussian function with a free σ parameter summed with a parabola in a narrow window around the PDG value of the ϕ meson mass. The fit value of the σ parameter is taken to be the experimental mass resolution. The dependence of σ_{exp} on p_T as observed in the Run-5 and Run-3 "no PID" analyses is shown in the right panel of Fig. 3.13 by the blue and red curves, respectively. The difference in the mass resolution behavior as a function of p_T between Run-5 and Run-3 is mainly attributed to the difference in the magnetic field strength between the two runs.

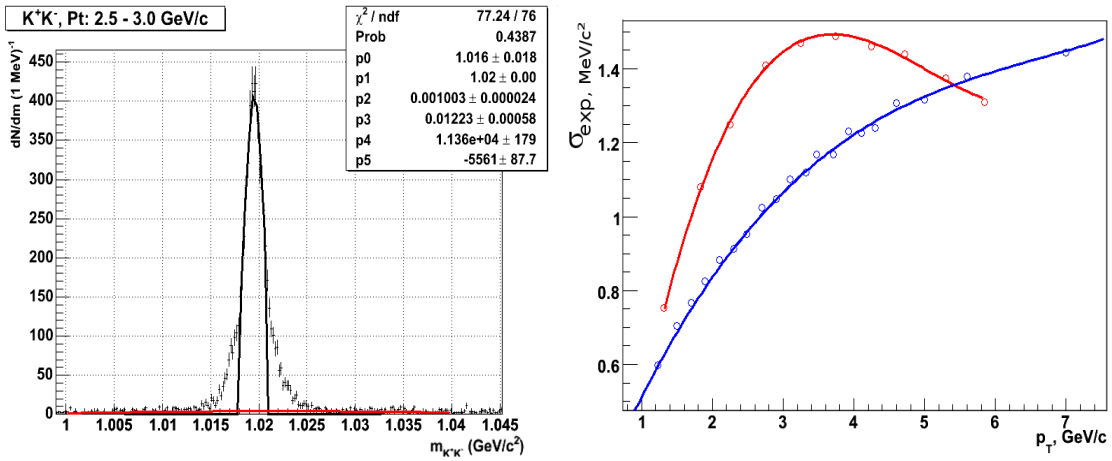

Figure 3.13: Example of the reconstructed invariant mass distribution from the $\phi \rightarrow K^+K^-$ simulation done under the assumption of zero natural width of the ϕ (left). P_T-dependence of the detector mass resolution in Run-5 p+p (blue) and Run-3 d+Au (red) configurations (right).

The ϕ meson invariant mass distribution gets distorted by the wrongly reconstructed momentum of kaons decaying in flight both in data and simulation. This effect is not taken into account in the fitting function described above and in order to get a good match between the fit parameters (Γ or σ) when fitting the invariant mass distributions in data or simulation we allow some freedom on the parameters of the fitting function. The σ parameter of the Gaussian function is always constrained to fall within 90 and 110 percent of the σ_{exp} value derived from the zero-width simulation. The Γ parameter of the Breit-Wigner function is left as a free parameter in the fit of the simulated data, and its extracted value Γ_0 is then used in the real data fitting to constrain the Γ parameter to fall within 90 and 110 percents of the Γ_0 value.

Fig. 3.14 shows the fits used to estimate the combinatorial background in the Run-5 p+p "no PID" analysis. Fig. 3.15 shows examples of the fits used in other analyses.

All fits converge with a good χ^2 probability. The fit parameters Γ and σ obtained from the data (for the fits shown in Fig. 3.14) and the corresponding value from simulation (see Section 3.6.1) are in good agreement, as shown inTable 3.3. One sees that the Γ parameter obtained from the fits is systematically larger than the PDG value of the ϕ meson width. This is due to the fact that the Γ parameter here reflects both the natural width and the widening due to the in flight kaon decays, and hence shall not be interpreted as the natural width of the ϕ meson.

p_T, GeV/c	Data (Sim) Γ, MeV	Data (Sim) σ, MeV
1.2-1.4	5.1±0.7 (4.9)	0.7±0.1 (0.7)
1.4-1.6	5.0±0.7 (4.9)	0.7±0.1 (0.7)
1.6-1.8	4.9±0.7 (4.9)	0.9±0.2 (0.7)
1.8-2.0	5.4±0.8 (4.7)	0.9±0.1 (0.9)
2.0-2.2	4.8±0.5 (4.9)	0.8±0.1 (0.8)
2.2-2.4	5.3±0.1 (4.7)	1.0±0.1 (1.0)
2.4-2.6	4.7±0.5 (4.7)	1.0±0.2 (1.1)
2.6-2.8	5.1±0.5 (5.3)	1.0±0.2 (1.0)
2.8-3.0	5.2±0.5 (5.1)	1.2±0.2 (1.0)
3.0-3.4	5.2±1.1 (5.5)	1.2±0.2 (1.2)
3.4-3.6	6.0±0.7 (5.7)	1.3±0.2 (1.2)
3.6-4.0	6.0±0.4 (6.0)	1.3±0.1 (1.2)
4.0-5.0	6.4±1.0 (6.2)	1.3±0.2 (1.2)
5.0-6.0	6.3±0.3 (6.3)	1.2±0.2 (1.3)
6.0-8.0	6.6±0.2 (6.4)	1.5±0.04 (1.4)

Table 3.3: Width of the Breit-Wigner and Gaussian functions obtained from fits of the ϕ meson line shape for different p_T bins in Run-5 p+p "no PID" analysis.

If $f(x) = \sum_{i=0}^{i=n} a_i x^i$ is the polynomial function for the background and $I = \int_{m_0-\Delta m}^{m_0+\Delta m} f(x)dx$ is the integral of $f(x)$ over the mass range $[m_0 - \Delta m, m_0 + \Delta m]$, then we can express the a_0 coefficient using I and the coefficients $a_1, \ldots, a_n$, and rewrite $f(x)$ as

$$f(x) = \sum_{i=1}^{i=n} a_i x^i + \frac{I}{2\Delta m} - \frac{1}{2\Delta m} \sum_{i=1}^{i=n} \frac{a_i}{i+1} \left((m_0 + \Delta m)^{i+1} - (m_0 - \Delta m)^{i+1} \right) \tag{3.5}$$

It is practical to use I as a fitting parameter instead of a_0. In this case, the error on this parameter, ΔI, reflects the statistical error on the subtracted background yield and can be easily propagated to the statistical error on the raw ϕ meson yield.

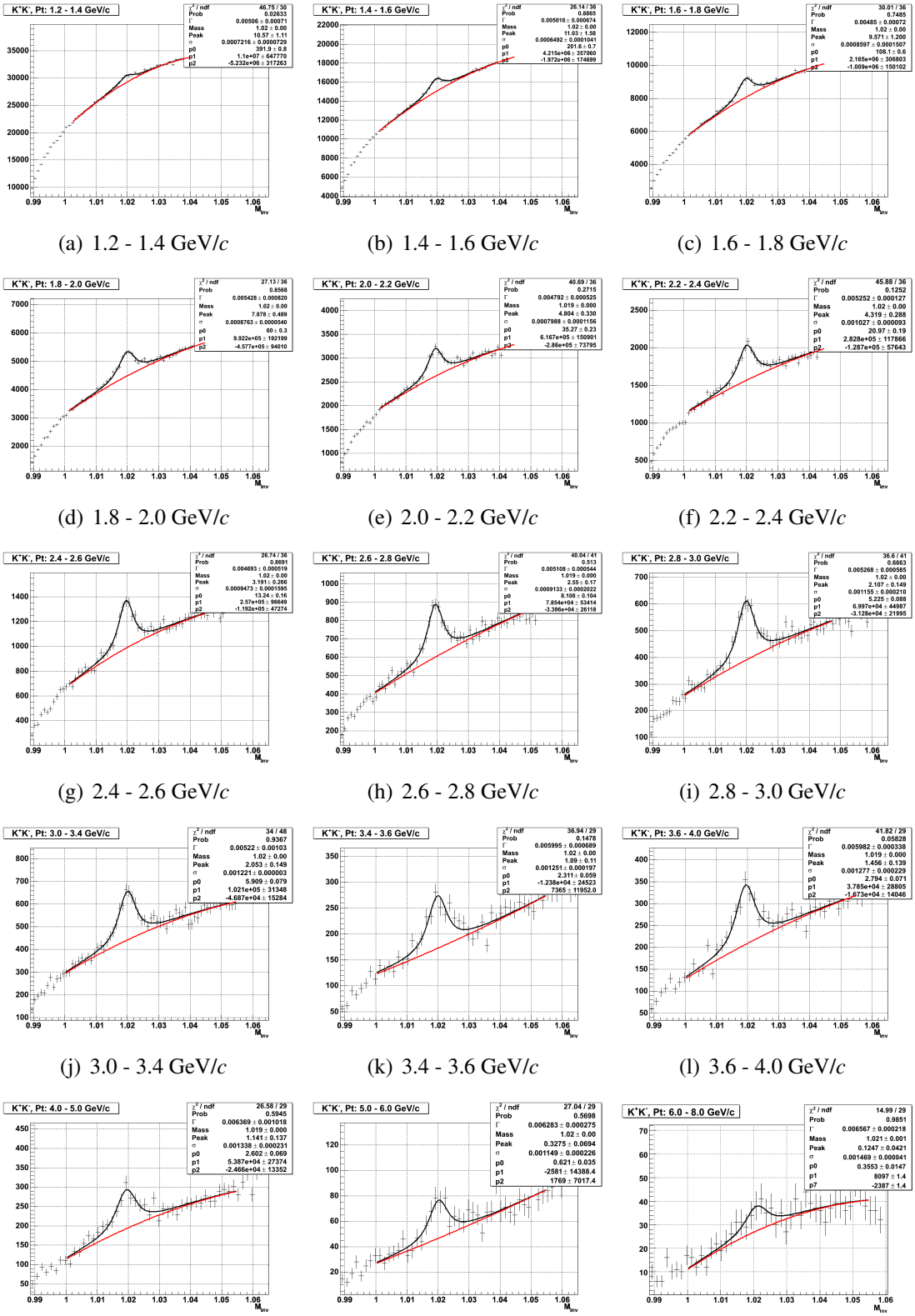

(a) 1.2 - 1.4 GeV/c (b) 1.4 - 1.6 GeV/c (c) 1.6 - 1.8 GeV/c

(d) 1.8 - 2.0 GeV/c (e) 2.0 - 2.2 GeV/c (f) 2.2 - 2.4 GeV/c

(g) 2.4 - 2.6 GeV/c (h) 2.6 - 2.8 GeV/c (i) 2.8 - 3.0 GeV/c

(j) 3.0 - 3.4 GeV/c (k) 3.4 - 3.6 GeV/c (l) 3.6 - 4.0 GeV/c

(m) 4.0 - 5.0 GeV/c (n) 5.0 - 6.0 GeV/c (o) 6.0 - 8.0 GeV/c

Figure 3.14: Fits to the invariant mass distributions used to estimate the combinatorial background in Run-5 p+p "no PID" analysis, as a function of p_T.

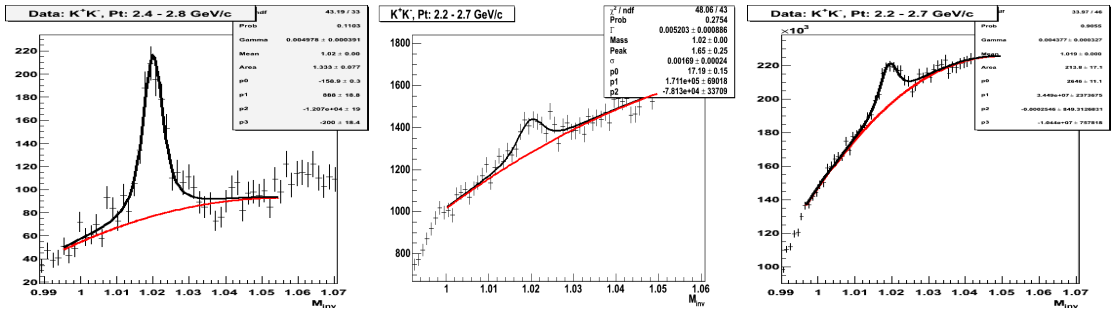

Figure 3.15: Examples of fits used to estimate the combinatorial background: Run-5 "one kaon PID" (left), Run-3 "no PID" (middle), Run-4 "no PID" (right). The red solid lines are the backgrounds.

3.4.3 Raw yield extraction

Event-mixing technique Let us call $\mathcal{FG}(m, p_T)$ - the invariant mass distribution constructed using real pairs for a given p_T bin and $\mathcal{BG}(m, p_T)$ - the corresponding one for mixed pairs. We define $N^{\phi}_{FG}(p_T)$ and $N^{\phi}_{BG}(p_T)$ as:

$$N^{\phi}_{FG}(p_T) = \int_{m_0-\Delta m}^{m_0+\Delta m} \mathcal{FG}(m, p_T)dm \qquad N^{\phi}_{BG}(p_T) = \int_{m_0-\Delta m}^{m_0+\Delta m} \mathcal{BG}(m, p_T)dm \tag{3.6}$$

where m_0 is the ϕ meson mass of 1.019 GeV/c^2, Δm defines a window of 9 MeV/c^2 used for the ϕ yield extraction. Then the raw ϕ yield in a given p_T bin is $N^{\phi}_{raw} = N^{\phi}_{FG}(p_T) - \alpha \cdot N^{\phi}_{BG}(p_T)$, where α is the normalization factor defined in Section 3.4.1. The error in the ϕ yield is calculated by standard propagation of errors as:

$$\Delta N^{\phi}_{raw} = \sqrt{N^{\phi}_{FG} + \alpha^2 N^{\phi}_{BG} + (\Delta\alpha)^2 (N^{\phi}_{BG})^2} \tag{3.7}$$

Fitting technique In the analyses of p+p and d+Au data, where no mixed event background subtraction was used, the raw yield in a given p_T bin is equal to $N^{\phi}_{raw} = N^{\phi}_{FG}(p_T) - I(p_T)$, where N^{ϕ}_{FG} is defined in Eq. 3.6 and I is the integral of the background function (see Section 3.4.2) over a ±9 MeV/c^2 window around the ϕ mass. The error in the ϕ yield is given by:

$$\Delta N^{\phi}_{raw} = \sqrt{N^{\phi}_{FG} + (\Delta I)^2} \tag{3.8}$$

where ΔI is the error in the integral I, defined, as explained in the previous section, using the error in the parameters resulting from the fit.

In the Run-4 "no PID" Au+Au analysis, the mixed event background was subtracted fist and then the residual background was estimated using the fitting technique. The raw ϕ yield in a given p_T bin in this case is calculated as $N^{\phi}_{raw} = N^{\phi}_{FG}(p_T) - \alpha \cdot N^{\phi}_{BG}(p_T) - I(p_T)$,

where N^{ϕ}_{FG} and I are same as above, and N^{ϕ}_{BG} is defined in Eq. 3.6. The error in the ϕ yield is still evaluated by Eq. 3.8 because the error arising from the subtraction of the mixed event background is translated to the error in the integral of the background function.

3.5 Absolute normalization and corrections to the raw yields

The main physics quantity extracted from these analyses is the invariant p_T distributions of the ϕ meson. For that the raw yields should be corrected for the limited detector acceptance, reconstruction and trigger efficiency, multiplicity effects and various analysis cuts. The invariant ϕ meson yield per MB triggered event in every p_T bin is given by:

$$\frac{1}{2\pi p_T}\frac{d^2N}{dp_T dy} = \frac{N^{\phi}_{raw}(p_T)}{2\pi p_T \cdot N_{events} \cdot \varepsilon_{emb} \cdot \varepsilon_{rbr} \cdot CF(p_T) \cdot BR \cdot \Delta p_T} \cdot \frac{\varepsilon_{BBC}}{\varepsilon_{bias}}, \tag{3.9}$$

where:

- $N^{\phi}_{raw}(p_T)$ is the raw ϕ yield (see Section 3.4.3).
- $CF(p_T)$ is the correction factor to account for detector acceptance and reconstruction efficiency (see Section 3.7), derived from the single particle Monte Carlo simulations (see Section 3.6).
- N_{events} is the number of analyzed events.
- ε_{rbr} is the efficiency due to variations in the detector performance from run to run (see Section 3.8).
- ε_{emb} is the pair embedding efficiency which accounts for the reconstruction losses due to detector occupancy (see Section 3.9).
- Δp_T is the bin size.
- BR is the $\phi \rightarrow K^+K^-$ branching ratio equal to 0.491 [68].
- ε_{BBC} is the BBC efficiency for the Minimum Bias collisions (see Section 2.6).
- ε_{bias} is the BBC trigger bias (see Section 2.6).

All these corrections are described in the following sections with the exception of ε_{BBC} and ε_{bias} corrections discussed in Section 2.6.

3.6 Monte Carlo simulations

Single-particle Monte Carlo is the primary tool to correct the raw yields due to limitations of detector acceptance and reconstruction efficiency.

The heart of the PHENIX simulation software is the "PHENIX Integrated Simulation Application" (PISA) which is based on the GEANT3 code [113] and supports 24 different event generator interfaces. The PHENIX detector as implemented in PISA is shown in Fig. 3.16. The *HIJING* [114] and *PYTHIA* [115] generators are used in PHENIX as the default full event generators for nucleus-nucleus collisions and proton-proton collisions, respectively. The single-particle generator *EXODUS*, that was developed within PHENIX, is commonly used for single particle event generation.

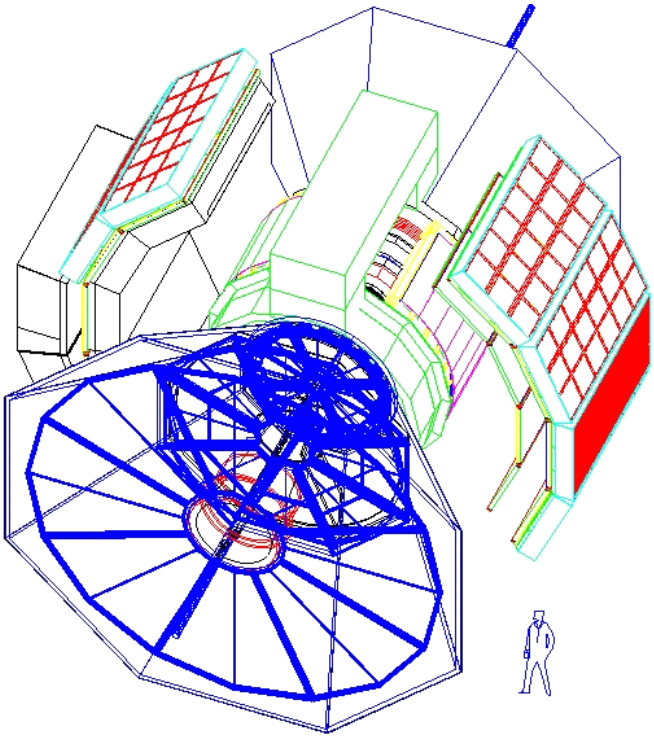

Figure 3.16: The PHENIX detector as implemented in PISA.

The simulation of the $\phi \rightarrow K^+K^-$ is done in three stages. The first stage is the generation of the primary ϕ mesons using the *EXODUS* generator[1]. In the second stage, the resulting output is passed through PISA. Once the primary particle is fed to PISA, the program tracks the particle, it's decay products as well as the products of interactions of primary and secondary particles with matter. The output from PISA contains information about the hits produced as the tracked particles pass through the sensitive parts of each detector subsystem on an event-by-event basis. The third stage is the reconstruction of the PISA hits file. The PHENIX reconstruction software [95] converts PISA hits into digitized detector signals that mock the response of each subsystem to real particles from the collisions. Since the simulation output file format replicates the one utilized in the

[1] It is also possible to decay the ϕ meson into kaons using *EXODUS* decay machinery.

reconstruction of the real data, the simulated data are processed with the same analysis code as used for the data.

3.6.1 Simulation projects details

Table 3.4 summarizes the details of the simulation projects used in the various analyses. The ϕ mesons were generated with a uniform distribution for the azimuthal angle ϕ, rapidity y, and vertex z_{vtx} within the ranges specified in Table 3.4. The p_T distribution of the primary ϕ mesons in all simulation projects, with the exception of the Run-4 "two kaons PID" analysis, was chosen to be flat to provide enough statistics for acceptance and reconstruction efficiency studies. In the simulation made for Run-4 "two kaons PID" analysis, an exponential p_T distribution $dN/dp_T = p_T e^{-m_T/T}$ with an inverse slope parameter $T = 440$ MeV, was used. A Gounaris-Sakurai parameterization [116] with the natural width parameter Γ set to the PDG value or to zero was used to define the ϕ meson spectral shape. The shape of the reconstructed ϕ meson invariant mass distribution depends on two major factors: the mass resolution of the detector, which depends on p_T, and the natural width of the ϕ meson. It is quite a complicated task to disentangle these two contributions having only the invariant mass distribution where these two factors are convoluted. To extract the mass resolution of the detector a separate simulation, with the ϕ meson natural width parameter Γ set to zero, was performed.

Analysis	Configuration	N_{evt}	y	ϕ, rad	p_T range, GeV/c	z_{vtx}, cm	Γ, MeV
Run-3 "no PID"	Run-3	$4{\cdot}10^6$	±0.6	$0-2\pi$	$0.0-8.0$	±30	0.0
	Run-3	$4{\cdot}10^6$	±0.6	$0-2\pi$	$0.0-8.0$	±30	PDG
Run-4 "two kaons PID"	Run-4	$5{\cdot}10^7$	±0.6	$0-2\pi$	$0.0-10.0$	±30	PDG
Run-4/Run-5 "no PID"	Run-5	$2{\cdot}10^6$	±0.5	$0-2\pi$	$0.5-8.0$	±30	0.0
	Run-4	$2{\cdot}10^6$	±0.5	$0-2\pi$	$8.0-11.0$	±30	0.0
	Run-5	$5{\cdot}10^6$	±0.5	$0-2\pi$	$0.5-8.0$	±30	PDG
	Run-4	$2{\cdot}10^6$	±0.5	$0-2\pi$	$8.0-11.0$	±30	PDG
Run-5 "one kaon PID"	Run-5	$2{\cdot}10^6$	±0.5	$0-2\pi$	$0.5-8.0$	±30	0.0
	Run-5	$2{\cdot}10^7$	±0.5	$0-2\pi$	$0.5-5.5$	±30	PDG

Table 3.4: Summary of the simulation projects used in the various analyses.

3.6.2 Comparison of fiducial acceptances in simulation and data

It is crucial that the MC simulations match each detector's characteristics used in the analysis as accurately as possible. To check this, one can compare the track distribution both in data and simulation. The description below explains the procedure used in the Run-5 "one kaon PID" analysis to ensure that the fiducial acceptance in simulation is the same as in data.

The same DC/PC1 fiducial acceptance cuts applied to the data, defined by the procedure described in Section 3.2, were applied also to the simulated data. Fig. 3.17 shows two-dimensional DC/PC1 occupancy histograms in the α vs. *board* space (see Section 3.2 for the *board* coordinate definition). For this comparison the α angle distribution in simulation (originally flat) was weighted according to the α angle distribution seen in data. The simulation histograms were normalized to represent the same total integral as in the data. The DC/PC1 fiducial acceptances in data and simulation are in good agreement as demonstrated in Fig. 3.18 showing the projections of the α vs. *board* distribution on the *board*-axis for data and simulation overlaid.

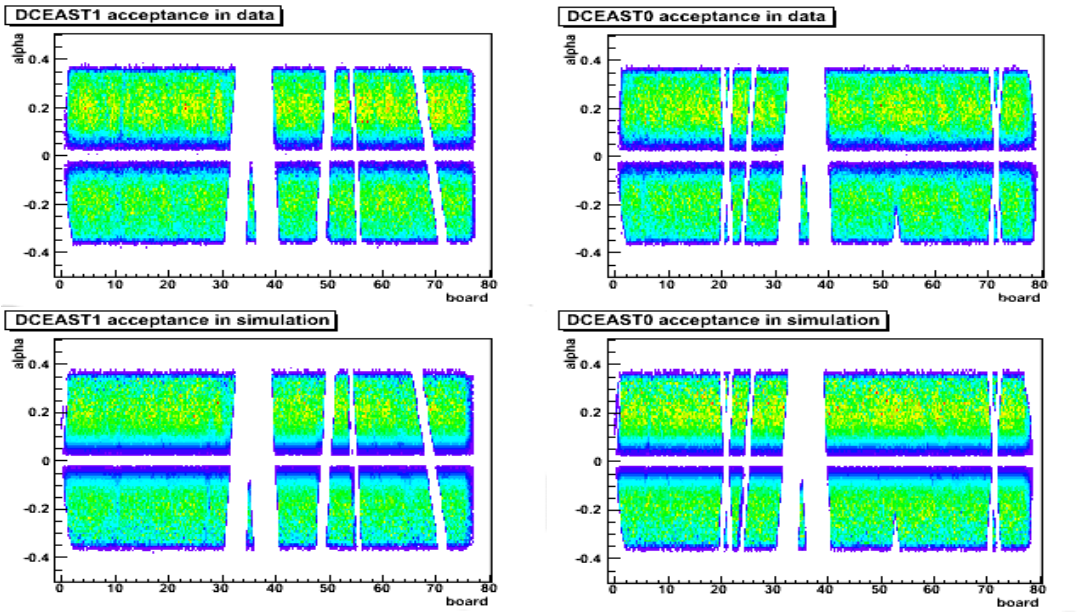

Figure 3.17: DC/PC1 East North (left) and South (right) fiducial acceptances as seen in the data (top) and in the simulation (bottom) for "one kaon PID" Run-5 analysis.

The approach used to compare the TOF fiducial acceptances in data and simulation is similar. The two-dimensional scatter plots of the track projections onto the TOF plane are shown in Fig. 3.19 for data and simulation. The difference in the acceptance shape for positive and negative charged tracks comes from the imprinting of the DC ineffective areas, which depend on the charge of the particle, onto the TOF acceptance. For this

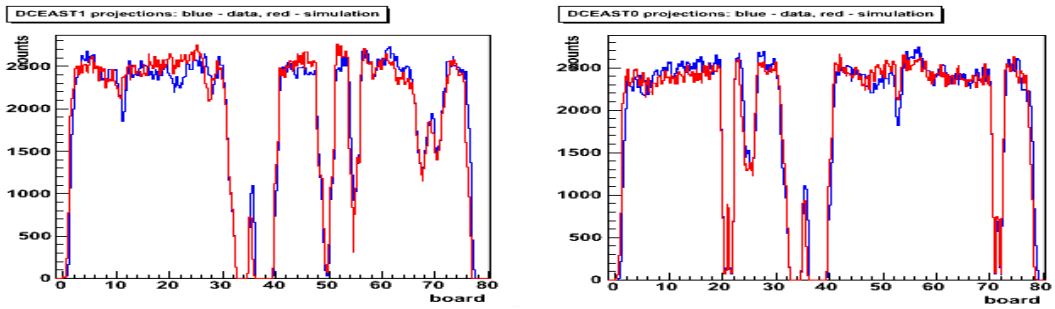

Figure 3.18: Fiducial comparison between data (blue) and simulation (red) for the DC *board* distributions for "one kaon PID" Run-5 analysis. The comparison for the East North part of the DC/PC1 acceptance is shown in the left panel and for the East South part in the right panel.

comparison the p_T distribution of tracks in simulation was weighted according to that of the data. The simulation histograms were normalized to represent the same total integral as in the data. The TOF fiducial acceptances in data and simulation are in good agreement. This is seen in Fig. 3.20 that shows the projections of the $ptofz$ vs. $ptofy$[1] distributions on the horizontal and vertical axes for data and simulation overlaid.

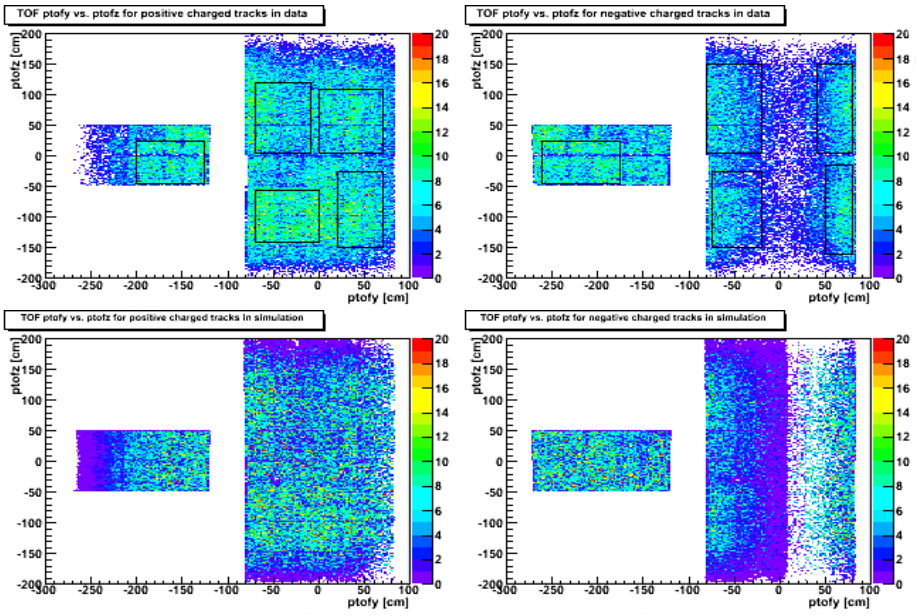

Figure 3.19: TOF fiducial acceptances for positive (left) and negative (right) charged tracks as seen in the data (top) and in the simulation (bottom) for "one kaon PID" Run-5 analysis.

[1] $ptofz$ and $ptofy$ are the z and y coordinates of the track projection onto the TOF plane, respectively.

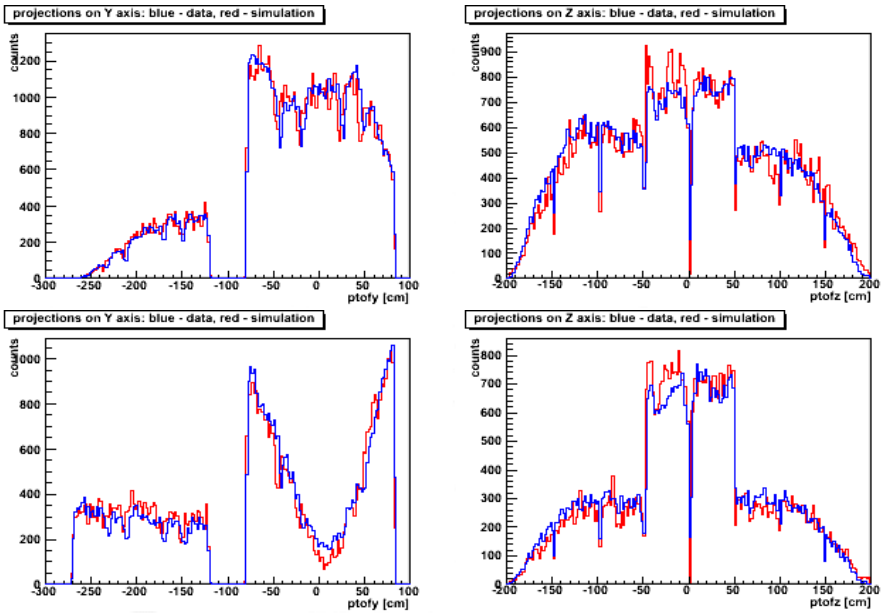

Figure 3.20: Fiducial comparison between data (blue) and simulation (red) for the $ptofy$ (left) and $ptofz$ (right) distributions for "one kaon PID" Run-5 analysis. The $ptofy$ and $ptofz$ are generated by projecting scattered plots shown in Fig. 3.19 on the vertical and horizontal axes respectively. The comparison for positive charged tracks is shown in the top panels and for negative charged tracks in the bottom panels.

3.7 Acceptance and reconstruction efficiency correction

The simulated data files are subject to the same analysis procedure as applied to the real data. The correction factor $CF(p_T)$ for a given p_T bin is defined by the fraction of ϕ mesons generated within the bin that gets reconstructed. This correction factor represents the geometrical acceptance and the pair reconstruction efficiency and also takes into account the detector mass resolution. One should note that the p_T of the generated ϕ meson does not coincide with the p_T of the reconstructed ϕ meson due to the limited detector momentum resolution. If we have a spectrum which is a steeply falling function of p_T, then for two adjacent bins there are always more feed-downs from the bin with lower p_T to the bin with higher p_T than vice versa. Since most of the simulated data were generated with a flat p_T distribution (see Section 3.6.1), the difference in the p_T distribution slopes between the real data and the simulations is corrected by the following procedure:

1. Determine the invariant p_T spectrum of measured ϕ mesons using the acceptance and reconstruction efficiency corrections derived with flat simulated p_T spectra.
2. Fit the invariant p_T spectrum of ϕ mesons.
3. Weight the generated p_T spectrum of ϕ mesons to match the measured one.
4. Recalculate the acceptance and reconstruction efficiency corrections.

5. Determine the invariant p_T spectrum of measured ϕ mesons using the acceptance and reconstruction efficiency corrections derived with the weighted generated p_T spectra.

Normally, the steps 2 to 5 are repeated several times, although subsequent iterations do not introduce any significant modification to the acceptance and reconstruction efficiency correction function.

The correction factor for a given p_T bin is defined by: $CF(p_T) = \frac{N^{rec}(p_T)}{N^{gen}(p_T)}$, where N^{gen} and N^{rec} represent the number of generated and reconstructed ϕ mesons in that bin, respectively. Fig. 3.21 shows the correction factors as a function of p_T obtained in the different analyses. The difference between the correction factors for Run-4 Au+Au and Run-5 p+p "no PID" analyses is due to different fiducial acceptances and different cuts in these two experimental periods. Also one can see that the correction factor in Run-3 "no PID" analysis is smaller compared to Run-4/5 "no PID" analyses. This effect can be explained by the difference in the magnetic field configurations in Run-3 and later runs. The correction factor for Run-4 "two kaons PID" is about a factor of 10 smaller compared to that in Run-5 "one kaon PID" analysis due to the small acceptance of the TOF detector.

3.8 Run-by-run efficiency correction

In a complex detector like PHENIX, performance variations over time are unavoidable. The severe filtering of data based on the DC/PC1 occupancy (see Section 3.2) applied in all analyses described in this thesis, but the Run-4 "two kaons PID" analysis, allowed to reach a level of performance stability such that there is no further correction required to account for any run-by-run variation. However, in the Run-4 Au+Au "two kaons PID" analysis, the selection of runs used in the analysis was based on the average number of kaons per event in each run (see Section 3.2). The average number of kaons per event, shown as a function of run number in the bottom panel of Fig. 3.5, is not stable with time. The top panel of Fig. 3.22 shows the single kaon run-by-run efficiency $\varepsilon_{K^{+/-}}$ derived by normalizing the average number of $K^{+/-}$ per each run to the same in the reference run 116537[1]. The relative K^+K^- pair efficiency, shown in the middle panel of Fig. 3.22, is defined as the product of the single kaon efficiencies $\varepsilon_{K^+}\varepsilon_{K^-}$. The average pair efficiency weighted over the number of analyzed events in each run, shown in the bottom panel of Fig. 3.22, evaluated by Eq. 3.10 was taken as the run-by-run efficiency. It was found to be 0.98 for the "++" and 0.82 for the "−−" field data samples.

[1] Run 116537 was used to tune fiducial acceptance and detector efficiency in the Monte Carlo simulation for Run-4 Au+Au analyses.

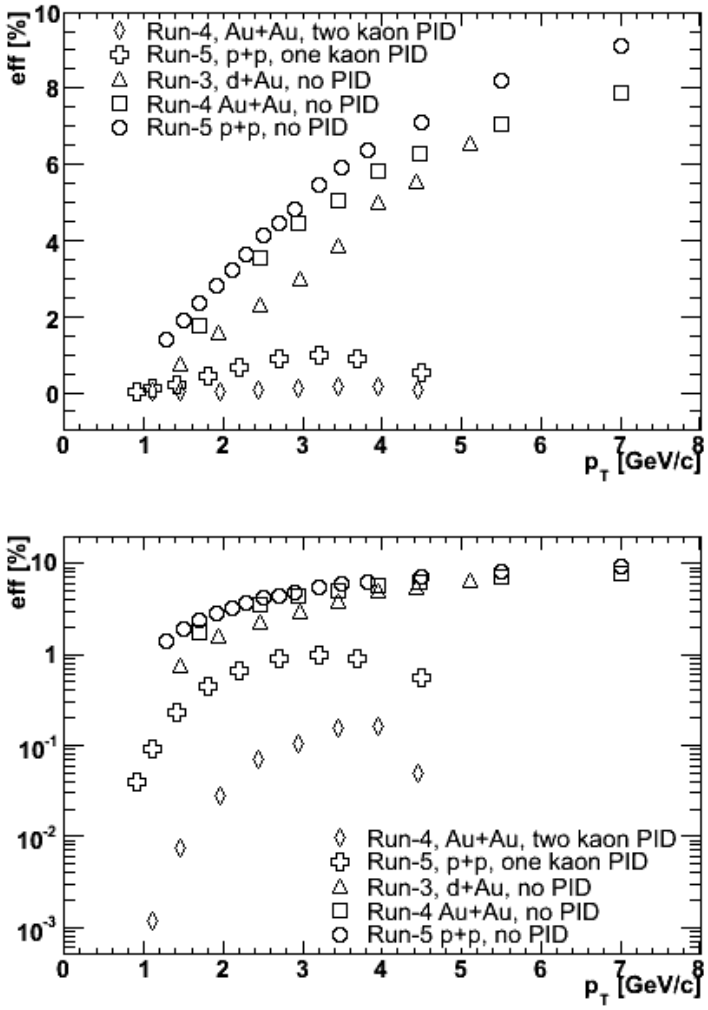

Figure 3.21: Correction factors as a function of p_T shown on linear (top) and logarithmic (bottom) scale.

$$\varepsilon_{rbr} \equiv \langle \varepsilon_{K^+} \varepsilon_{K^-} \rangle = \frac{\sum_i \varepsilon_{K^+}^{run\ i} \cdot \varepsilon_{K^-}^{run\ i} \cdot N_{evt}^{run\ i}}{\sum_i N_{evt}^{run\ i}} \tag{3.10}$$

3.9 Embedding efficiency correction

In the high multiplicity environment of heavy-ion collisions the track reconstruction efficiency decreases with increasing detector occupancy (or centrality). The event multiplicity effects on the track reconstruction efficiency were studied by embedding the GEANT [113] hits produced by single kaons from the $\phi \rightarrow K^+K^-$ simulation into the raw detector hits of events of different centrality classes. Comparing the number of tracks recon-

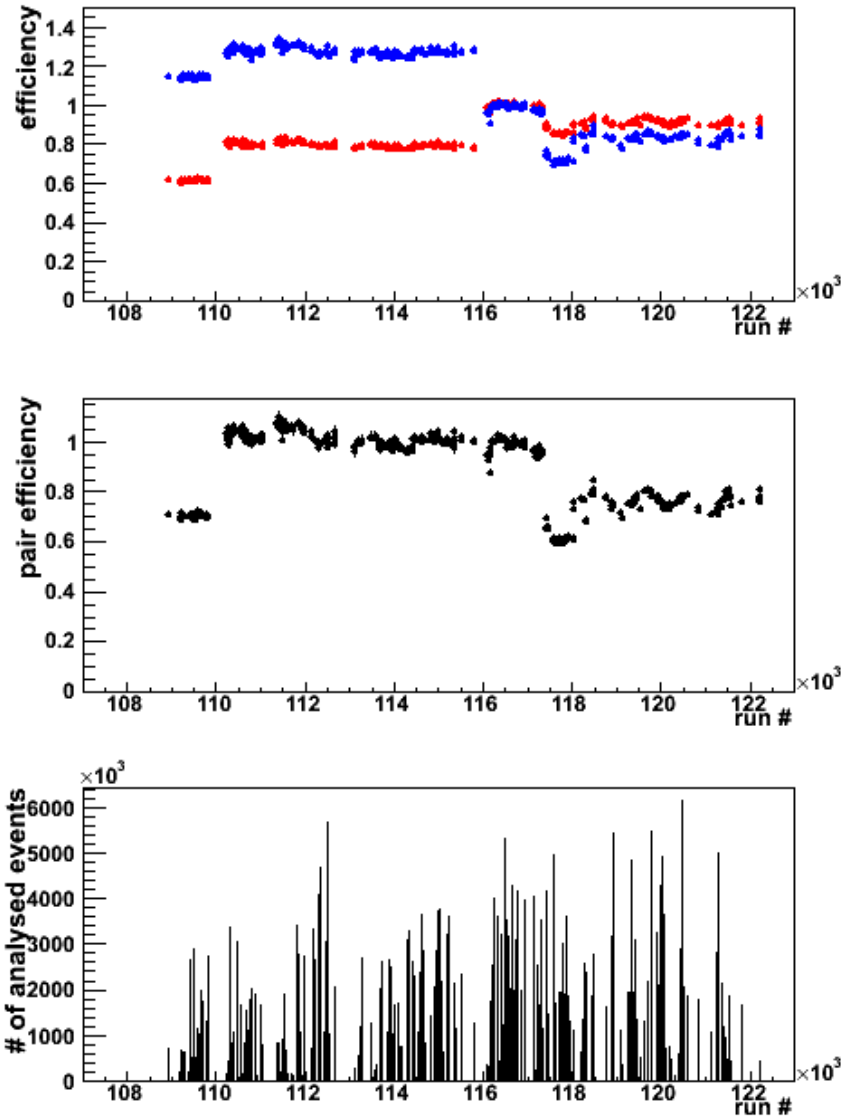

Figure 3.22: Top: run-by-run efficiency for K^+ (red) and K^- (blue). Middle: run-by-run efficiency for K^+K^- pair. Bottom: number of analyzed events for each run.

structed with and without embedding allows to determine the single particle embedding (track reconstruction) efficiency. The embedding efficiency for the ϕ was calculated as the product of single kaon efficiencies $\varepsilon^{\phi}_{emb} = \varepsilon^{K^+}_{emb} \times \varepsilon^{K^-}_{emb}$. The ϕ meson embedding efficiencies as a function of event centrality for Run-4 "two kaons PID" (blue) and "no PID" (red) analyses are shown in Fig. 3.23.

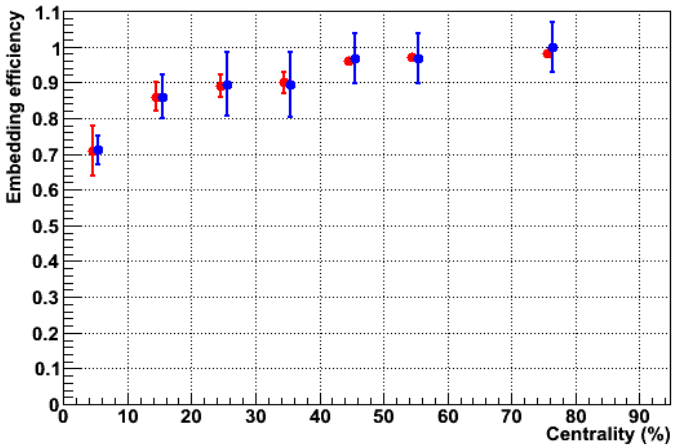

Figure 3.23: Embedding (track reconstruction) efficiencies for $\phi \rightarrow K^+K^-$ in Run-4 "two kaons PID" analysis (blue) and in Run-4 "no PID" analysis (red). The points are slightly displaced for clarity.

3.10 Bin width correction

Data which is distributed along steeply falling curves, such as particle yields as a function of p_T, when binned in p_T, shall be corrected for the effects of finite bin width. The effect is more significant in wide bins such that the average p_T of the data in that bin is shifted with respect to the center of the bin. To correct for this effect one can either move the data points vertically and leave the p_T unchanged at the center of the bin or move the data points along the p_T-axis and leave the yield unchanged. In this work we use the first method as it allows to control positioning of the data points on the p_T-axis, which is important when calculating the ratio of two spectra.

Let $f(p_T)$ denote the true ϕ meson invariant yield as function of p_T. The yield m measured in a bin ranging from p_T^{min} to p_T^{max} is given by:

$$m = \frac{1}{p_T^{max} - p_T^{min}} \cdot \int_{p_T^{min}}^{p_T^{max}} f(p_T) dp_T \tag{3.11}$$

A fit to the uncorrected spectrum is used as an approximation of the $f(p_T)$. The correction factor for each data point is defined as the ratio of m to the value of the fit at the center of the corresponding bin.

3.11 Systematic uncertainties

The following sources of systematic uncertainties affecting the extraction of the raw ϕ meson yields and calculation of the reconstruction efficiencies have been considered:

Uncertainty in fiducial acceptance determination

Studies of the fiducial acceptance mismatch between the data and simulation are detailed in Section 3.6.2. The systematic uncertainties on the fiducial acceptance of the DC/PC1 were evaluated from the variation of the ratio of the integrals, data to simulation (see Fig. 3.18), resulting from the selection of different regions for the normalization of data and simulation, and was found to be 2% for a single charged track and 4% for a pair.

The systematic uncertainties on the fiducial acceptance of the TOF were evaluated in a similar way. The projection of a track on the TOF subsystem already has the DC/PC uncertainty in it because of the evident imprinting of the DC/PC dead areas seen in Fig. 3.19 and Fig. 3.20. The simulation was normalized to data in different regions, shown as black rectangulars in Fig. 3.19. From the variation of the ratio of the total integrals, data to simulation, we estimated the TOF acceptance uncertainty for identified tracks to be 4.5%. The total systematic uncertainty related to the DC/PC1/TOF acceptance is 6.5% for a pair. In Run-4 Au+Au "two kaons PID" analysis this uncertainty is somewhat smaller, 4.5% for a pair. This can be due to the better tuning of the TOF detector simulation to the real data for Run-4 Au+Au data set.

Run-by-run variation of acceptance

In the Run-4 Au+Au "two kaons PID" analysis the run-by-run correction was done by two methods: by monitoring the average number of inclusive kaons per event, and by monitoring the K^+ and K^- from the ϕ meson peak region. The maximum deviation of 6% between the two methods was assigned as the systematic error.

In all other analyses, after the severe data quality studies described in Section 3.2, the variation of the acceptance with time were as low as $\sim$2-3% for a pair.

Raw yield extraction in data and simulation

In all analyses but the Run-4 Au+Au "two kaons PID" analysis[1] to study the systematic uncertainty in the raw yield extraction we: (i) vary the fit function to describe the combinatorial background by using a second vs. third order polynomial function, (ii) vary the range of the fits used to determine the shape of the background under the ϕ peak, (iii) repeat the analysis with additional track selection criterion (4σ matching in ϕ and z to the PC3||EMCal) resulting in a change of the shape of the background under the ϕ peak.

[1] All analyses where the fitting technique was used for the combinatorial background determination.

In the Run-4 Au+Au "two kaons PID" analysis the mixing technique (see Section 3.4.1) was used for the combinatorial background determination. From the comparison of the normalization factors from the different normalization methods we derive a maximum uncertainty of $\pm 1\%$ in the normalization factor. This translates into an uncertainty in the raw yield determination of $\pm \frac{1}{\sqrt{12}}(S/B)^{-1}$, where S/B is the signal to background ratio. Additionally, we vary the mass window over which the meson yield is determined.

Embedding uncertainty

The systematic error due to the embedding procedure was estimated as a function of centrality by calculating the embedding correction with different track selection criteria and varies from 1% to 7% from peripheral to central collisions.

Momentum scale uncertainty

To estimate the systematic error related to uncertainty of the DC/PC1 momentum scale we varied the momenta of the reconstructed particles within 0.5% in the simulated data and calculated the corresponding variation of reconstruction efficiency. The estimated uncertainty increases gradually with p_T from 0.5% at 1 GeV/c to 5% at 7 GeV/c.

Branching ratio uncertainty

Branching ratio uncertainty for $\phi \rightarrow K^+K^-$decay is equal to 1.2% [117].

The total systematic error is determined by the quadratic sum of the individual contributions. A summary of all systematic uncertainties for the p+p, d+Au and Au+Au analyses is given in Appendix A.

Chapter 4

Results and discussion

4.1 Invariant transverse momentum spectra.

The fully corrected invariant p_T spectra (see Section 3.5) of the ϕ meson measured in p+p, d+Au and Au+Au collisions are shown in Fig. 4.1. The p_T spectra are derived in p+p and d+Au for minimum bias events, and in Au+Au for minimum bias events and seven centrality classes (0-10%, 10-20%, 20-30%, 30-40%, 40-50%, 50-60% and 60-93%). At low p_T up to values of $\sim 4-4.5$ GeV/c the spectra appear to follow an exponential shape for all collision systems and all centralities, while at higher p_T they begin to exhibit the power-law behavior expected for particles produced in hard scattering processes. Measurements done with different analysis techniques are shown together in Fig. 4.1 with different symbols. Reasonable agreement between the different analysis techniques is seen in the regions where the measurements overlap. This is better demonstrated on a linear scale in Fig. 4.2 which shows the ratios of the invariant yields obtained with "no PID" or "one kaon PID" techniques in p+p collisions to a fit performed to the combined data sets and similar ratios for the results obtained with "no PID" or "two kaons PID" techniques in Au+Au collisions.

To avoid an additional error in the nuclear modification factors due to interpolation of data points, the p+p analyses have been revisited to have the same p_T binning as in the d+Au and Au+Au analyses. The final p_T binning for d+Au and Au+Au and for the corresponding p+p reference spectra is presented below, all values are in units of GeV/c. The spectra in the final p_T binning are referred hereinafter as final.

- Au+Au / p+p reference: 1.1 ± 0.1, 1.45 ± 0.25, 1.95 ± 0.25, 2.45 ± 0.25, 2.95 ± 0.25, 3.45 ± 0.25, 3.95 ± 0.25, 4.45 ± 0.25, 5.5 ± 0.5, 7.0 ± 1.0
- d+Au Min. bias / p+p reference: 1.45 ± 0.25, 1.95 ± 0.25, 2.45 ± 0.25, 2.95 ± 0.25, 3.45 ± 0.25, 3.95 ± 0.25, 4.45 ± 0.25, 5.1 ± 0.4

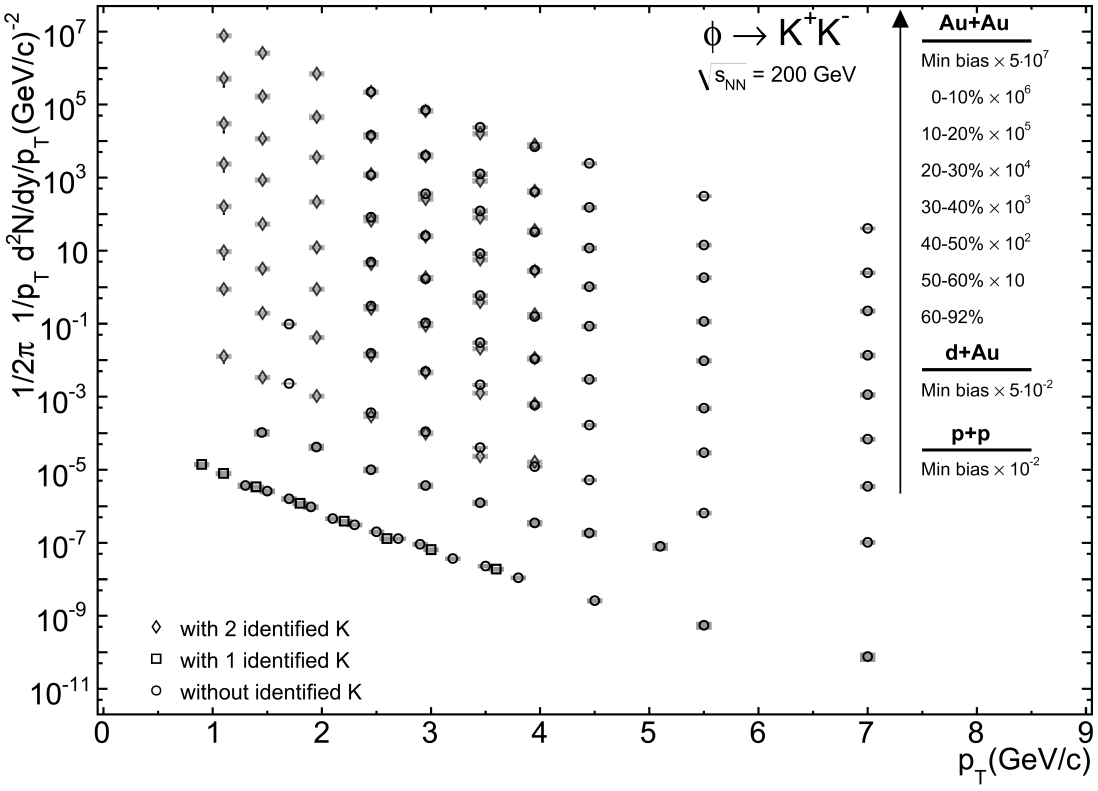

Figure 4.1: ϕ meson invariant p_T spectra. The error bars show the statistical errors, and the gray error bands show the systematic errors on the data points. Both statistical and systematic errors are in almost all cases smaller than the size of the symbols.

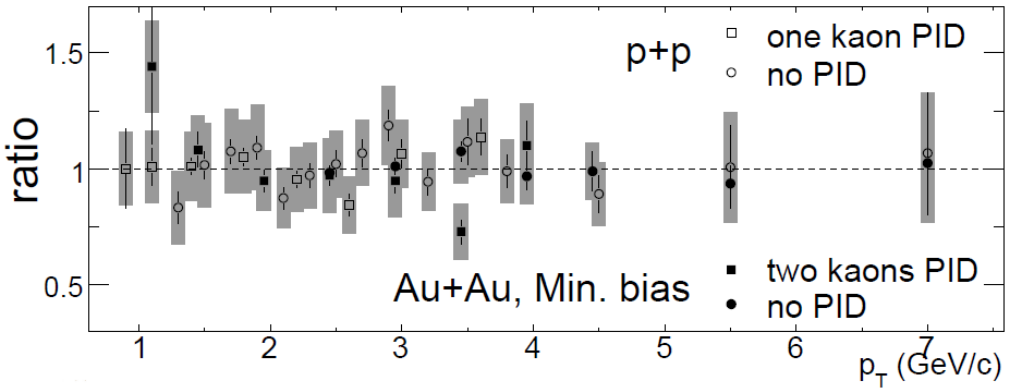

Figure 4.2: Ratios of the invariant yields obtained with "no PID" or "one kaon PID" ("no PID" or "two kaons PID") techniques in p+p (Au+Au) to a fit performed to the combined data sets.

The final Au+Au spectra were obtained by taking the first three low p_T points from the"two kaons PID" analysis, and all other points from the "no PID" analysis. In the final p+p spectra only the lowest p_T point was taken from the "one kaon PID" analysis, and the rest from the "no PID" analysis. Fig. 4.3 shows the final ϕ meson spectra obtained in

p+p, d+Au and Au+Au.

4.2 Rapidity density

The yields of strange particles are interesting and useful probes for examining the hot and dense nuclear matter as they help in understanding the strangeness production in heavy-ion collisions and the equilibration of strangeness (see Section 1.3.1 and Section 1.4). Moreover, the restoration of approximate chiral symmetry at high temperature and density is expected to modify the ϕ meson mass and width. The latter may result in a change of the branching ratios of $\phi \rightarrow K^+K^-$ and $\phi \rightarrow e^+e^-$ (see Section 1.4) when the ϕ decays in the medium, which can be detected by comparing the yields of the ϕ measured via K^+K^- and e^+e^- decay channels (see Section 1.3.2 and Section 1.4).

The best and most accurate way to measure the particle rapidity density is to sum up the $\frac{d^2N}{dp_Tdy}$ ($\frac{d^2N}{dm_Tdy}$) data points over the entire p_T (or m_T) range. Unfortunately this cannot be done when the detector acceptance is limited for low-p_T particles, which is a very common situation in many experiments, and also in PHENIX. In such cases the usual practice is to fit the measured spectra with some functional form and calculate $\frac{dN}{dy}$ by integrating the fit function over the full p_T or m_T range. Since the true functional form is unknown a certain assumption regarding the functional form is required and hence, the resulting $\frac{dN}{dy}$ is model-dependent. The choice of the model becomes of primary importance when the contribution to $\frac{dN}{dy}$ from the extrapolation is significant as is the case for the $\phi \rightarrow K^+K^-$ measurements. In this work the ϕ meson rapidity density is obtained by fitting the fully corrected invariant p_T distribution of the ϕ mesons with a Levy [49, 118] function adopted to the form:

$$\frac{1}{2\pi p_T}\frac{d^2N}{dp_Tdy} = \frac{1}{2\pi}\frac{dN}{dy}\frac{(n-1)(n-2)}{(\Lambda+m_\phi(n-1))(\Lambda+m_\phi)}\left(\frac{\Lambda+\sqrt{p_T^2+m_\phi^2}}{\Lambda+m_\phi}\right)^{-n} \tag{4.1}$$

where $\frac{dN}{dy}$, n and Λ are free parameters, and m_ϕ is the mass of the ϕ meson. The motivation behind the choice of the Levy function to fit the data is simple: it has the an exponential-like shape at low p_T and at the same time it has a power-law-like shape at high p_T. The choice of this function will be further justified below. We also used two different exponential functions to fit the data which are commonly used:

$$\frac{1}{2\pi p_T}\frac{d^2N}{dp_Tdy} = \frac{1}{2\pi}\frac{dN}{dy}\frac{1}{T^2}e^{-p_T/T} \tag{4.2a}$$

$$\frac{1}{2\pi p_T}\frac{d^2N}{dp_Tdy} = \frac{1}{2\pi}\frac{dN}{dy}\frac{1}{T(T+m_\phi)}e^{-(m_T-m_\phi)/T} \tag{4.2b}$$

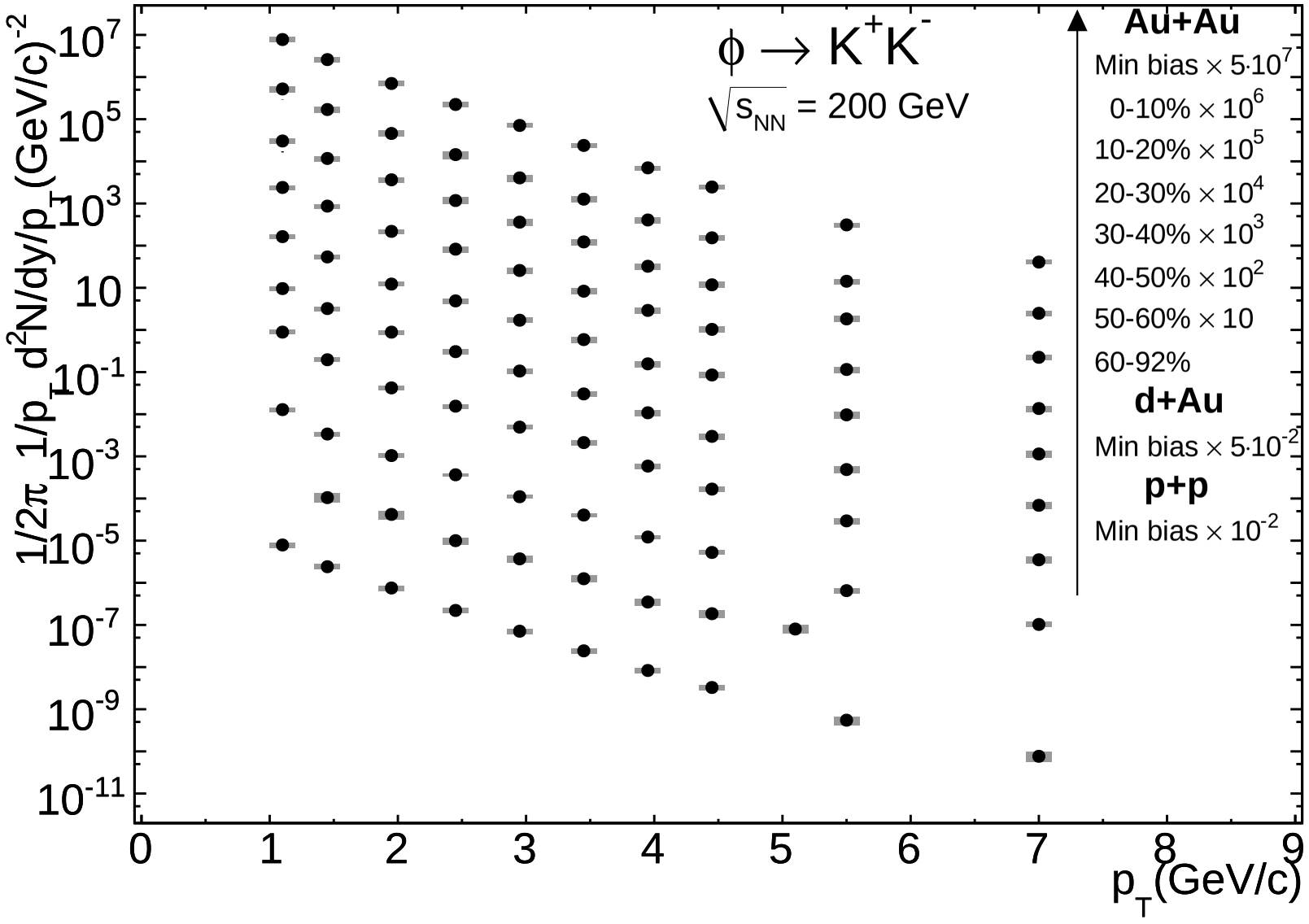

Figure 4.3: ϕ meson invariant p_T spectra in p+p, d+Au and Au+Au in the final p_T bins. The error bars show the statistical errors, and the gray error bands show the systematic errors on the data points. Both statistical and systematic errors are in almost all cases smaller than the size of the symbols.

The first function implies that the particle production is exponential in p_T, while the second one assumes that the particle production is exponential in $m_T = \sqrt{p_T^2 + m_\phi^2}$. $\frac{dN}{dy}$ and T are free parameters in both functions.

We start by fitting the ϕ meson p_T spectra obtained in p+p and minimum bias Au+Au collisions with the three functions over the entire range of the measurements. As one sees in Fig. 4.4 the spectral shapes can be well described with Levy functional fits, while the exponential fits underestimate the ϕ meson yields at $p_T \gtrsim 4$ GeV/c. Since at high p_T the data do not follow none of the exponential distributions, in further analysis we limit the p_T range for the exponential fits to $p_T = 0.9 - 4.3$ GeV/c ($m_T = 1.36 - 4.42$ GeV/c^2). The Levy fits are always performed over the entire p_T range $0.9 - 7.2$ GeV/c. A summary of the ϕ meson p_T spectra fitted under these conditions is presented in Fig. 4.5. The parameters extracted from the fits and χ^2/NDF values are given in Table 4.1, Table 4.2 and Table 4.3.

The extrapolation of the measured spectra to $p_T = 0$ GeV/c leads to a significant systematic uncertainty in the $\frac{dN}{dy}$ determination. To estimate this error the p_T spectra are fitted multiple times. Each time the y-coordinates of all points in the spectra are varied by a fraction of the standard deviation. To completely randomize the variation of the points within the measured errors we used the following harmonic function:

$$v^i(p_T^i) = v_0^i + a_{random}\sigma^i \cos\left(2\pi\left(\frac{f_{random}}{f_{max}} + f_{min}\right)\frac{p_T^i - p_{Tmin}}{p_{Tmax} - p_{Tmin}} + \varphi_{random}\right) \tag{4.3}$$

where the new value v^i in the bin p_T^i is the measured value v_0^i in this bin increased by a random fraction a_{random} of the systematic error in this bin, σ^i, multiplied by a cosine function with a random phase φ_{random} and a random frequency f_{random}. a_{random} is distributed according to a Gaussian law with zero mean and variance equal to one, φ_{random} and f_{random} have a flat probability distribution function chosen within the limits [φ_{min},φ_{max}]=[-π,π] and [f_{min},f_{max}]=[0,0.5], respectively.

As a result of the multiple fits we obtain some distributions for each fit parameter. Examples of fit trials for the three fit functions and the resulting parameter distributions are shown in Appendix B. The RMS of each parameter distribution is assigned as systematic error on this parameter. The number of fit trials is set to 1000, as the mean and RMS values of the parameter distributions do not change significantly with a larger number of trials. The systematic errors on the fit parameters obtained using this procedure for the three fitting functions are quoted in Table 4.1, Table 4.2 and Table 4.3.

Although in some cases the χ^2/NDF values for the fits are not great, it can be seen from Fig. 4.5 that the Levy and p_T-exponential functions (see Eq. 4.1 and Eq. 4.2a) fit

Event class	dN/dy	Λ (GeV/c^2)	n	χ^2/NDF
Au+Au Min. bias	1.55±0.12(stat)±0.21(syst)	4.01±0.53(stat)±1.10(syst)	17.44±1.23(stat)±2.65(syst)	27.9/7
Au+Au 0-10%	5.47±0.93(stat)±0.76(syst)	3.90±1.32(stat)±1.20(syst)	17.76±3.23(stat)±3.30(syst)	8.7/7
Au+Au 10-20%	3.75±0.47(stat)±0.45(syst)	4.09±1.03(stat)±1.15(syst)	17.44±4.00(stat)±3.08(syst)	9.9/7
Au+Au 20-30%	2.14±0.27(stat)±0.27(syst)	6.46±2.01(stat)±1.50(syst)	22.83±4.61(stat)±3.74(syst)	8.6/7
Au+Au 30-40%	1.26±0.17(stat)±0.18(syst)	5.10±1.44(stat)±1.37(syst)	18.93±3.11(stat)±3.34(syst)	17.5/7
Au+Au 40-50%	0.90±0.12(stat)±0.10(syst)	5.03±1.52(stat)±1.47(syst)	19.52±3.52(stat)±3.87(syst)	14.1/7
Au+Au 50-60%	0.45±0.07(stat)±0.07(syst)	4.83±1.63(stat)±1.33(syst)	18.69±3.62(stat)±0.64(syst)	22.9/7
Au+Au 60-92%	0.106±0.014(stat)±0.011(syst)	3.87±1.14(stat)±0.85(syst)	16.36±2.59(stat)±1.92(syst)	9.3/7
p+p Min. bias	0.0082±0.0005(stat)±0.0010(syst)	2.45±0.46(stat)±0.66(syst)	13.08±1.15(stat)±1.64(syst)	12.3/7

Table 4.1: Parameters from the Levy fits with Eq. 4.1 to the ϕ meson spectra presented in Fig. 4.5.

Event class	dN/dy	T (GeV)	χ^2/NDF
Au+Au Min. bias	1.55±0.08(stat)±0.21(syst)	0.432±0.005(stat)±0.010(syst)	7.4/5
Au+Au 0-10%	5.80±0.71(stat)±0.90(syst)	0.412±0.012(stat)±0.011(syst)	1.2/5
Au+Au 10-20%	3.99±0.36(stat)±0.50(syst)	0.431±0.009(stat)±0.010(syst)	1.6/5
Au+Au 20-30%	2.44±0.22(stat)±0.31(syst)	0.446±0.009(stat)±0.012(syst)	4.4/5
Au+Au 30-40%	1.40±0.13(stat)±0.17(syst)	0.454±0.010(stat)±0.011(syst)	10.0/5
Au+Au 40-50%	0.95±0.09(stat)±0.012(syst)	0.444±0.009(stat)±0.011(syst)	3.7/5
Au+Au 50-60%	0.43±0.04(stat)±0.05(syst)	0.462±0.011(stat)±0.012(syst)	17.9/5
Au+Au 60-92%	0.108±0.009(stat)±0.011(syst)	0.447±0.009(stat)±0.009(syst)	3.9/5
p+p Min. bias	0.0082±0.0003(stat)±0.0011(syst)	0.429±0.005(stat)±0.011(syst)	24.1/5

Table 4.2: Parameters from the exponential fits with Eq. 4.2a to the ϕ meson spectra presented in Fig. 4.5.

Event class	dN/dy	T (GeV)	χ^2/NDF
Au+Au Min. bias	0.95±0.04(stat)±0.12(syst)	0.404±0.005(stat)±0.010(syst)	18.3/5
Au+Au 0-10%	3.56±0.38(stat)±0.52(syst)	0.381±0.011(stat)±0.012(syst)	3.1/5
Au+Au 10-20%	2.52±0.20(stat)±0.29(syst)	0.400±0.009(stat)±0.010(syst)	2.3/5
Au+Au 20-30%	1.55±0.12(stat)±0.18(syst)	0.416±0.009(stat)±0.012(syst)	7.2/5
Au+Au 30-40%	0.89±0.07(stat)±0.10(syst)	0.426±0.010(stat)±0.011(syst)	11.4/5
Au+Au 40-50%	0.60±0.05(stat)±0.07(syst)	0.415±0.009(stat)±0.011(syst)	5.7/5
Au+Au 50-60%	0.27±0.02(stat)±0.03(syst)	0.435±0.011(stat)±0.012(syst)	22.6/5
Au+Au 60-92%	0.068±0.005(stat)±0.007(syst)	0.418±0.009(stat)±0.008(syst)	5.9/5
p+p Min. bias	0.0054±0.0002(stat)±0.0006(syst)	0.394±0.005(stat)±0.011(syst)	51.6/5

Table 4.3: Parameters from the exponential fits with Eq. 4.2b to the ϕ meson spectra presented in Fig. 4.5.

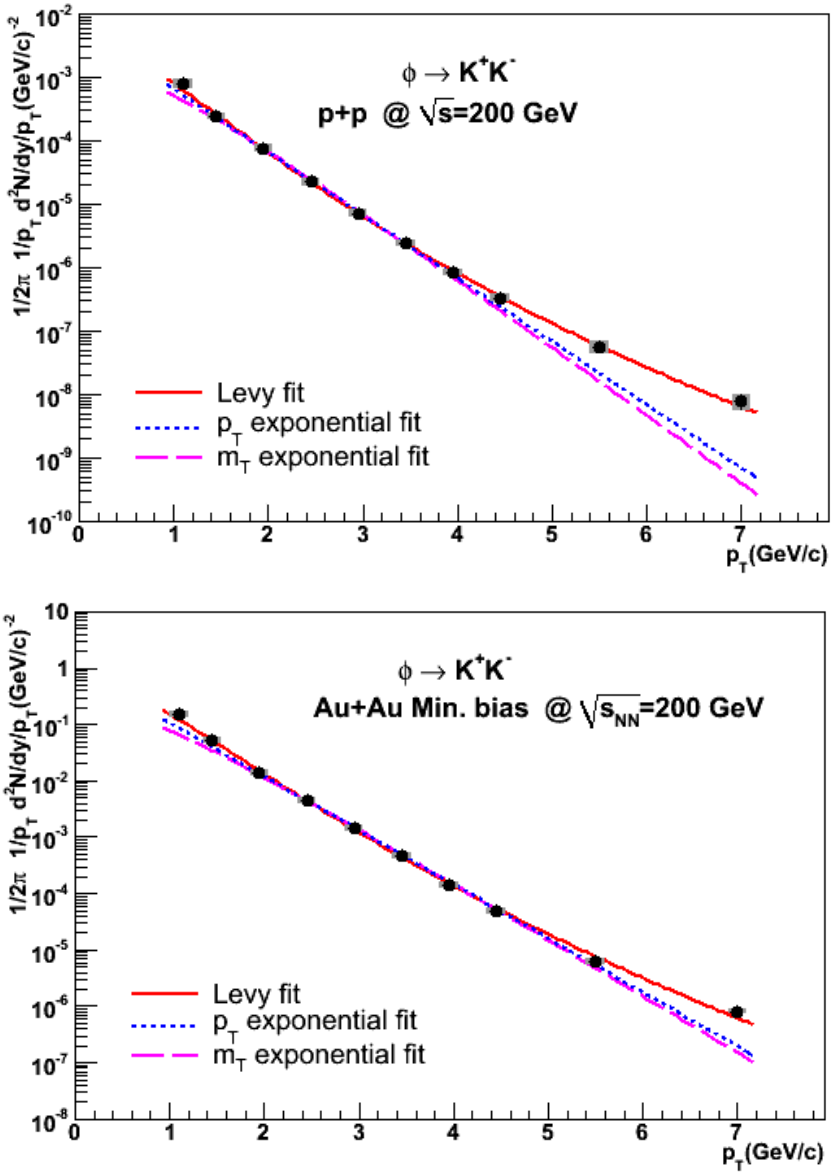

Figure 4.4: Invariant p_T spectra of $\phi \rightarrow K^+K^-$ in p+p and minimum bias Au+Au collisions fitted with the Levy function of Eq. 4.1, the p_T-exponential function of Eq. 4.2a and the m_T-exponential function of Eq. 4.2b.

the data reasonably well. The ϕ meson rapidity densities obtained by fitting with these two functions are in a good agreement. Fits performed with the m_T-exponential function (see Eq. 4.2b) miss the lowest-p_T point, consequently the resulting $\frac{dN}{dy}$ is systematically lower by a factor of $\sim$1.5-1.6 compared to the $\frac{dN}{dy}$ obtained by fitting with the other two functions.

However, our data by themselves do not provide enough information to discard the results obtained with any of the three functions. To further constrain the models we use the complementary $\phi \rightarrow e^+e^-$ data obtained in p+p collisions [119] which cover the low

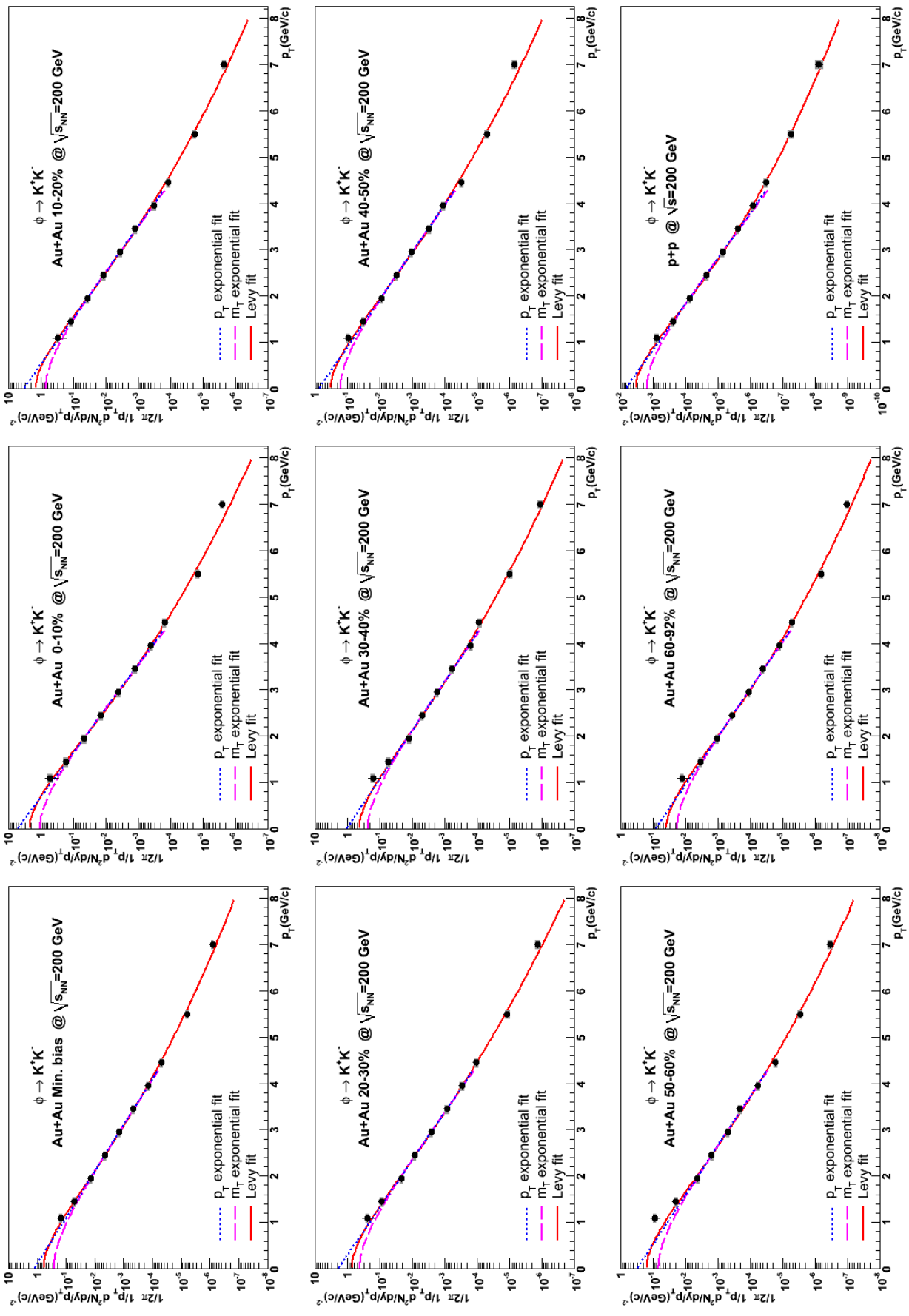

Figure 4.5: Invariant p_T spectra of $\phi \rightarrow K^+K^-$ in p+p and Au+Au collisions fitted with the Levy function of Eq. 4.1, the p_T-exponential function of Eq. 4.2a and the m_T-exponential function of Eq. 4.2b.

p_T region of the ϕ meson spectra unavailable in any of the K^+K^- analyses.

The p_T spectra of $\phi \rightarrow e^+e^-$ in p+p and $\phi \rightarrow K^+K^-$ in p+p and minimum bias Au+Au are shown in Fig. 4.6 plotted in the form of $\frac{d^2N}{dp_T dy} vs. p_T$. Since $\frac{d^2N}{dp_T dy}$ is equal to zero at $p_T = 0$ one sees that the e^+e^- data allow to extract $\frac{dN}{dy}$ by summing up the data points in the $\frac{dN^2}{dy dp_T}$ spectra without invoking any model and with almost no error in the extrapolation to $p_T = 0$. We also note that the $\phi \rightarrow e^+e^-$ and $\phi \rightarrow K^+K^-$ measurements in p+p collisions have a significant overlap region in p_T and in that region both measurements agree well as demonstrated in Fig. 4.6 and Fig. 4.7.

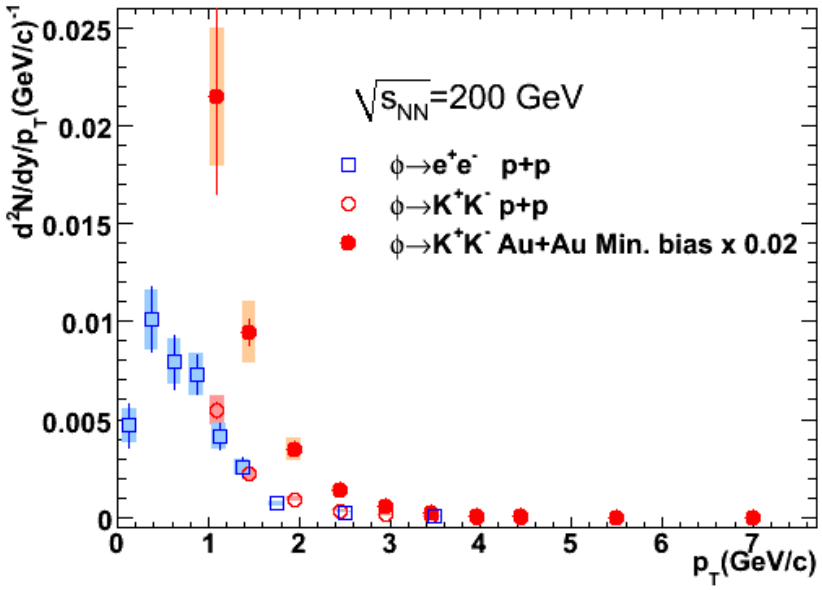

Figure 4.6: p_T spectra of the ϕ meson measured in p+p and in minimum bias Au+Au collisions.

In Fig. 4.7 the combined data points from both measurements are fitted with the Levy, m_T-exponential and p_T-exponential functions. The m_T-exponential fits are shown by the dashed red and blue lines in the top panel. The red line is the fit performed over the m_T range $1-4.4$ GeV/c^2 (p_T range $0-4.3$ GeV/c), the blue line is the fit over the m_T range $1-1.9$ GeV/c^2 (p_T range $0-1.6$ GeV/c). The fits with the p_T-exponential and Levy function extend from 0 to 4.3 GeV/c and from 0 to 7.2 GeV/c (entire range of the measurements), respectively, and are shown in the bottom panel. Table 4.4 summarizes the $\frac{dN}{dy}$ values extracted using the various fits described above, as well as those obtained by summing up the e^+e^- data points. For comparison the table also includes the fit results of the K^+K^- data only from Table 4.1, Table 4.2 and Table 4.3.

All methods used to extract the ϕ meson rapidity density in p+p collisions yield consistent results with only exception - the m_T-exponential fits performed over the p_T range $0-4.3$ GeV/c. From Fig. 4.7 as well as the $\frac{dN}{dy}$ values presented in Table 4.4, it can be

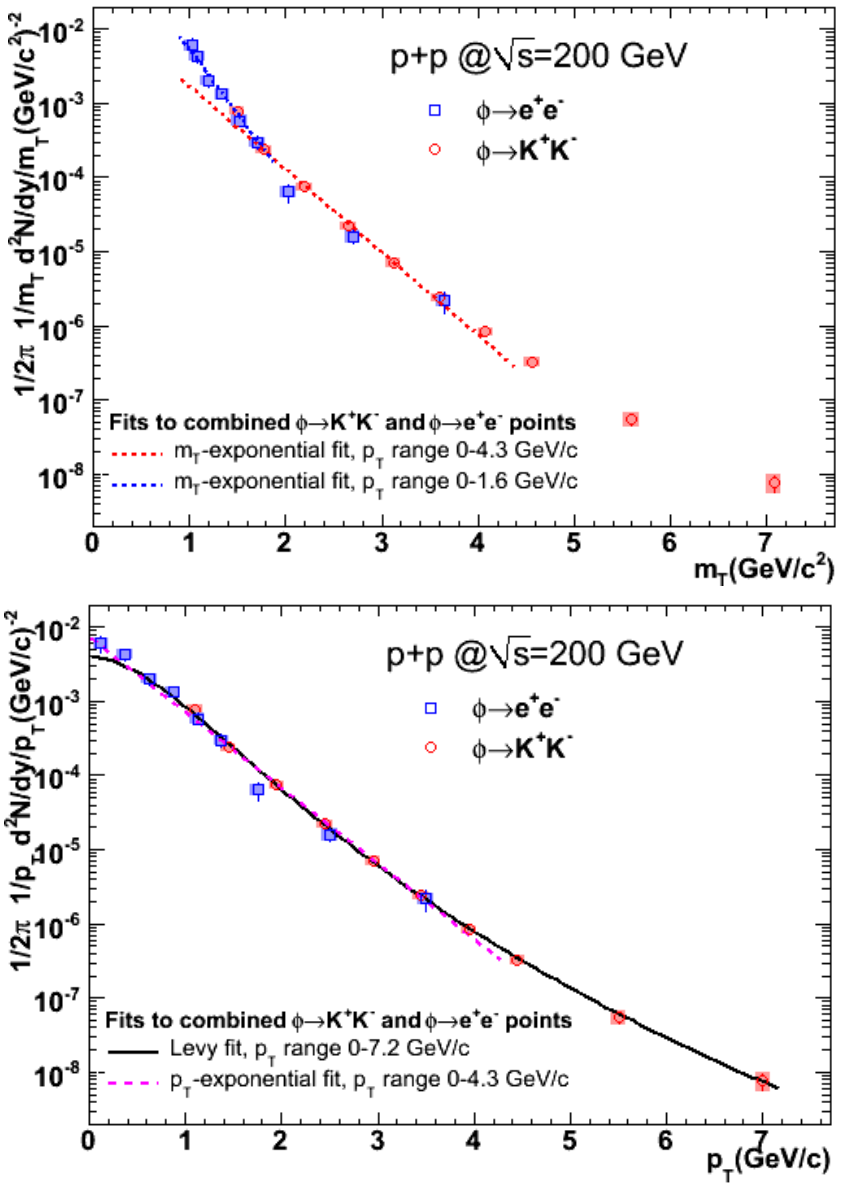

Figure 4.7: Invariant m_T (top) and p_T (bottom) spectra of the ϕ meson measured through $\phi \to K^+K^-$ and $\phi \to e^+e^-$ channels in p+p collisions. The solid line represents the Levy function fit while the dashed lines are the m_T-exponential or p_T-exponential function fits. All fits are performed to the combined $\phi \to K^+K^-$ and $\phi \to e^+e^-$ data points (see text for details).

seen that the m_T-exponential function fit is sensitive to the fitting range. The ϕ meson m_T distribution has a clear change in slope at $m_T \approx 1.8$ GeV/c which cannot be described by the fit if higher m_T points are included in the fit. Thus, despite the fact that the m_T-exponential function is commonly used to describe particle p_T spectra, it cannot be used to describe our $\phi \to K^+K^-$ data as we have only two p_T bins below $m_T \approx 1.8$ GeV/c.

Based on the above discussion we take the Levy fit results on $\frac{dN}{dy}$ as the basic case

Data sample	Method	dN/dy
e^+e^- & K^+K^-	Levy fit ($0-7.2$ GeV/c)	0.0089±0.0005(stat)
e^+e^- & K^+K^-	p_T-exponential fit ($0-4.3$ GeV/c)	0.0084±0.0003(stat)
e^+e^- & K^+K^-	m_T-exponential fit ($0-1.6$ GeV/c)	0.0099±0.0006(stat)
e^+e^- & K^+K^-	m_T-exponential fit ($0-4.3$ GeV/c)	0.0056±0.0002(stat)
e^+e^-	sum of the points in the spectra	0.0089±0.0016(stat)±0.0014(syst)
K^+K^-	Levy fit ($0-7.2$ GeV/c)	0.0082±0.0005(stat)±0.0010(syst)
K^+K^-	p_T-exponential fit ($0-4.3$ GeV/c)	0.0082±0.0003(stat)±0.0011(syst)
K^+K^-	m_T-exponential fit ($0-4.3$ GeV/c)	0.0054 ±0.0002(stat)±0.0006(syst)

Table 4.4: Summary of the ϕ meson $\frac{dN}{dy}$ values obtained by various methods in p+p collisions.

and we use the p_T-exponential function fit results as an alternative case for studying the systematics in the $\frac{dN}{dy}$ extraction.

The $\frac{dN}{dy}$ values obtained with the p_T-exponential fit depend also on the fitting range. We study this effect (see Table B.2 in Appendix B) and find the changes in the $\frac{dN}{dy}$ to be comparable with the systematic errors estimated previously. We also note that the $\frac{dN}{dy}$ values obtained with the p_T-exponential fit fall within the systematic error corridor defined by the "varying data points and refitting" procedure. Our conclusion is that the procedure we used to study the systematic uncertainties from the fitting of p_T spectra with the Levy function provides a reasonable estimate of these errors and there is no need to assign any additional systematic errors on the $\frac{dN}{dy}$ values. The final values of the ϕ meson yields per unit of rapidity with associated systematic errors are summarized in Table 4.5.

Event class	dN/dy
Au+Au Min. bias	1.55±0.12(stat)±0.21(syst)
Au+Au 0-10%	5.47±0.93(stat)±0.76(syst)
Au+Au 10-20%	3.75±0.47(stat)±0.45(syst)
Au+Au 20-30%	2.14±0.27(stat)±0.27(syst)
Au+Au 30-40%	1.26±0.17(stat)±0.18(syst)
Au+Au 40-50%	0.90±0.12(stat)±0.10(syst)
Au+Au 50-60%	0.45±0.07(stat)±0.07(syst)
Au+Au 60-92%	0.106±0.014(stat)±0.011(syst)
p+p Min. bias	0.0082±0.0005(stat)±0.0010(syst)

Table 4.5: Summary of the ϕ meson rapidity densities, $\frac{dN}{dy}$, obtained in Au+Au and p+p collisions. The systematic errors are estimated as described in the text.

4.2.1 Consistency with previous PHENIX results on ϕ production

We compare our Au+Au results with the previously published ϕ meson spectra [77] obtained from the lower statistics and smaller p_T reach Run-2 Au+Au dataset in Fig. 4.8. For this comparison our final spectra were combined to be at the same centrality bins as used in [77]. In order to check consistency between the new and old results we plot in a linear scale, both the new and the previously published spectra divided by the Levy fit performed to the new spectra. The resulting ratios are shown in the right panel of Fig. 4.8. Besides being consistent to the previous measurements, the new Au+Au spectra have a finer centrality binning and significantly higher p_T reach compared to the previous results.

The ϕ meson rapidity densities, $\frac{dN}{dy}$ from this work and those obtained in Ref. [77] are presented in Fig. 4.9. The left panel shows the system size dependence of $\frac{dN}{dy}$ and the right panel shows the same for $\frac{dN}{dy}$ normalized by the number of participant pairs ($0.5N_{part}$). The new results are consistent with the previously published results within statistical and systematic uncertainties. In the most central collisions the yield from Ref. [77] is lower by a factor of ∼1.4 (3.94±0.60(stat)±0.62(sys) vs. 5.47±0.93(stat)±0.76(sys)). We attribute this to the fact that in Ref. [77] the extraction of the ϕ meson yields was performed by fitting the spectra with the m_T-exponential function (see Eq. 4.2b) which may lead to an underestimation of the yield (see Section 4.2).

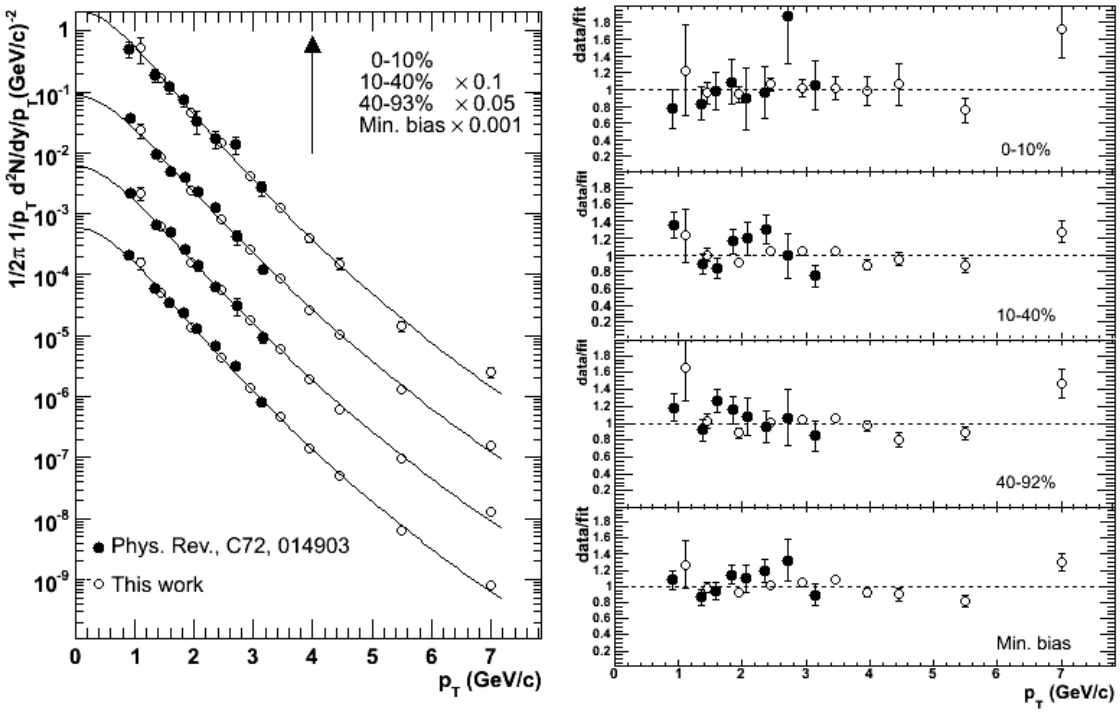

Figure 4.8: Consistency between the ϕ meson spectra in Au+Au collisions obtained in this work and previous PHENIX results [77].

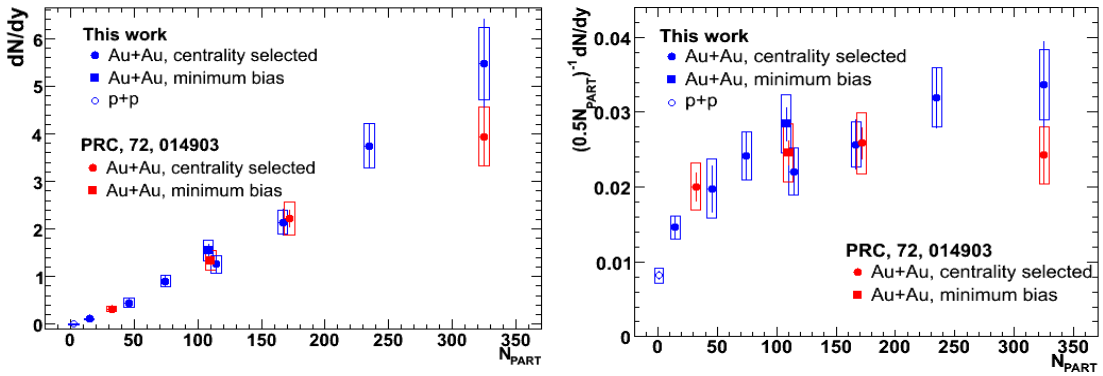

Figure 4.9: Consistency between the ϕ meson yields in Au+Au collisions obtained in this work and previous PHENIX results [77].

4.2.2 Comparison to $\phi \rightarrow e^+e^-$ results

As discussed in Section 1.4 the possible in-medium modification of the branching ratios of $\phi \rightarrow K^+K^-$ and $\phi \rightarrow e^+e^-$ is an important signal of the restoration of chiral symmetry. Fig. 4.10 shows the centrality dependence of the ϕ meson yield per unit of rapidity ($\frac{dN}{dy}$) per participant pair as obtained in the K^+K^- and e^+e^- decay channels. The preliminary e^+e^- measurements [79, 119] agree with the results from the K^+K^- channel in minimum bias and most central Au+Au collisions and also in p+p collisions, while in midcentral and peripheral Au+Au collisions the $\frac{dN}{dy}$ values extracted in the e^+e^- decay channel are by a factor of $\sim$2 larger than the yields extracted in the K^+K^- decay channel. However, statistical and systematic errors of the Au+Au dielectron channel measurements are too large preventing us from making any definite statements on possible in-medium effects. Within the error bars the yields measured in the two decay channels are consistent.

The precision of the present $\phi \rightarrow e^+e^-$ measurements in Au+Au is largely limited by a huge combinatorial background, and expected to be dramatically improved with the upgrade of the PHENIX experiment with the Hadron Blind Detector (see Chapter 5).

4.2.3 Comparison to results from other identified hadrons

Fig. 4.11 shows the system size dependence of the normalized yield for pions, kaons, protons from Ref. [120] and ϕ. The data show that $\frac{dN}{dy}$ per participant pair increases for all particle species. When we normalize the ϕ meson $\frac{dN}{dy}$ per participant in Au+Au by that measured in p+p, the data indicate a strong enhancement in the ϕ production over that expected from N_{part} scaling reaching a factor of about 4 in the most central Au+Au collisions (see Fig. 4.12). In fact, an enhanced production of ϕ meson in heavy-ion collisions is one of the signals of the QGP formation [73]. However, no clear conclusion can be drawn from this result before a similar comparison can be made of the relative

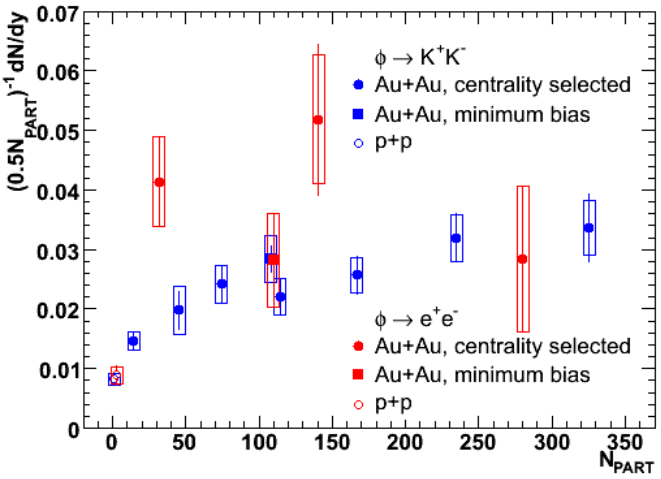

Figure 4.10: Multiplicity dependence of the ϕ meson rapidity density per participant pair for K^+K^- (blue) and e^+e^- (red) decay channels. Statistical and systematic errors are shown by vertical bars and boxes, respectively. For clarity, the K^+K^- and e^+e^- points for $p+p$ and minimum bias Au+Au collisions are shifted slightly along the abscissa.

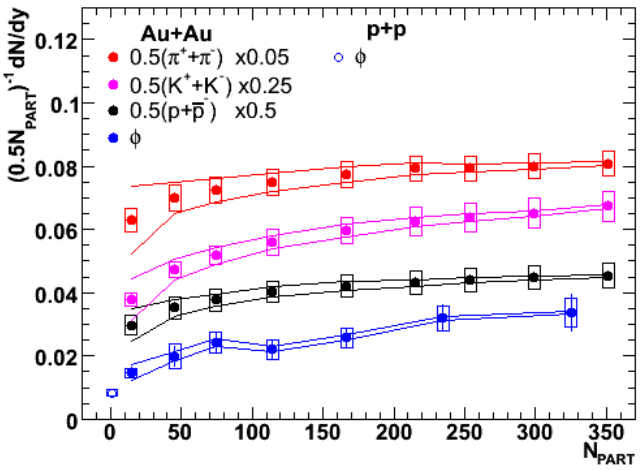

Figure 4.11: Rapidity density per participant pair ($0.5N_{part}$) as a function of N_{part} for pions, kaons, protons and ϕ mesons in Au+Au and p+p collisions at $\sqrt{s_{NN}} = 200$ GeV. Charged hadron data are taken from [120]. The lines represent the uncertainty on N_{part} affecting all particle species in the same way.

enhancements of other hadrons as we go from p+p to Au+Au. There is an ongoing work in PHENIX aiming at measuring the rapidity densities for pions, kaons, protons in p+p collisions. Lacking the p+p results for these hadrons, we plot the relative enhancement in the particle production in central collisions, with respect to the most peripheral collisions in Fig. 4.13. The error bars represent the total statistical and systematic errors

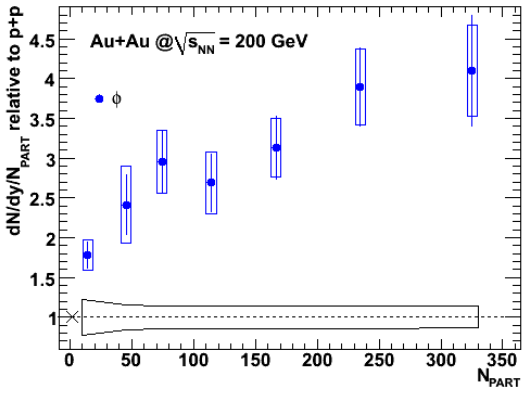

Figure 4.12: Relative enhancement of the ϕ meson production in Au+Au collisions with respect to p+p. The error band around unity reflects the uncertainty on N_{part} and the uncertainty in the p+p data combined.

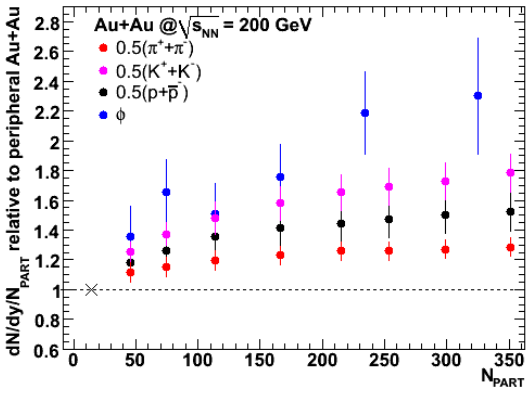

Figure 4.13: Relative enhancement in the production of pions, kaons, protons and ϕ in central Au+Au collisions with respect to the most peripheral.

combined[1]. The N_{part} value for the most peripheral collisions ($N_{part} = 14.5$) is indicated by the cross. All particles show an enhancement of $\frac{dN}{dy}$ per participant pair *vs*. centrality. But there seems to be an ordering of the relative enhancement magnitude in terms of strangeness content. A similar ordering has been previously seen in the production of multistrange baryons [24] (see Section 1.3.1). The relative enhancement for protons appears to be greater than for pions but smaller than for kaons. Hadron production data in p+p collisions will allow a better comparison with smaller error bars providing more precise answers about the enhancement of the ϕ meson production in the Au+Au collisions.

4.3 Nuclear modification factors

The R_{AA} for the ϕ meson was obtained by dividing point-by-point the Au+Au spectra, by the p+p spectra, scaled by the number of binary nucleon-nucleon collisions N_{coll}[2] (see Eq. 1.5). Accordingly, the R_{CP} was obtained by dividing point-by point the Au+Au spectra from central collisions, scaled by the corresponding N_{coll}, by the same from the most peripheral (60-93%) collisions (see Eq. 1.6). Statistical errors were propagated by the quadratic sum of the statistical errors of the numerator and denominator. When the systematic errors for R_{AA} and R_{CP} are calculated, the individual contributions should be subdivided into the two classes: correlated and uncorrelated errors. Since the correlated errors cancel in ratios, the total systematic errors were derived by the quadratic sum of

[1] These errors are probably overestimated, since the correlations between the systematic uncertainties on the $\frac{dN}{dy}$ measured in the most peripheral and central collisions were not accounted for.

[2] Same procedure is used to obtain the R_{dA} for the ϕ meson.

the uncorrelated systematic errors.

Fig. 4.14 and Fig. 4.15 show the ϕ-meson nuclear modification factors R_{AA} and R_{CP}, respectively, measured in Au+Au collisions at $\sqrt{s_{NN}} = 200$ GeV. Fig. 4.16 shows the ϕ meson R_{dA}, measured in minimum bias d+Au collisions at $\sqrt{s_{NN}} = 200$ GeV. The N_{coll} values for Au+Au collisions derived from Glauber calculations were taken from Table 2.2. For minimum bias d+Au collisions N_{coll} is equal to 8.5$\pm$0.4 [121]. In all plots, the boxes around 1 represent the systematic uncertainty from the N_{coll} determination. The systematic errors on each data point are dominated by contributions from the raw ϕ meson yield extraction and the reconstruction efficiency. There is also an overall normalization error of the p+p reference spectrum of 10% which is not shown on the plots.

Within errors, peripheral Au+Au collisions behave like a superposition of p+p collisions with regard to the ϕ meson production at $p_T > 1$ GeV/c ($R_{AA} \approx 1$). This results in the R_{CP} being very much similar to the R_{AA} (see Fig. 4.14 and Fig. 4.15) for the ϕ meson. For the purpose of the discussion we concentrate below on the R_{AA} only, keeping in mind that all features we see in the R_{AA} patterns can be also seen in the R_{CP}.

The R_{AA} for the 0-10% central collisions are noticeably below unity. It is ≈ 0.7 at $p_T = 1-2.5$ GeV/c and reaches ≈ 0.3 at $p_T > 5$ GeV/c. The transition from the suppression seen in central collisions to the N_{coll} scaling behavior apparent in the most peripheral collisions is rather smooth, also the R_{AA} patterns appear to flatten with increasing centrality.

The R_{dA} (shown in Fig. 4.16) is consistent with unity within the errors of the measurement. The large error bars leave some room for the Cronin enhancement [122–126]. The limited statistics prevent us from extending the study of the ϕ meson R_{dA} into more centrality bins.

4.3.1 R_{AA} comparison of ϕ meson to other identified particles

A clear difference between the suppression patterns of baryons and light mesons was observed in Au+Au collisions at intermediate p_T (see for example Fig. 1.10). Mesons are suppressed whereas baryons are not. This together with the common suppression pattern found at $p_T > 2.5$ GeV/c for η and π^0 [52], which have about a factor of 4 difference in their masses, suggests that the suppression is governed by the number of valence quarks rather than the mass of the hadron. Measurements of the nuclear modification factor for the ϕ meson, whose mass is similar to that of the baryons proton and $\Lambda(1115)$, have a discriminating power between mass and number of valence quarks effects and also allow to test whether the flavor of the constituent quarks are of any importance.

Fig. 4.17 shows a comparison of the R_{AA} for ϕ from this work, π^0 from Ref. [65],

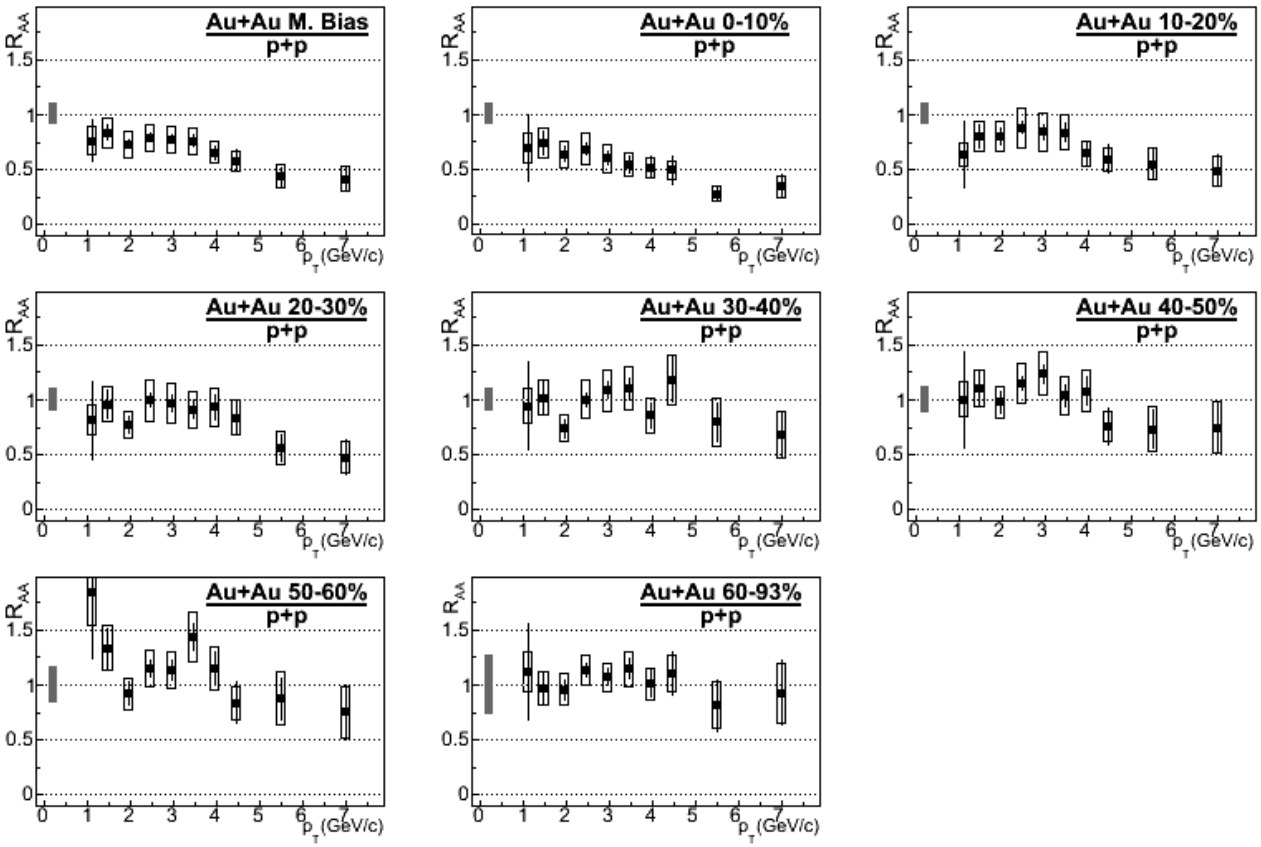

Figure 4.14: R_{AA} as a function of p_T for ϕ meson in Au+Au collisions at $\sqrt{s_{NN}} = 200$ GeV in minimum bias and seven centrality classes.

proton and kaon from Ref. [121] and η, ω and direct γ from Ref. [61] measured in most central Au+Au collisions. The ϕ's R_{AA} exhibits less suppression than π^0 and η in the p_{T} range of $1 < p_{\mathrm{T}} < 4.5$ GeV/c. At $p_{\mathrm{T}} > 5$ GeV/c the R_{AA} of ϕ becomes similar to that of π^0 and η [61, 65] although with large error bars. The R_{AA} for the kaon follows the trend of the ϕ in the p_{T} region where the measurements overlap. The measurements of ω meson are available only at high $p_T = 7-9$ GeV/c. It's suppression could be similar to that of π^0, η and ϕ, but a more conclusive statement is not possible due to the large errors of the measurements. The R_{AA} for the proton shows no suppression but on the contrary some enhancement at $p_{\mathrm{T}} > 1.5$ GeV/c. Initial state cold nuclear matter effects can also contribute to the differences in hadron suppression factors in A+A collisions.

Our results show that the ϕ meson does not follow the same suppression pattern as observed for other mesons in the intermediate p_T range. This could indicate that hadron suppression is governed not only by the number of valence quarks but also by their flavor.

The suppression of high p_T hadrons in heavy ion collisions relative to p+p is believed to be a consequence of parton energy loss in the medium generated in the collision [127]. Most theoretical models of parton energy loss utilize a factorized approach [128] where

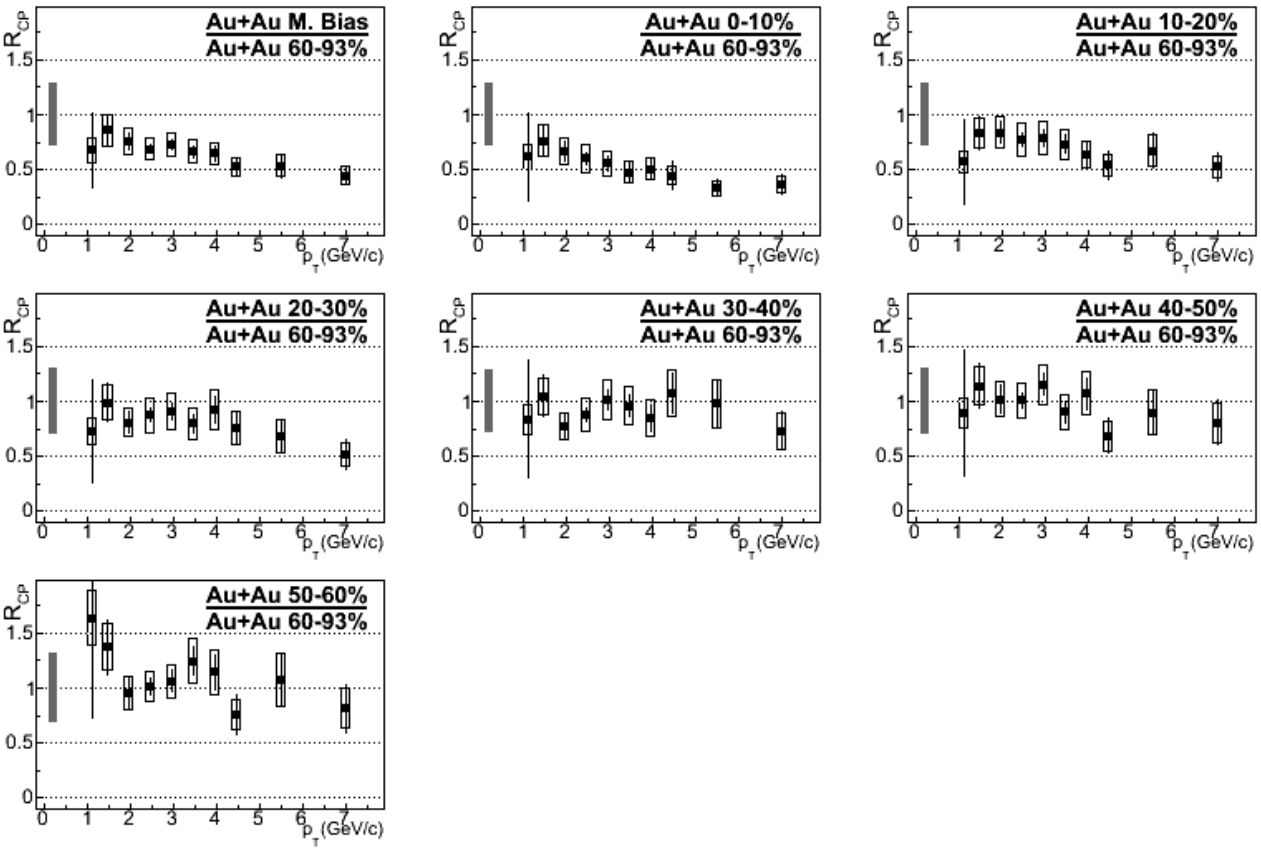

Figure 4.15: R_{CP} as a function of p_T for ϕ meson in Au+Au collisions at $\sqrt{s_{NN}} = 200$ GeV in minimum bias and six centrality classes.

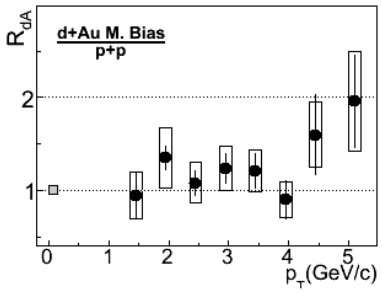

Figure 4.16: R_{dA} as a function of p_T for ϕ meson in minimum bias d+Au collisions at $\sqrt{s_{NN}} = 200$ GeV.

the production cross section of a high-p_T hadron h may be expressed as the product:

$$d\sigma^{hard}_{AB\to h} = f_{a/A}(x_a, Q^2_a) \otimes f_{b/B}(x_b, Q^2_b) \otimes d\sigma^{hard}_{ab\to cX}(x_a, x_b, Q^2_c) \otimes \widetilde{\mathcal{D}}_{c\to h}(z_c, Q^2_c) \qquad (4.4)$$

where $d\sigma^{hard}_{ab\to cX}(x_a, x_b, Q^2_c)$ is the perturbative partonic cross section, $x_a = p_a/P_A$ and $x_b = p_b/P_A$ are the initial momentum fractions carried by the interacting partons, $z_c = p_h/p_c$ is the momentum fraction carried by the final observable hadron, $f_{a/A}(x_a, Q^2_a)$ and

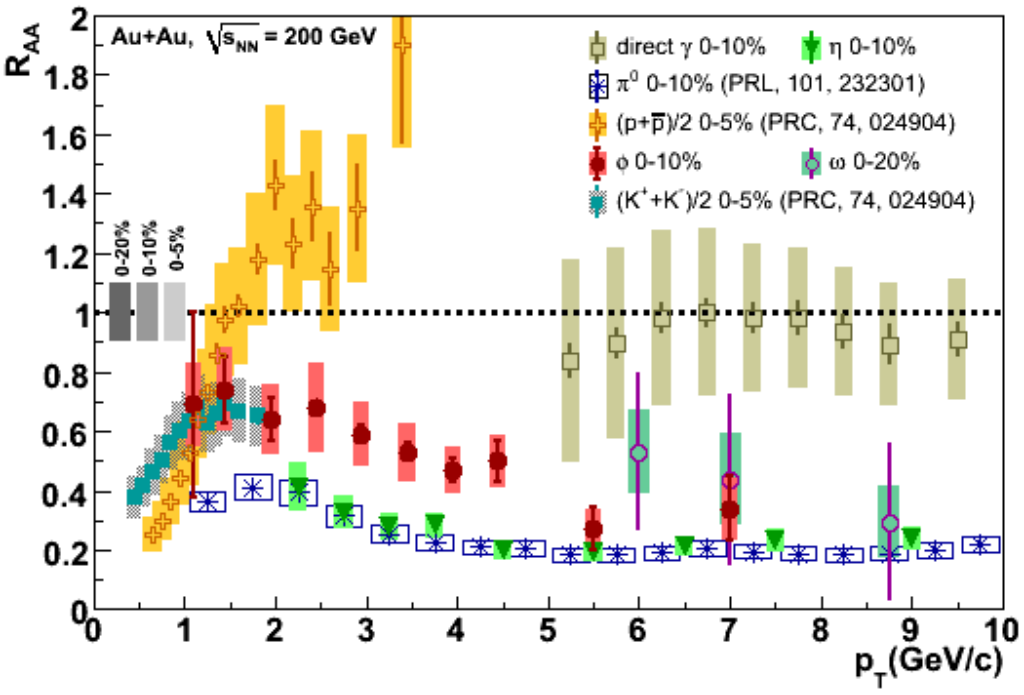

Figure 4.17: R_{AA} vs. p_T for ϕ, π^0, $(K^+{+}K^-)$, η, ω, $(p+\bar{p})$ and direct γ in central Au+Au collisions. Values for $(K^+{+}K^-)$ and $(p+\bar{p})$ are from Ref. [121], for π^0 are from Ref. [65], for η, ω and direct γ are from Ref. [61]. The uncertainties related to $\langle N_{coll}\rangle$ determination is shown as boxes on the left. The global uncertainty of $\sim 10\%$ related to p+p reference normalization is not shown.

$f_{b/A}(x_b, Q_b^2)$ are parton distribution functions, and $\widetilde{\mathcal{D}}_{c\to h}(z_c, Q_c^2)$ is a medium-modified fragmentation function. The parton distribution functions and the vacuum fragmentation functions are process-independent and determined experimentally in deep-inelastic $e^{\pm}$+A and e^++e^- collisions, respectively. The entire effect of energy loss is handled via the calculation of the medium modification to the vacuum fragmentation function. The various models differ in their assumptions about the relevant scales (energy, E, and virtuality, Q^2, of the initial parton, and typical momentum, μ, of the medium and its spatial extent, L), as well as in the way they deal with the space-time evolution of the medium. For a recent review of the energy loss models and their comparison to data see [129].

In all models, the final hadronization of the hard parton is assumed to occur in the vacuum, after the parton, with degraded energy, has escaped from the system. Since hadronization of the parton depends only on its identity but not on its history, the ratio of different identified high-p_T hadrons should stay unchanged with respect to p+p collisions, while their absolute yield should be suppressed with respect to the N_{coll}-scaled p+p results [130]. This seems to be the case at $p_T \gtrsim 5.5-7$ GeV/c where the suppression patterns of different hadrons exhibit similar suppression levels and therefore it is only in this region

that quantitative comparison of energy loss models to the data can be made. However, at intermediate p_T the dependence of the suppression patterns on particle species shown in Fig. 4.17 is inconsistent with the picture of hadron production through hard-scattering followed by energy loss in the medium and fragmentation in vacuum. The data in this range require involvement of an additional particle production mechanism.

Quark recombination models [131–135] advocate partonic recombination as the dominant mechanism for hadron production at intermediate p_T. These models take into account the interplay between thermal and fragmentation components of the partonic spectrum and are able to reproduce hadronic spectral shapes. The ϕ meson data shown in this work present a new constraint for these models.

4.3.2 R_{dA} comparison of ϕ meson to other identified particles

Fig. 4.18 shows a comparison of the R_{dA} for ϕ from this work, π^0 and η from Ref. [136], proton and kaon from Ref. [121] and ω from Ref. [137] for minimum bias d+Au collisions. While the proton R_{dA} exhibits an enhancement usually associated with the Cronin effect [122–126], the R_{dA} for π^0, η and ω suggest smaller or no enhancement at $p_{\mathrm{T}} = 2-4$ GeV/c. The R_{dA} for ϕ measured in minimum bias d+A collisions follows the same trend and is in better agreement with the R_{dA} of other mesons than with that of the proton. No meson species dependence is observed in R_{dA} within uncertainties.

4.3.3 Comparison to Cu+Cu collisions.

Measurements of the nuclear modification of the ϕ meson in Cu+Cu collisions [78] bridge the gap between the Au+Au and d+Au measurements. Comparative studies of Au+Au and Cu+Cu data sets allow to test how sensitive is the particle production at high-p_T to the collision geometry. Furthermore, smaller colliding systems, like Cu+Cu, allow to study the region of small N_{part} values ($\lesssim 50$), corresponding to peripheral Au+Au collisions where statistic is limited, with greater precision and in more centrality bins. Additionally, the nuclear modification in this N_{part} range can be studied with reduced uncertainties in N_{coll} with the smaller Cu nucleus [92].

The ϕ's R_{AA} measured in Au+Au and Cu+Cu collisions for similar number of participating nucleons N_{part}, i.e. similar energy density, are in agreement as demonstrated in Fig. 4.19. This is illustrated more generally in Fig. 4.20 where the modification factor integrated over various p_T ranges is shown as a function of N_{part}. We can conclude from these figures that over the entire range of p_T the ϕ meson production seems to depend only on the size of the overlapping system and not on the geometry of the nuclear overlap.

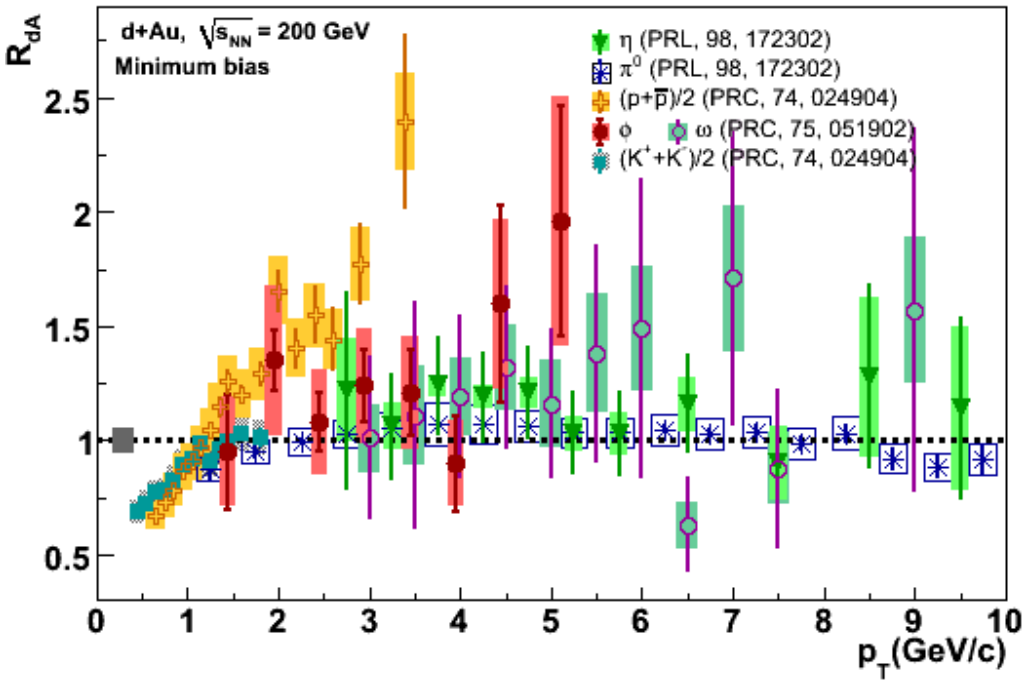

Figure 4.18: R_{dA} vs. p_T for ϕ, π^0, $(K^+{+}K^-)$, η, ω, and $(p+\bar{p})$ in minimum bias d+Au collisions. Values for $(K^+{+}K^-)$ and $(p+\bar{p})$ are from Ref. [121], for π^0 and η are from Ref. [136], for ω are from Ref. [137]. The uncertainties related to $\langle N_{coll}\rangle$ determination is shown as boxes on the left. The global uncertainty of $\sim 10\%$ related to p+p reference normalization is not shown.

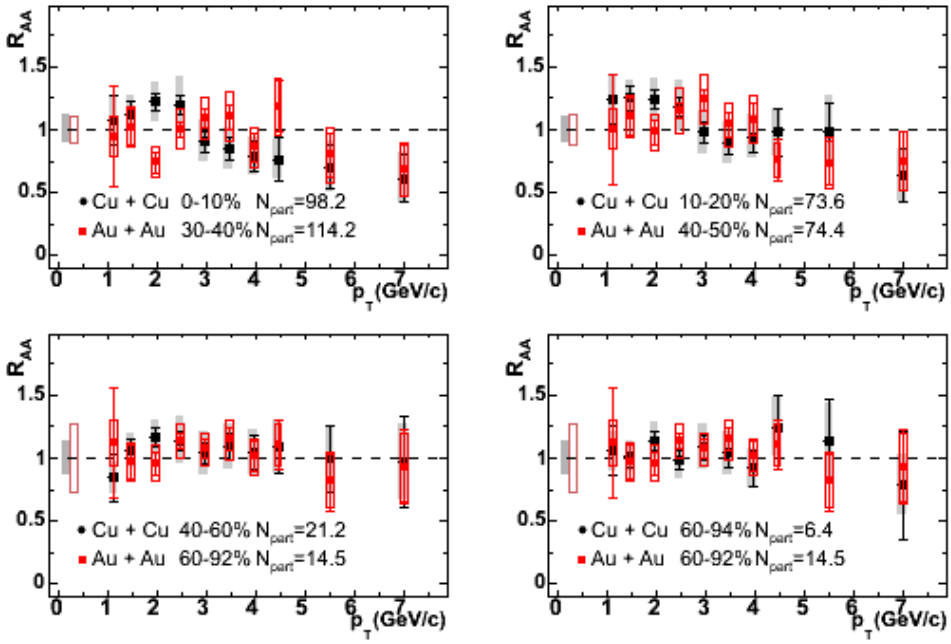

Figure 4.19: R_{AA} for Au+Au and Cu+Cu collisions at $\sqrt{s_{NN}} = 200$ GeV measured at similar numbers of N_{part}.

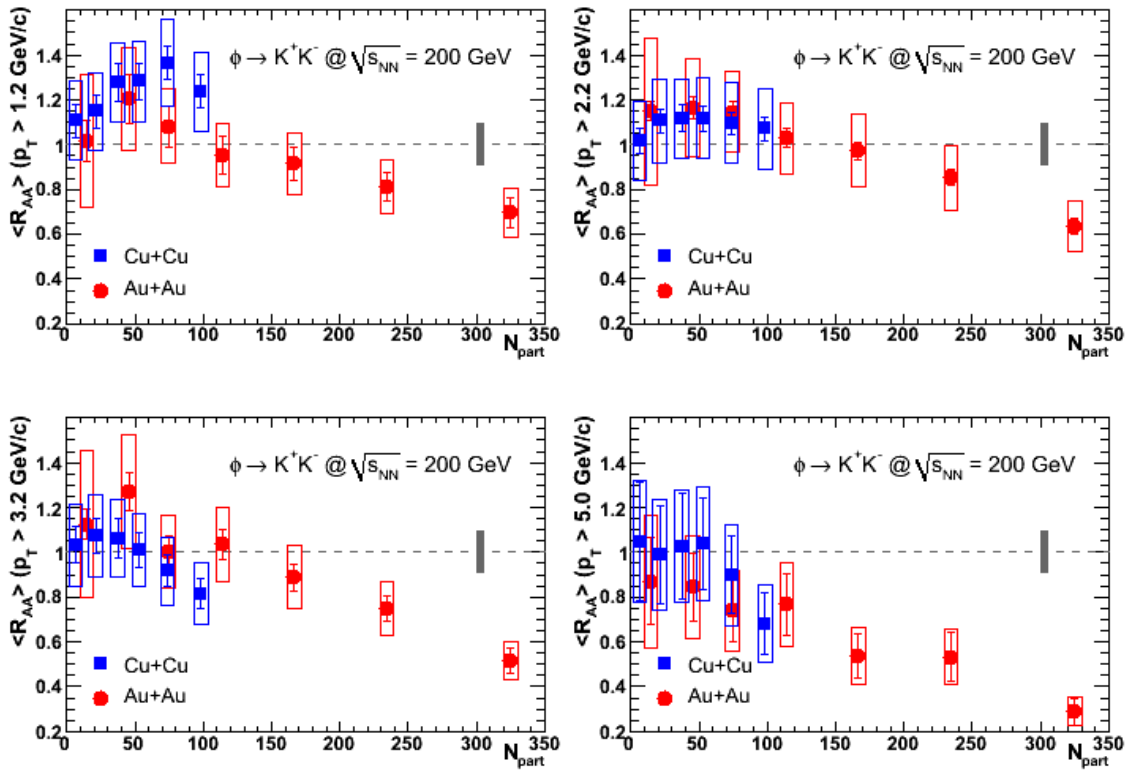

Figure 4.20: R_{AA} integrated over various p_T ranges (as indicated on the ordinates) for Au+Au and Cu+Cu collisions at $\sqrt{s_{NN}} = 200$ GeV as a function of N_{part}.

Chapter 5

Hadron Blind Detector

5.1 Measurement of low-mass dielectrons in PHENIX

Dileptons are considered as one of the most promising observables for detecting and studying the properties of the hot and dense matter formed in ultra-relativistic heavy-ion collisions [138, 139]. Deconfinement and chiral symmetry restoration, which are the two fundamental characteristics of the QGP, can manifest themselves in the dilepton invariant mass spectrum. For instance, identification of the thermal radiation ($q\bar{q} \rightarrow \gamma^* \rightarrow e^+e^-$) is a signal of deconfinement and in-medium modifications of the light vector mesons can serve as a probe of chiral symmetry restoration. Unfortunately, dilepton probes have rather small yields and compete with huge backgrounds from hadronic processes and γ conversions. The main background sources populating the mass region of interest are: two-body resonance decays of the ρ, ω and ϕ; Dalitz decays of π^0, η, η' into $\gamma\, e^+e^-$ and ω into $\pi^0 e^+e^-$; semi-leptonic decays of D meson. A precise and complete knowledge of the background sources is therefore imperative before drawing any reliable conclusion on a new source of dileptons or in-medium modification of spectral functions.

PHENIX is the only experiment at RHIC that can measure low-mass electron pairs. The central arm spectrometers have very good electron identification capabilities provided by the RICH and EMCal. The RICH is used mainly for electron/pion separation exploiting the fact that electrons radiate Čerenkov light in the CO_2 gas radiator, while other particle species do not generate light as long as their momentum p is below the corresponding Čerenkov threshold[1]. Further electron identification (electron/hadron separation) is achieved by the EMCal which measures the energy E, deposited by particles traversing through it. Electrons deposit most of their energy in the EMCal, and have a small mass, so the ratio of the energy deposited in the calorimeter to the momentum of

[1] CO_2 has the a pion Čerenkov threshold of 4.65 GeV/c [96].

the track, E/p, is close to one. Hadrons lose only some fraction of their energy in the EMCal and thus typically have E/p smaller than one. PHENIX also has an excellent mass resolution of 1% at the ϕ mass, mandatory for precise spectroscopy of the light vector mesons.

However, in its original configuration [85], the PHENIX capabilities for a good measurement of low-mass electron pairs with $m_{e^+e^-} < 1$ GeV/c^2 are limited by a huge combinatorial background originating from unrecognized γ-conversions and π^0 Dalitz decays. The first measurements of the dielectron continuum in Au+Au collisions at RHIC energies performed by PHENIX [140], has a signal to background ratio of about 1/200 at invariant mass $m_{e^+e^-} \sim 500$ MeV/c^2 as can be seen in Fig. 5.1 showing the foreground, background and subtracted e^+e^- invariant mass spectra. The systematic errors are dominated by those from the combinatorial background subtraction due to the small signal-to-background ratio.

To extend the capability of low-mass electron pair measurement in PHENIX, the Weizmann group proposed to upgrade the PHENIX experimental set-up by adding a Hadron Blind Detector (HBD) [141–143].

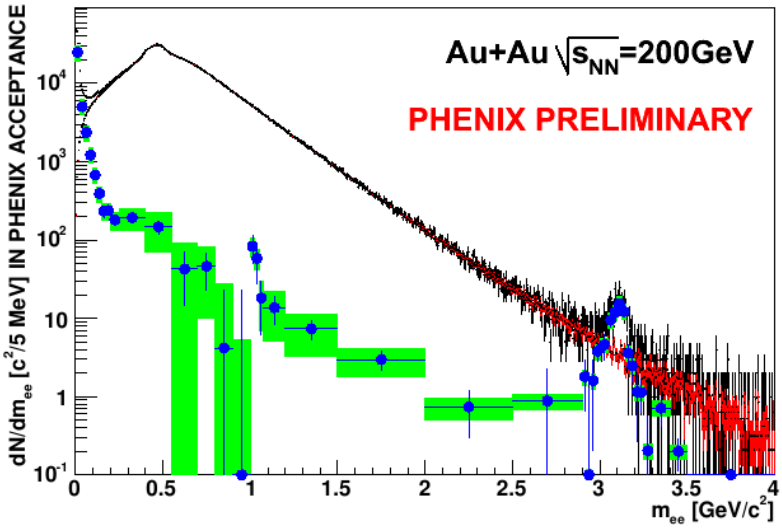

Figure 5.1: The foreground (black), background (red) and subtracted (blue circles) e^+e^- invariant mass measured by PHENIX in Au+Au collisions at $\sqrt{s_{NN}} = 200$ GeV [140]. Statistical and systematic errors are shown by vertical bars and shaded bands, respectively.

5.2 The HBD concept

The HBD is a conceptually novel threshold Čerenkov detector, located in the inner part of the PHENIX detector (see Fig. 5.2). The HBD's primary purpose is to tag electrons

originating from γ conversions and π^0 Dalitz decays in the field free region surrounding the collision vertex. Since the opening angle of the pairs is preserved in the absence of magnetic field, the electron pairs from these sources can be easily identified in the HBD, based on their smaller opening angle as compared to those from light vector mesons, and thus be rejected. The size of the HBD is constrained by the space between the beam pipe outer radius of $\sim$5 cm and the available magnetic field-free region (see right panel of Fig. 2.3) extending up to 60 cm in the radial direction. The system specifications were determined from conceptual Monte Carlo simulations [141]. In order to reject the π^0 Dalitz decay and conversion background by at least two orders of magnitude, the detector must have an electron identification efficiency of at least 90%, a double (electron) hit recognition of $\sim$90%, together with a moderate π rejection factor as low as 50-100.

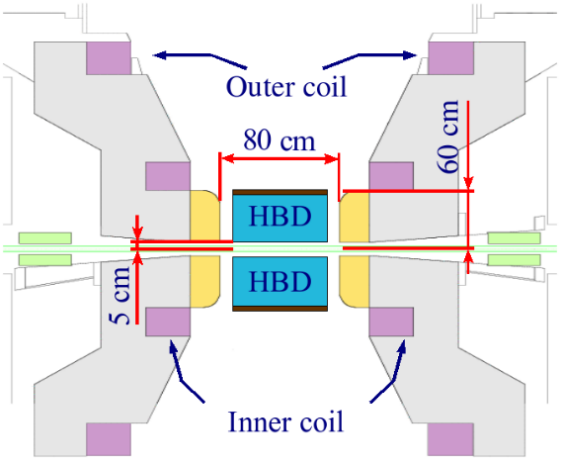

Figure 5.2: Layout of the inner part of the PHENIX detector, showing the HBD location.

After careful consideration of relevant options for the key elements (radiator and detector gases, window, photocathode, electron multiplication element and readout scheme), the following choice of the main HBD elements was made: a 50 cm long Čerenkov radiator directly coupled to a triple Gas Electron Multiplier (GEM) [144] detector with a cesium iodide (CsI) film evaporated on the top surface of the upper-most GEM, and CF_4 used as detector as well as radiator gas.

Each triple GEM module consists of one gold plated GEM with a cesium iodide (CsI) film evaporated on its top surface and two standard GEMs below. A stainless steel mesh 1.5 mm above the stack can be biased by a positive or negative voltage with respect to the upper GEM. Depending on the drift field direction, charge produced by ionizing particles in the gap between the mesh and the GEM stack can either be collected by the upper GEM (forward bias), or repelled from it (reverse bias) as depicted on Fig. 5.3. The reverse bias mode is the normal HBD operating regime.

The GEM stack is connected to the radiator in a windowless configuration, so that light from particles passing trough the radiator can directly reach the CsI photocathode plane, forming a circular blob image on it. The photoelectrons emitted from the photocathode are sucked into the GEM holes by the strong electric field inside these holes, and after three stages of amplification in the GEMs the electron avalanche is read out in a pad plane located at the bottom of the GEM stack (see Fig. 5.3).

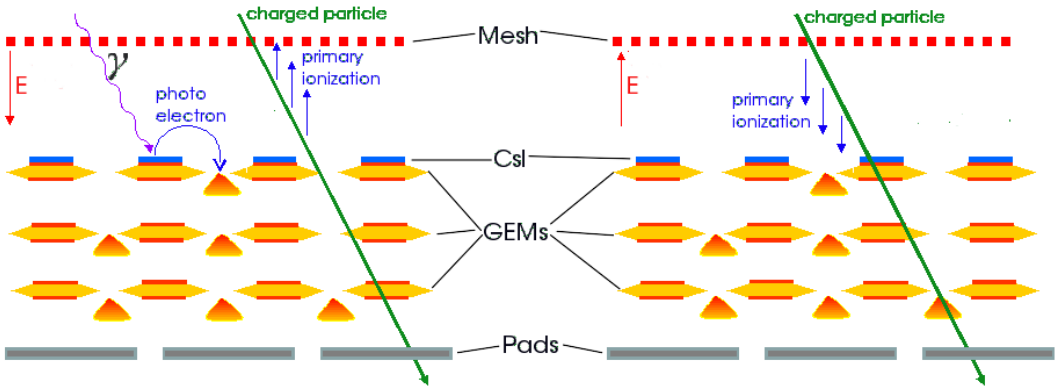

Figure 5.3: Triple GEM detector configuration in the reverse bias mode (left) and in the forward bias mode (right).

The proposed detector scheme exhibits a number of very attractive features:

- The detector is sensitive to radiation over a very broad bandwidth (from ∼6 eV given by the CsI threshold to ∼11.5 eV given by the CF_4 cut-off) resulting in a figure of merit N_0 calculated to be close to 800 cm^{-1}. Assuming an ideal detector with 100% gas transparency and 100% photoelectron collection efficiency, the resulting number of photoelectrons per incident electron is N_{pe} ≈36 for the proposed radiator length.

- Another important advantage of the detector scheme is that it allows the use of a photocathode in reflective mode[1]. In such a geometry the photocathode is insensitive to photons generated in the avalanche.

- The pad plane has hexagonal pads of size slightly smaller than the size of the blob ∼10 cm^2. The shape and size of the pads have been optimized such that an electron entering the HBD fires at most three pads, whereas the probability of a single pad hit is negligibly small. On the contrary, a hadron will always produce a single pad hit, since the ionization charges are very well localized providing a very simple and strong electron/hadron separation.

[1] In reflective photocathodes light is incident on a thick photoemissive film and the electrons are emitted backwards.

- The relatively large pad size translates into a low granularity of the detector. In addition, keeping in mind that photoelectrons produced by a single electron will be distributed over not more than three pads, one can expect a primary charge of $\sim$10 electrons/pad. Therefore, the operating gain of the triple GEM can be as low as a few times 10^3, which is a significant advantage for a stable operation of the detector.

5.3 R&D project

An intensive R&D was carried out to demonstrate the overall concept validity and to address a number of questions raised by this novel detector concept. In particular, the following questions were addressed:

- Pure CF4 had never been used as detector gas. Therefore stable operation of a triple GEM detector with a CsI photocathode layer in pure CF_4 at gains of $\sim 10^4$ needed to be demonstrated.
- The absolute quantum efficiency (QE) of the CsI photocathode has been studied by a large number of groups [145, 146]. However, all these measurements were performed for photon energies below 8.5 eV. Since CF_4 is transparent up to 11.5 eV extension of the absolute QE measurement range to higher photon energies was desirable.
- There are several mechanisms that may lead to degradation of the CsI photocathode QE or to aging of the GEM foils during the long term detector operation in the presence of a large flux of heavily ionizing particles. Owing to the strong reactivity of the CF_4 derivatives, possibly formed in the ion-electron avalanche, the metal or insulator surfaces of the GEMs, as well as CsI photocathode surface may receive a permanent chemical damage. In order to check the compatibility between the detector vessel construction materials, GEMs, CsI photocathods and CF_4 a global irradiation test was required.
- The detector characteristic properties, i.e. "blindness" to hadrons and high detection efficiency for electrons needed to be demonstrated.

Setup and experimental conditions For all R&D measurements, we used GEMs produced at CERN of size 3×3 cm^2 and 10×10 cm^2. The GEMs were made from a 50 μm thick Kapton[1] foil, with 5 μm copper cladding on both faces, chemically perforated with holes, with an internal (external) diameter of 60 μm (80 μm) and a pitch of 140 μm. The

[1] Kapton is a registered trademark of Dupont, Inc.

GEMs that were used for photocathode deposition have the copper cladding coated with thin layers of nickel and gold to provide a CsI compatible substrate. In order to reduce the energy stored on the GEM the bottom side of the 10×10 cm^2 GEM foils were divided in 4 segments (10×2.5 cm^2 each). The GEM foils were stretched and glued between the two 0.5 mm thick FR4 frames. Each HV segment was connected to a common HV bus line through 20 MΩ resistor. The mesh electrodes were made from a stainless woven wire mesh stretched and soldered to a FR4 frame having a copper electrode at the circumference.

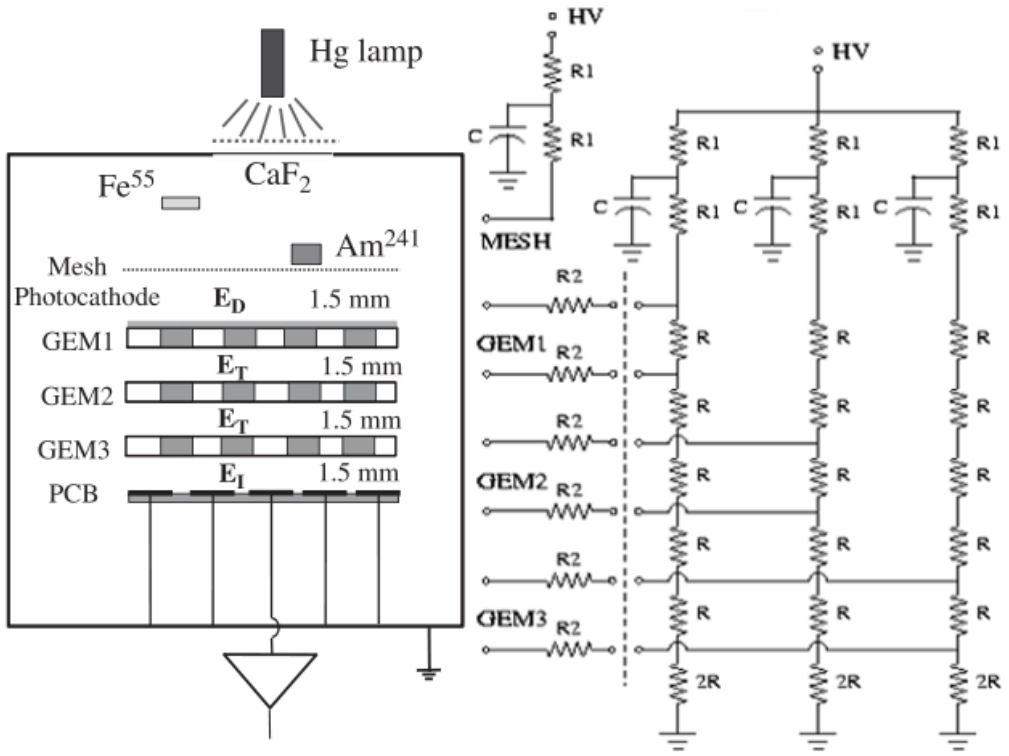

Figure 5.4: Setup of the triple GEM detector and its powering scheme. The Hg lamp, ^{55}Fe and ^{241}Am sources were used for measurements with UV-photons, X-rays and α-particles, respectively.

The detector, consisting of the mesh electrode, three GEMs, and PCB, was assembled inside a stainless steel box as shown in Fig. 5.4. The box can be pumped down to 10^{-6} Torr and has inlet and outlet gas lines to allow gas flushing. The assembly operations were performed in a high purity dry nitrogen atmosphere inside a glove-box to minimize damage of the CsI photocathode due to moisture and oxygen. After assembling the triple GEM detector, the stainless steal detector vessel is pumped by a turbopump to 10^{-6} Torr. Then the detector vessel is filled with the gas mixture needed for the particular experiment. All measurements were done in the gas flow mode at atmospheric pressure with an overpressure of 0.5 Torr in the detector vessel. Two gases were used for the measure-

ments: Ar/CO_2 (70:30) mixture and pure CF_4. The detector vessel was also equipped with a Hg lamp, ^{55}Fe and ^{241}Am sources for measurements with UV-photons, X-rays and α-particles, respectively. The Hg-lamp was used in the measurements with the CsI reflective photocathode. The lamp was positioned outside of the detector box, illuminating the photocathode through a UV-transparent CaF_2 window made in the detector box lid. An absorber placed above the window reduced the UV flux by about a factor of 1000 in order to prevent damage to the photocathode. The illuminated area of the detector was about 1 cm^2 and in this geometry the photoelectron current was about 2×10^6 electrons/mm^{2}s. The ^{55}Fe source was positioned on a moving arm inside the box at a distance of $\sim$40 mm from the mesh and could be moved out of the sensitive volume. The total rate of X-rays was kept at the level of 1 kHz. The ^{241}Am emitting 5.5 MeV α-particles was used to study the discharge limit in the presence of heavily ionizing particles. The source was attached to a moving arm that could be inserted at a distance of 1 mm above the drift mesh. In order to provide a high energy deposition and small energy dispersion in the drift gap the source was strongly collimated. The rate of α-particles was $\sim$100 Hz. The energy deposition in a 3 mm gas layer was estimated to be $\sim$1.1 MeV for CF_4 and $\sim$0.3 MeV for Ar/CO_2 producing $\sim20\times10^3$ and $\sim12\times10^3$ primary charges, respectively.

Powering scheme A three-branch resistive chain circuit, shown in Fig. 5.4, equipped with CAEN-N126 HV power supply was used to power the three GEMs. A second power supply, CAEN-471A, was used for the mesh. The main advantage of the three-branch resistive chain is that if a permanent short occurs in one GEM, the two other GEMs are totally unaffected. The resistors R2 are surface mounted on the GEM foils, and the rest of the resistive chain is mounted in a HV distribution box outside the HBD. The values of the various components are: R=5.6 MΩ, R1=1.2 MΩ, R2=20 MΩ and C=2 nF.

The normal operating voltage across each GEM to achieve a gain of 10^4 is almost 500 V. This corresponds to a total voltage of about 4700 V and a total current close to 270 μA supplied by the power supply, or close to 90 μA in each branch. To be precise the voltage across the GEM foil is equal to 506 V for a total voltage of 4700 V. Under normal operation, there is no current and no voltage drop across the resistors R2. However, if a short occurs in a HV segment of one of the GEMs, then this GEM will have a lower voltage of only 451 V whereas the other two GEMs will remain at 506 V. This will result in a smaller overall gain of the detector by a factor of about 2.5. One can restore the nominal voltage and nominal gain by replacing the 5.6 MΩ resistor of the shorted GEM with a 6.5 MΩ resistor.

The system must be protected against discharges. If a discharge occurs in one GEM, the power supply should ramp down (to avoid continuous discharges). The mesh power

supply should also ramp down simultaneously in order to avoid an excessive HV gradient between the mesh and the first GEM. The difference between the total current in case of a short in one GEM and the total current in regular regime is $\sim$1.2 μA. The CAEN-N126 module includes protection against over-current with a precision of 0.1 μA and therefore provides reliable protection in case of discharge. The power supply tripping threshold was always kept at 1 μA above the normal current.

CsI photocathode evaporation The deposition of the CsI layer was performed at the Radiation Detection Physics Laboratory at the Weizmann Institute. Fig. 5.5 shows a schematic illustration of the set up used for CsI-photocathode evaporation. It comprises a high vacuum chamber connected via a gate valve to a turbopump, a thermal evaporation station at the bottom of the vacuum chamber, a shutter, and a thickness monitor system. The removable glass bell jar closes the vacuum chamber with a thick rubber gasket and allows easy access into the evaporation chamber. The photocathodes were produced by evaporation of a $\sim$2000 Å thick layer of CsI on a gold plated GEM substrate in vacuum ($\sim 10^{-6}$ Torr).

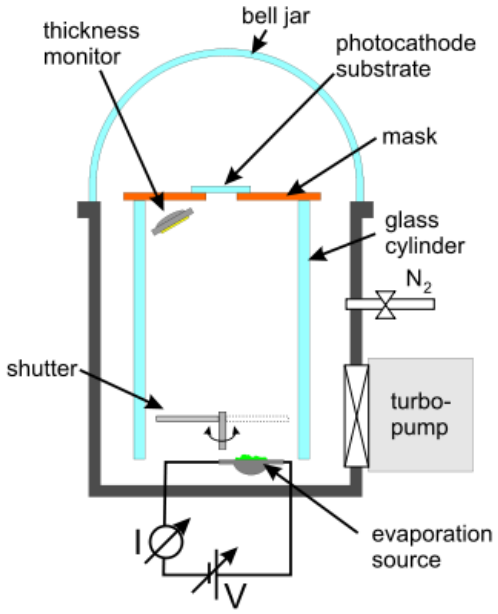

Figure 5.5: Schematic view of the set up used for CsI-photocathode evaporation [147].

5.4 R&D results

5.4.1 Gain in Ar/CO_2 and CF_4

The absolute gain was measured with a ^{55}Fe X-ray source using the knowledge that 5.9 keV photons release 210 electrons in Ar/CO_2 and 110 electrons in CF_4, corresponding to 26 eV and 54 eV per electron-ion pair, respectively [148]. Pulse height distributions from a ^{55}Fe source measured at a gain of 10^4 in Ar/CO_2 and CF_4 are shown in Fig. 5.6. In Ar/CO_2 the principal peak (5.9 keV) and the escape peak are clearly seen. The FWHM is typically 22% and 38% for Ar/CO_2 and CF_4, respectively.

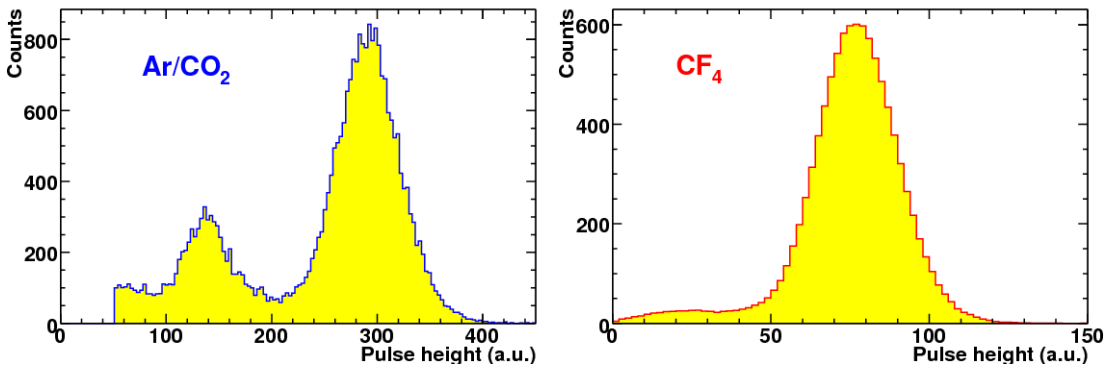

Figure 5.6: Pulse height spectrum of ^{55}Fe X-rays with Ar/CO_2 (left) and CF_4 (right).

Fig. 5.7 shows the typical gain curves measured in Ar/CO_2 and CF_4 with 3×3 cm^2 and 10×10 cm^2 GEMs. The data show that for the same gain CF_4 requires ∼140 V higher operation voltages compared to Ar/CO_2, otherwise the gain-voltage characteristics are similar for both gases. A gain of 10^4 in CF_4 is obtained at a voltage across each GEM of about 510 V. Results reported in [149] confirm our measurements.

5.4.2 Avalanche charge saturation effect and discharge probability

A strong deviation of the gain dependence on voltage across the GEM foil from the exponential growth at high gains was found in CF_4. For 3×3 cm^2 GEMs this feature of CF_4 is seen for $\Delta V_{GEM} \gtrsim 530\ V$ in Fig. 5.7. The effect is much more pronounced and appears at significantly lower voltages across the GEM foils when the detector is irradiated with ^{241}Am α-particles. Fig. 5.8 shows the total charge in the avalanche. Since there was a suspicion that the observed suppression at high values of ΔV_{GEM} is due to the saturation of the preamplifier, the measurements were repeated without preamplifier at the 1 MΩ input of an oscilloscope. Both measurements were performed under identical conditions and for this purpose the preamplifier was calibrated in units of input charge. In order to obtain

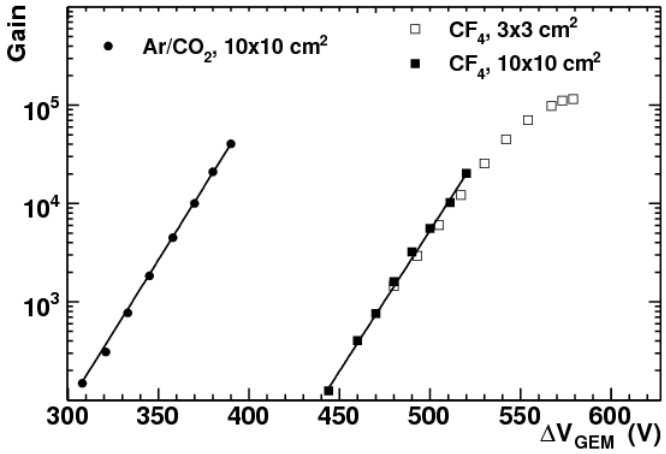

Figure 5.7: Gain as a function of GEM voltage measured with ^{55}Fe X-ray source. The lines represent exponential fits to the data taken with 10×10 cm^2 GEMs.

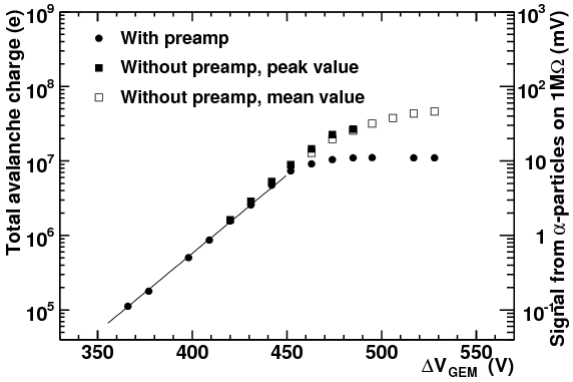

Figure 5.8: Pulse height of the signal from α-particles measured with and without preamplifier as a function of GEM voltage.

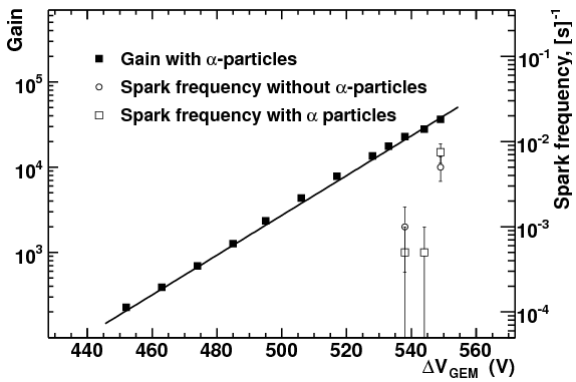

Figure 5.9: Spark frequency and detector gain as a function of voltage across the GEM with and without α-particle irradiation.

the relation between the signal measured without preamplifier and the input charge the results were normalized in the range $\Delta V_{GEM} = 420 - 440$ V where both measurements could be performed and the amplifier was still far from saturation. More details about these measurements can be found in [150].

The gain curve obtained in the measurements without preamplifier saturates when the total charge in the avalanche exceeds 4×10^7 electrons. This effect of the charge saturation in CF_4 makes the detector robust against discharges, which is a crucial characteristic for stable operation in a high multiplicity environment of charged particles.

Fig. 5.9 shows the gain-voltage characteristic of the detector together with the spark frequency measured with and without α-particle irradiation. The duration of each measurement was ∼2000 s, i.e. the maximum number of sparks counted in the highest point was about 20. In the operational range of the gain for the proposed detector (up to 10^4)

the spark probability is found to be negligible. The results also indicate that discharges are independent of the flux of heavily ionizing particles passing through the detector and appear to be determined by local GEM defects. Subsequent studies of gain stability and sensitivity of the triple GEM detector to background particles produced in Au+Au collisions, performed during a full luminosity Au+Au run within the PHENIX central arm [151], led to the same conclusion. During these studies the detector was operated for over 24 hours, in close proximity to the beam pipe (50 cm) with no sparking or discharges observed.

5.4.3 Aging studies

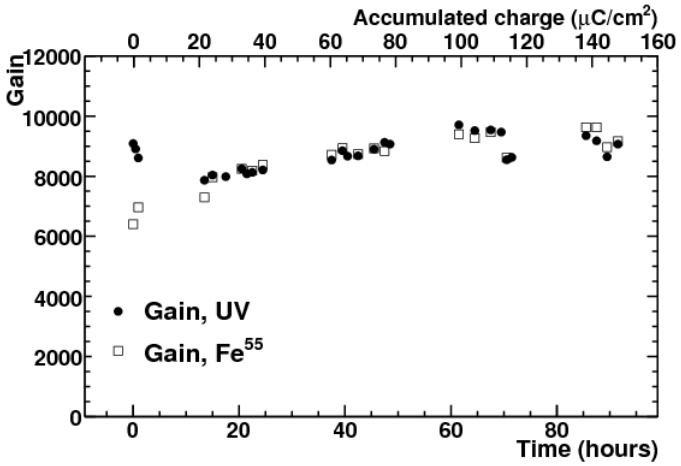

Figure 5.10: Results of aging test performed on a 10×10 cm^2 triple-GEM detector with a CsI reflective photocathode. Open squares correspond to the measurements with ^{55}Fe, solid circles represent the measurements with UV irradiation.

Aging studies of the triple GEM detector with a CsI photocathode evaporated on the top of the first GEM were performed with an intense UV Hg-lamp and ^{55}Fe X-ray source. The detector was irradiated by UV lamp continuously for about 100 hours with short interruptions every few hours. During these interruptions the UV irradiation was stopped and the ^{55}Fe source was inserted into the detector box for a gain monitoring measurement. The current to the PCB was continuously monitored during the test. By comparing the gain measured with the ^{55}Fe source and with the UV-lamp one can decouple the degradation of the photocathode from the deterioration of GEMs.

Fig. 5.10 shows the gain obtained with ^{55}Fe (open squares) and with UV lamp (solid circles) as a function of the irradiation time and accumulated charge. The gain variations during the test did not exceed 20% and during the second half of the test they were even smaller ($\lesssim$5%). The results of the aging studies showed that there are no significant

changes neither in the CsI photocathode efficiency nor in the gain after exposure of the detector to an accumulated total charge of 100 μC/cm^2 corresponding to $\sim$10 years of the HBD operation in PHENIX.

5.4.4 CsI quantum efficiency

The determination of the absolute QE of a photocathode requires an absolutely calibrated light source or ties to some calibrated standards. In our measurements we used as a reference a calibrated photomultiplier tube (PMT). The schematic view of the CsI quantum efficiency measuring apparatus is shown in Fig. 5.11. The system comprises a vacuum ultraviolet (VUV) monochromator (Jobin Yvon H20, 115-500 nm), which contains a deuterium lamp (Hamamatsu L7293, 115-320 nm), monochromator optics, a LiF beam splitter (cut-off at 105 nm), a lamp intensity monitor (PMT-0, Hamamatsu R1460) and a LiF output window to the detector box. The detector box contains an absolutely calibrated PMT (Hamamatsu R6836) operated in the photodiode mode (gain=1), the sample mesh/photocathode and a rotating UV mirror to deflect the beam alternatively to the CsI layer and to the PMT. There are collimators of 8 mm diameter in front of each target to ensure equal path length and equal solid angles.

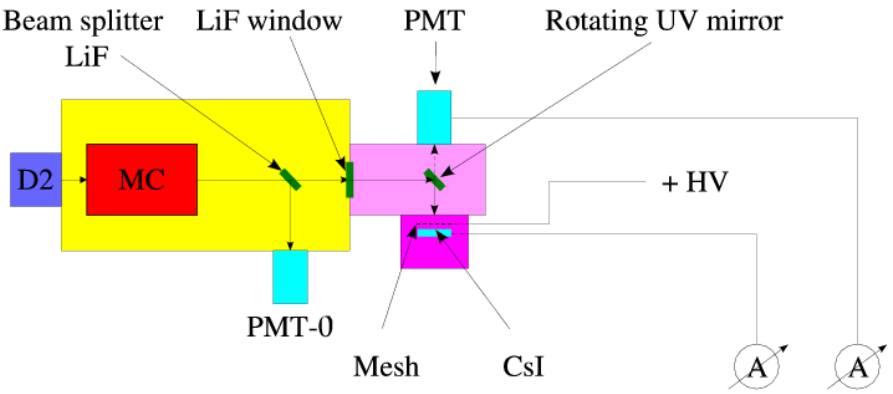

Figure 5.11: Schematic view of the CsI quantum efficiency measuring apparatus.

Fig. 5.12 shows the currents of the CsI and PMT as measured in vacuum over the wavelength range of 120-200 nm (the corresponding photon energy range is 6.2-10.3 eV). The measurements were repeated with CF_4 gas at atmospheric pressure.

The absolute QE of the CsI layer at a given wavelength λ is given by

$$QE_{\mathrm{CsI}}(\lambda) = \frac{QE_{\mathrm{PMT}}(\lambda)}{C_1 \cdot C_2} \cdot \frac{I_{\mathrm{CsI}}(\lambda)/I_0^{\mathrm{CsI}}(\lambda)}{I_{\mathrm{PMT}}(\lambda)/I_0^{\mathrm{PMT}}(\lambda)}, \tag{5.1}$$

where $QE_{\mathrm{PMT}}(\lambda)$ is the absolute QE of the PMT at the wavelength λ, C_1 is the mesh

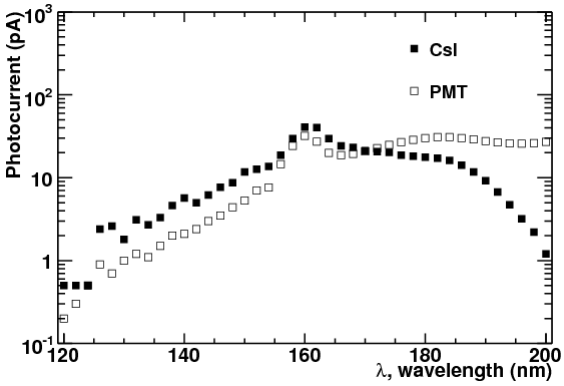

Figure 5.12: Photocurent from the CsI layer and the reference PMT as function of wavelength.

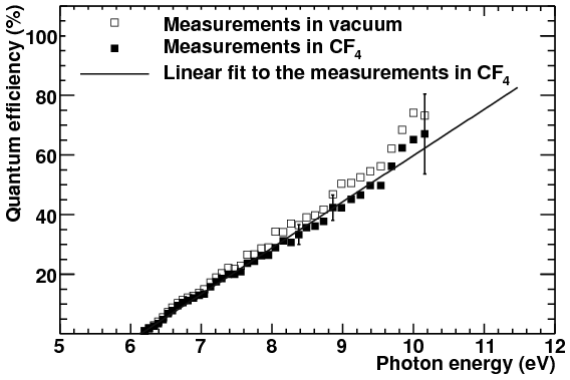

Figure 5.13: Absolute quantum efficiency of CsI in vacuum and CF_4 over the bandwidth 6.2-10.3 eV.

transparency (C_1=0.81) and C_2 is the opacity of the CsI layer due to the GEM holes (C_2=0.833), $I_{\rm PMT}(\lambda)$ and $I_{\rm CsI}(\lambda)$ are the CsI photocathode and PMT currents measured at that wavelength, and $I_0^{\rm PMT}(\lambda)$ and $I_0^{\rm CsI}(\lambda)$ are the currents from the lamp intensity monitor (PMT-0) measured simultaneously with the measurements of the currents from PMT and CsI photocathode, respectively.

Fig. 5.13 shows the CsI absolute QE over the bandwidth 6.2-10.3 eV as measured in vacuum and CF_4. The quantum efficiency in CF_4 is systematically lower by about 10-15% than in vacuum. One possible reason for this effect could be the backscattering of photoelectrons to the photocathode surface due to elastic collisions with the gas molecules. The results presented here are in very good agreement with those of [146] which covered the range 5.85-8.3 eV (150-212 nm). Extrapolating linearly the measured dependence of the quantum efficiency on the photon energy from 10.5 eV to 11.5 eV, gives a figure of merit of N_0=822 cm^{-1} and a number of photoelectrons $N_{p.e.} \simeq$36 for the proposed radiator length of 50 cm[1].

5.4.5 Response to mips, α-particles and UV-photons

To study the key properties of the HBD i.e. "blindness" to hadrons and high detection efficiency for electrons we looked at the detector response to mips, α-particles and UV-photons. The mip response was measured during the beam test at the KEK-PS, and the α-particles and UV-photons responses were measured in laboratory conditions using the setup described in Section 5.3.

The test beam data were taken with a secondary beam of negative particles (mainly pi-

[1]This is estimated under ideal conditions assuming 100% gas transparency and 100% photoelectron collection efficiency.

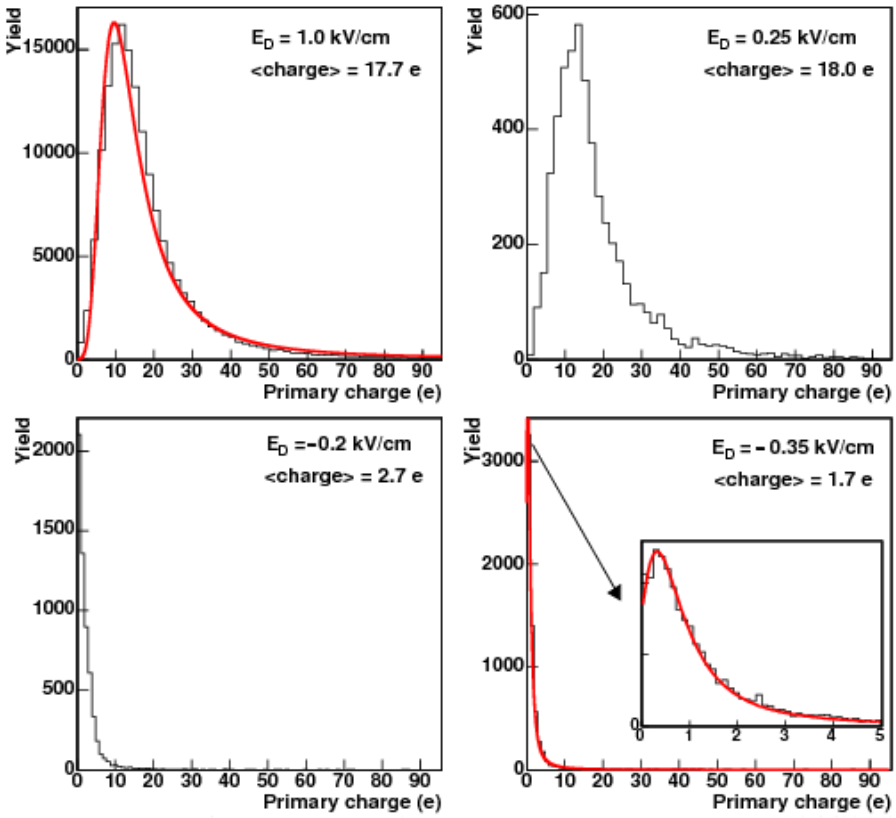

Figure 5.14: Pulse-height spectra measured with 1 GeV/c pions at various values of the drift field E_D in the gap between the mesh and the upper GEM. The solid lines in the upper left and bottom right panels represent fits to a Landau distribution of the measured spectra. The insert in the bottom right panel is an expanded view of the low signal part of that panel.

ons) containing a few percent of electrons. Fig. 5.14 shows the pulse-height spectra, after pedestal subtraction, measured with 1 GeV/c pions at various values of the drift field E_D in the gap between the mesh and the upper GEM. The spectra exhibit a clear minimum ionizing peak and are well described by a Landau distribution [152]. For E_D=1 kV/cm (top left panel), the measured mean amplitude is $\sim$18 electrons corresponding to a primary ionization of 120 charges/cm or 54 eV/ion-pair assuming an energy loss of dE/dx=7 kV/cm [153]. As long as E_D remains positive the pulse-height distribution shape does not change much as seen in the two top panels. For negative values of E_D a strong suppression of the ionization signal is observed. The mean amplitude drops to $\sim$10% of its value for a positive field (bottom right panel) indicating that the collection of ionization charges occurs only from a thin layer ($\sim$150 μm) above the first GEM surface and from the gap between the first and second GEMs. The mean amplitude as a function of E_D is shown in Fig. 5.15. The figure shows also the results of similar measurements performed with

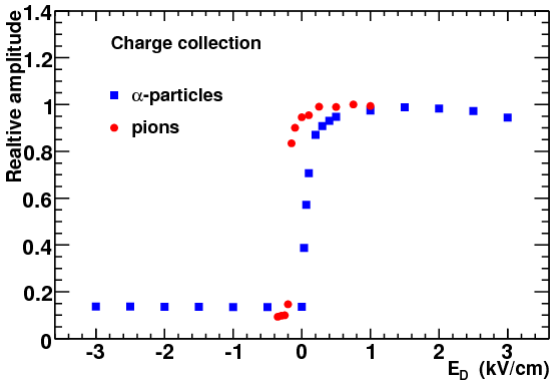

Figure 5.15: Collection of ionization charge measured with pions and α-particles vs. the drift field E_D in the gap between the mesh and upper GEM.

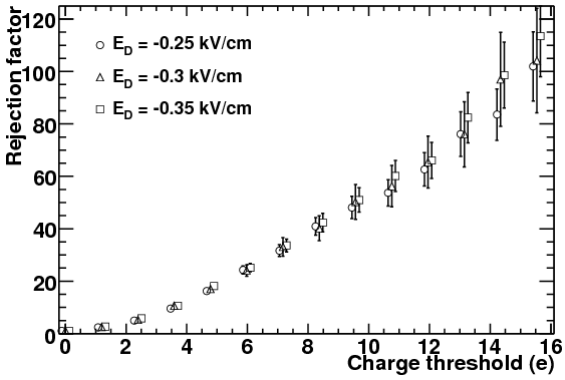

Figure 5.16: Hadron rejection factor as a function of a cut on the pion signal. The error bars represent the statistical uncertainties.

α-particles. A step-function like behavior is seen in both cases: the amplitude decreases sharply when the polarity of the drift field is switched and this occurs within a ΔE_D range of ∼0.1 kV/cm. The small difference in the values of the field at the onset of the signal drop is well within the uncertainties of the absolute high voltage values of the power supplies used in the two measurements.

The hadron rejection factor derived from the pion spectra measured for a few negative values of the E_D field is shown in Fig. 5.16. The rejection is limited by the long Landau tail and depends on the charge threshold, that can safely be applied preserving the electron collection efficiency. Rejection factors of the order of 50 can be achieved with an amplitude threshold of 10 electrons. Combining the hit size information to the amplitude response allows to achieve a much larger hadron rejection factor.

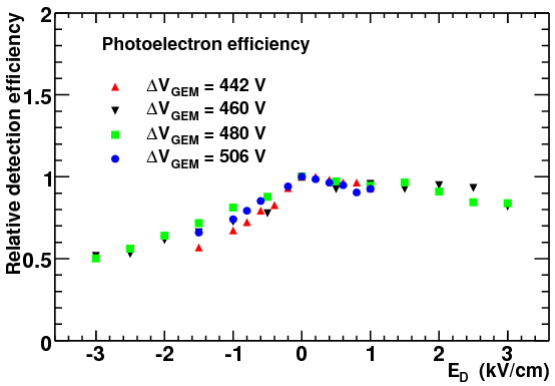

Figure 5.17: Photoelectron collection efficiencies for different gains vs. the drift field E_D in the gap between the mesh and upper GEM.

Fig. 5.17 shows the photoelectron collection efficiency as a function of E_D. The effi-

ciency was determined by illuminating the CsI photocathode with UV-photons from the Hg lamp through the CaF_2 window and measuring the photocurrent at the PCB for different voltages across the GEMs. The range of voltages used in the measurements (from 442 to 506 V) corresponds to gas gain variations of more than a factor of about 40. The maximum of the relative photoelectron collection efficiency occurs at 0 kV/cm for all voltages across the GEMs. So, we define it to be one at $E_D = 0$ kV/cm to allow an easy comparison between the various measurements. The efficiency slightly decreases as the field increases at positive E_D and it also drops off rather slowly at negative E_D as the field becomes more and more negative.

Combining the results from Fig. 5.15 and Fig. 5.17 it is clear that the best performance can be achieved at slightly negative drift field: while the bulk of the hadrons is suppressed, the collection efficiency of the photoelectrons remains very high.

5.5 HBD construction

5.5.1 Vessel construction

The HBD vessel was designed and built by our group at the Weizmann Institute. The HBD has two identical arms (see exploded view of one arm in Fig. 5.18), each one covering 135° in azimuth and $|\eta| < 0.45$. This larger acceptance as compared to the one of the central arms provides a generous veto area helping to reject close pairs in which one of the tracks is outside of the PHENIX acceptance [143]. Each arm is formed by ten panels glued together, a pair of FR4 frames that provide rigidity to the detector vessel and two side panels, attached to the FR4 frames with plastic screws. The panels consist of a 19 mm thick honeycomb core (a 13 mm thick honeycomb is used for the side panels) and a pair of 0.25 mm thick FR4 sheets glued to it on both sides. The detector entrance window is made of 127 μm thick mylar foil coated with 100 nm aluminum. The window is placed between two FR4 supports bolted to each other with an O-ring seal allowing easy replacement of the window if needed. One of the window supports is glued into the vessel. Among the eight smaller back panels the central six are equipped with two triple GEM photon detector modules on the inside, and connected to the Front End Electronics (FEE) board attached to the outer surface of the detector. The other two back panels are used for the detector services: gas in/out, high voltage distribution circuits, high voltage feed-through, UV transparent windows.

The detector anode is made of 50 μm thick Kapton foil with 1152 hexagonal pads printed on one side and short signal traces on the other side (pads and traces are made of 5 μm thick copper), in one single piece (140×63 cm^2). It also serves as an additional gas

seal. Plated through holes connect the pads to the signal traces.

Special tooling and jigs were developed and used during all phases of the construction to meet the tight mechanical tolerance of all subcomponents of the order of 0.1 mm and to achieve 0.5 mm clearance between adjacent photon detector modules. No mechanical problems were found during the vessel construction and detector assembly.

Special attention was paid to minimization of the material budget, to keep the multiple scattering to a minimum and to reduce the amount of conversions in the PHENIX central arm acceptance. With this design each box weights $\sim$5 kg. Adding all accessories results in a total weight of less then 10 kg. The radiation length of the vessel within the central arm acceptance is calculated to be 0.92%. The contribution of the 50 cm CF_4 gas is 0.54%, and the electronics constitute 1.88%, yielding a total radiation length of 3.34%.

One important requirement was the gas tightness of the box. Oxygen and water vapour absorb Čerenkov photons on their way through the radiator reducing the overall photo-electron yield. Every 10 ppm of either oxygen or water result in a loss of approximately 1 photoelectron in the 50 cm radiator length. Also water speeds up the CsI photo-cathodes aging rate. The measured leak rate for both arms of the detector was at the level of 0.1 cc/min, which is a very good result for a total volume of 311 liters.

5.5.2 Triple GEM detectors

All GEMs for the HBD were produced at CERN. The standard GEM foil 22×27 cm^2 in size is made of 50 μm thick Kapton, with 5 μm copper cladding on both sides. The gold plated GEM foils are of the same size, but have additional thin layers of nickel and gold on top of the copper layer. The gold coating prevents chemical interaction between the CsI and the copper, the nickel layer provides good adhesion of the gold layer. The GEMs are chemically pierced with 80 μm holes with a pitch of 150 μm. One of the GEM surfaces is divided into 28 strips (261×7.5 mm^2 each) to reduce the capacitance and energy stored in case of discharge. The mesh electrodes were made from a stainless steel woven wire mesh stretched and glued to a FR4 frame, same as for the GEMs. The mesh was subsequently cut around and the wire ends were covered with epoxy glue. The optical transparency of the mesh is 91%.

The mesh and the three GEMs are mounted on FR4 fiberglass frames. The frames have a width of 5 mm and a thickness of 1.5 mm that defines the inter-gap distance. Since the fiberglass frame is narrow and rather flexible, special tooling was developed to stretch the GEM foils and the mesh and to glue them onto the frames. To prevent saggita of the mesh and foils the frames have a cross-like 0.3 mm wide support. The three GEM foils and the mesh are stacked together and attached to the detector vessel by 8 pins.

The pins are located at the corners and the middle of the frame and maintain the frames undeformed under tension. With this GEM support design, the resulting total dead area within the central arm acceptance is calculated to be 6%.

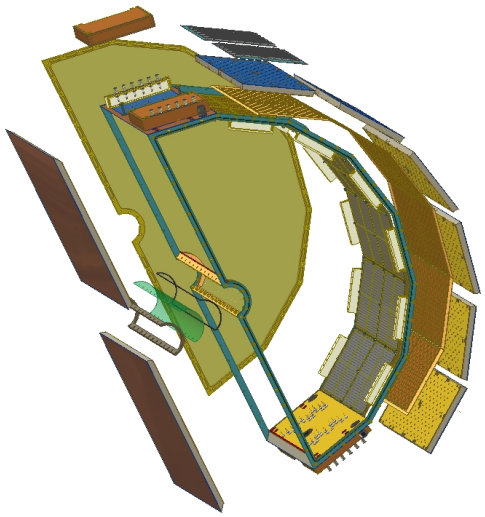

Figure 5.18: Exploded view of the HBD detector. One side cover is removed for clarity.

The GEM foils assembly, test and gain mapping were done at Weizmann Institute. All operations with the GEMs were performed either in a clean room (better than Class 100) or in a stainless steel test box. First, the foils were mechanically stretched on a special stretching device and then, while stretched, they were glued onto the FR4 frame with epoxy[1]. When the epoxy was cured, all excesses of Kapton foil were cut out, and a 20 MΩ SMD resistor was soldered to each HV segment. Quality control of the foil (measurement of the leakage current through the GEM) was performed at every step of the GEM preparation before framing, after framing and also after soldering the resistors. GEMs that passed the initial test in the clean room were individually tested up to 520 V in CF_4 atmosphere requiring the leakage current to be below 5 nA. Finally, a gain mapping of the GEMs was done in Ar/CO_2 with a ^{55}Fe X-ray source to measure the gas-gain variation across the foil, and the results were stored in a database. The last two tests were done in a stainless steel test box and success of these tests ensured that the GEM holds the necessary operating voltage and provided information about the gas-gain uniformity. Forty eight standard GEMs and twenty four gold plated GEMs combined in triplets in order to give the lowest possible gain variation for all modules were selected to be assembled in the detector. The resulting gain spread was found to be between 5% and 20% in all 24 modules.

[1]The epoxy used is Araldite AY-103/HY-991 from Huntsman Advanced Materials.

5.5.3 Photocathodes and electronics

The photocathodes for the HBD were produced at Stony Brook University [154] using a high vacuum evaporator system. The quantum efficiency of the photocathode was measured in situ inside the evaporator over the entire area of the GEM using a remote controlled movable UV light source and current monitor. All the produced photocathodes showed a quantum efficiency as high as in the R&D studies [150] with uniformity better than 5% across the entire area of the GEM.

The HBD is equipped with hybrid preamplifiers developed by the Instrumentation Division at BNL. This type of preamplifier produces a differential signal in the range from 0 to ± 1 V that is delivered to a receiver and front end module (FEM). The FEM contains a 12 bit, 65 MHz flash-ADC for each channel which digitizes the signal and sends the data via an optical G-Link to the PHENIX data acquisition system. The FEM and all digital electronics were designed and constructed by Nevis Laboratories.

5.6 HBD simulation

Detector simulation programs are an important tool during the design phase to develop a detector with optimal parameters. When the final detector is taking data the simulations become essential for understanding the data and to optimize performance. The PHENIX standard simulation package, PISA, is based on the GEANT3 [113] package. The final HBD design has been integrated into PISA, as shown in Fig. 5.19. Almost every detail is included in the detector description. However, some simplifications are used in the materials which are not active detecting elements or are outside the fiducial PHENIX acceptance.

The output of the PISA package, referred also as a ”hit file”, contains information about the hits in each subsystem in 3D space. For the HBD, only information about the hits produced by photons in the CsI photocathode layer and by charged tracks in the thin gas layer above the photocathodes is stored. The hit file is later processed by a second stage package which converts hits into simulated detector signals. For each charged particle hit in the HBD the ionization charge is generated randomly according to the measured HBD response to mips (see Section 5.4.5), while each photon hit produces one electron with a probability equal to the product of the quantum efficiency (see Section 5.4.4), the mesh transparency (91%) and the opaqueness of the GEM (73%). The resulting primary charge is multiplied by the detector gain to get the charge seen by a pad and finally a realistic electronic noise contribution is added. After completing the second stage (hit-to-signal conversion) the HBD response to simulated event is available as a charge amplitude

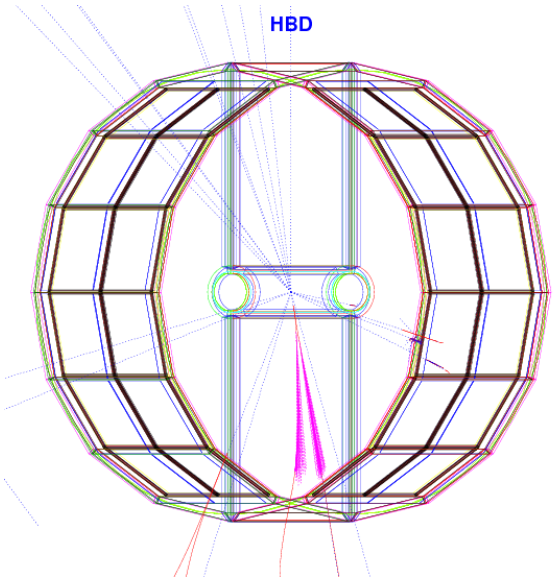

Figure 5.19: HBD as implemented in the PHENIX simulation package.

in every pad.

Several clustering and track-to-cluster association algorithms are now undergoing testing and optimization. The most straightforward of them builds clusters as follows. Pads with an amplitude greater than 2σ of its noise distribution are considered as fired pads. For each central arm track, a pad with an amplitude greater than 4σ of its noise distribution if found reasonably close (within $\sim$5 cm) to the track projection onto the HBD plane is tagged as the center of the HBD cluster. Fired pads, adjacent to the center of the cluster, are added to this cluster. After the pass over all central arm tracks in the event is completed, each group of adjacent fired pads that remained unassociated to any of the previously built clusters constitutes a new cluster.

5.7 Gas gain calibration

An extremely critical factor in the operation of gaseous detectors and of the HBD in particular is the gas gain. The scintillation in CF_4 provides a precise and very convenient method to measure the detector gas gain. Scintillation photons should produce single pad hits in the HBD not belonging to any track from the central arms in forward bias as well as in reverse bias modes. Fig. 5.20 shows the pulse height spectra of hits satisfying this requirement. It is clearly seen that the pulse height distribution in the forward bias mode have two different components: a fast exponential distribution due to scintillation photons and a slow exponential distribution due to charged particles. As one expects, in reverse mode mode the signal from charged particles is strongly suppressed, while the signal from

scintillation photons survives entirely. Using a high statistics run one can extract the gas gain for every pad from the pulse height distribution collected in the pad.

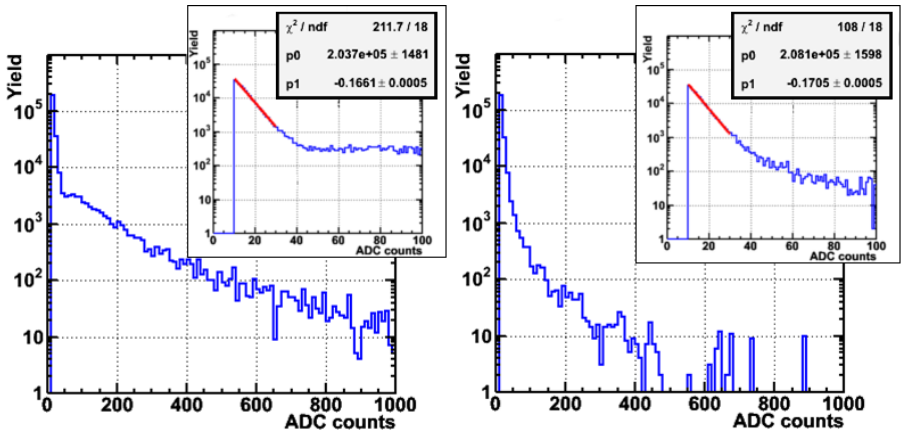

Figure 5.20: Pulse height distributions for single pads not belonging to tracks measured in forward bias (left) and reverse bias (right) modes. Inserts show the same distributions zoomed into the low amplitudes. The red solid lines in the inserts represent fits to an exponential distribution of the measured spectra.

If we assume that the number of scintillation photons per pad follows a Poisson distribution $P(n) = \frac{\mu^n e^{-\mu}}{n!}$, then the average number of photons $\langle m \rangle$ seen by a pad is given by: $\langle m \rangle = \frac{\sum_{n=1}^{\infty} nP(n)}{\sum_{n=1}^{\infty} P(n)} = \frac{\mu}{1-P(0)} = \frac{\mu}{1-e^{-\mu}}$, where $P(0) = e^{-\mu}$ is the probability to have no hit in a pad. The gain value is then given by: $1/(S \cdot \langle m \rangle)$, where S is the slope parameter of the fast component seen in the pulse height distribution of single pad hits. If properly corrected for multiple photon hits in a pad the gain should be independent of the event multiplicity. For small values of μ, the average number of scintillation photons per pad is given by: $\langle m \rangle = \frac{\mu}{1-e^{-\mu}} \approx 1 + \frac{\mu}{2} = 1 - \frac{\ln(P(0))}{2}$. The probability for no hit, $P(0)$, cannot be directly measured because pads with amplitude below a preset threshold are not recorded in the output data stream. Instead, we can measure the probability to have no hit in a pad for several values of the pad threshold and extrapolate to zero threshold. The measurement of the average gain of one of the HBD modules is illustrated in Fig. 5.21. The left panel shows pulse height distributions for single pads not belonging to tracks collected from samples of events having different track multiplicities. One sees that higher multiplicity events yield steeper pulse height distributions. The solid lines represent exponential fits to the pulse height distributions. The middle panel shows the probability to have no hit in a pad as a function of pad threshold for the same samples of events as in the left panel. The solid lines are polynomial fits used to extrapolate the measured probability trend to zero pad threshold. The right panel shows the non-corrected gain, determined as $1/S$, (solid circles) together with the corrected gain, determined as $1/(S \cdot \langle m \rangle)$, (open circles) as a function of event multiplicity. As one can see the corrected gain is independent of

the event multiplicity, as it was initially expected.

In the most peripheral events the probability to have multiple photon hits in one pad is small, and $1/S$ gives a good approximation of the gain.

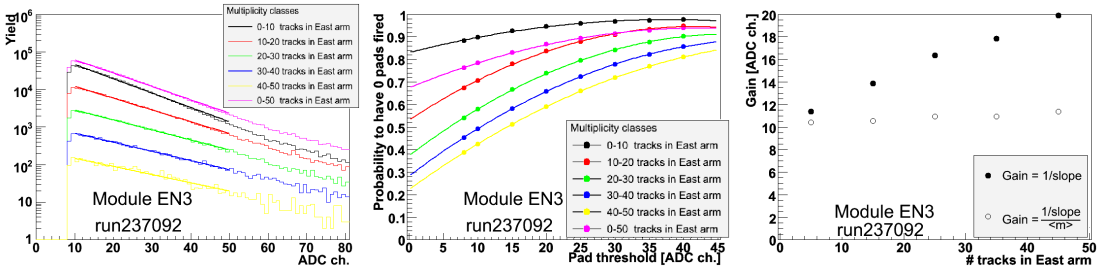

Figure 5.21: Pulse height distributions for single pads not belonging to tracks (left), probability to have no hit in a pad as a function of pad threshold (middle), detector gain for different centrality classes defined by the number of central arm tracks (right).

5.8 First results from the HBD

The HBD was first installed in PHENIX for Run-7 and underwent a series of commissioning studies aimed to test the new detector technology. During the run, the GEM stacks had difficulty holding the projected voltage, which was traced down to insufficient cleanliness of the final assembly procedure of the GEMs inside the detector vessel . Additionally, a problem was discovered with the high voltage system that resulted in releasing more than the expected amount of stored energy during a discharge, causing damage to many of the GEMs. For the details see [155]. Only the East arm of the HBD was operated during Run-7.

The entire HBD was rebuilt in 2008. A significant fraction of the damaged GEMs was successfully recuperated by washing with deionized water, others were replaced by spare ones. With the improved assembly procedure, the detector was rebuilt under much cleaner conditions. Furthermore, the resistive chain powering scheme was modified to eliminate the damage of powerful discharges. The HBD was reinstalled in PHENIX at the end of 2008 and used in Run-9 for physics. Currently only a small fraction (less than 10%) of the data collected in Run-9 has been analyzed. Preliminary results obtained so far [156] reveal performance comparable to that anticipated: we observe 20 photoelectrons per incident electron traversing the HBD, single electron efficiency close to 90% and significant improvement of at least a factor of 20 in the signal-to-background ratio for the measurements of the low-mass e^+e^- continuum.

Appendix A

Systematic errors summary on p_T spectra

All uncertainties are given in percents.

p_T (GeV/c)	1.1	1.45	1.95	2.45	2.95	3.45	3.95	4.45	5.5	7.0
acceptance	6.5	4.0	4.0	4.0	4.0	4.0	4.0	4.0	4.0	4.0
acceptance variation	3.0	2.0	2.0	2.0	2.0	2.0	2.0	2.0	2.0	2.0
yield extr. (MB)	8.0	8.0	8.0	7.0	7.0	7.0	7.0	8.0	20.0	25.0
yield extr. (sim)	3.0	3.0	3.0	3.0	3.0	3.0	3.0	3.0	3.0	3.0
momentum scale	0.5	0.6	1.1	1.8	2.4	3.0	3.6	4.0	4.7	5.0
trigger	9.6	9.6	9.6	9.6	9.6	9.6	9.6	9.6	9.6	9.6
trigger bias	2.5	2.5	2.5	2.5	2.5	2.5	2.5	2.5	2.5	2.5
branching ratio	1.2	1.2	1.2	1.2	1.2	1.2	1.2	1.2	1.2	1.2
Total error	15.0	13.9	13.9	13.5	13.6	13.7	13.8	14.5	23.5	27.9

Table A.1: p+p: Systematic errors summary.

p_T (GeV/c)	1.45	1.95	2.45	2.95	3.45	3.95	4.45	5.1
acceptance	4.0	4.0	4.0	4.0	4.0	4.0	4.0	4.0
acceptance variation	2.0	2.0	2.0	2.0	2.0	2.0	2.0	2.0
yield extr. (MB)	22.0	20.6	17.0	16.0	16.0	16.7	18.0	20.0
yield extr. (sim)	3.0	3.0	3.0	3.0	3.0	3.0	3.0	3.0
momentum scale	1.0	1.5	2.0	2.5	3.0	3.5	4.0	4.6
trigger	7.8	7.8	7.8	7.8	7.8	7.8	7.8	7.8
trigger bias	1.0	1.0	1.0	1.0	1.0	1.0	1.0	1.0
branching ratio	1.2	1.2	1.2	1.2	1.2	1.2	1.2	1.2
Total error	24.0	22.8	19.6	18.8	18.9	19.6	20.8	22.7

Table A.2: d+Au: Systematic errors summary.

p_T (GeV/c)	1.1	1.45	1.95	2.45	2.95	3.45	3.95	4.45	5.5	7.0
acceptance	4.5	4.5	4.5	4.0	4.0	4.0	4.0	4.0	4.0	4.0
acceptance variation	6.0	6.0	6.0	2.0	2.0	2.0	2.0	2.0	2.0	2.0
yield extr. (MB)	10.2	10.2	10.2	12.0	11.0	11.0	10.0	10.0	9.0	9.0
yield extr. (0-10%)	12.4	12.4	12.4	18.0	17.0	15.0	13.0	12.0	11.0	9.0
yield extr. (10-20%)	10.3	10.3	10.3	17.3	17.0	14.9	14.2	13.6	13.4	12.2
yield extr. (20-30%)	9.7	9.7	9.7	15.7	15.7	14.6	14.9	14.6	15.0	14.5
yield extr. (30-40%)	9.4	9.4	9.4	14.0	14.0	14.0	15.0	15.0	16.0	16.0
yield extr. (40-50%)	9.1	9.1	9.1	12.3	12.2	13.2	14.5	14.7	16.3	16.6
yield extr. (50-60%)	9.0	9.0	9.0	10.4	10.4	12.1	13.3	13.9	15.9	16.3
yield extr. (60-92%)	9.0	9.0	9.0	6.0	7.0	9.0	9.0	10.0	13.0	13.0
yield extr. (sim)	3.0	3.0	3.0	2.0	2.0	2.0	2.0	2.0	2.0	2.0
momentum scale	0.5	0.6	1.1	1.8	2.4	3.0	3.6	4.0	4.7	5.0
embedding (MB)	4.0	4.0	4.0	3.0	3.0	3.0	3.0	3.0	3.0	3.0
embedding (0-10%)	7.0	7.0	7.0	7.0	7.0	7.0	7.0	7.0	7.0	7.0
embedding (10-20%)	3.5	3.5	3.5	3.5	3.5	3.5	3.5	3.5	3.5	3.5
embedding (20-30%)	3.0	3.0	3.0	3.0	3.0	3.0	3.0	3.0	3.0	3.0
embedding (30-40%)	3.0	3.0	3.0	3.0	3.0	3.0	3.0	3.0	3.0	3.0
embedding (40-50%)	1.0	1.0	1.0	1.0	1.0	1.0	1.0	1.0	1.0	1.0
embedding (50-60%)	1.0	1.0	1.0	1.0	1.0	1.0	1.0	1.0	1.0	1.0
embedding (60-92%)	1.0	1.0	1.0	1.0	1.0	1.0	1.0	1.0	1.0	1.0
branching ratio	1.2	1.2	1.2	1.2	1.2	1.2	1.2	1.2	1.2	1.2
Total error (MB)	13.7	13.7	13.7	13.5	12.7	12.8	12.1	12.3	11.7	11.9

Table A.3: Au+Au: Systematic errors summary.

Appendix B

Determination of the systematic uncertainties in $\frac{dN}{dy}$

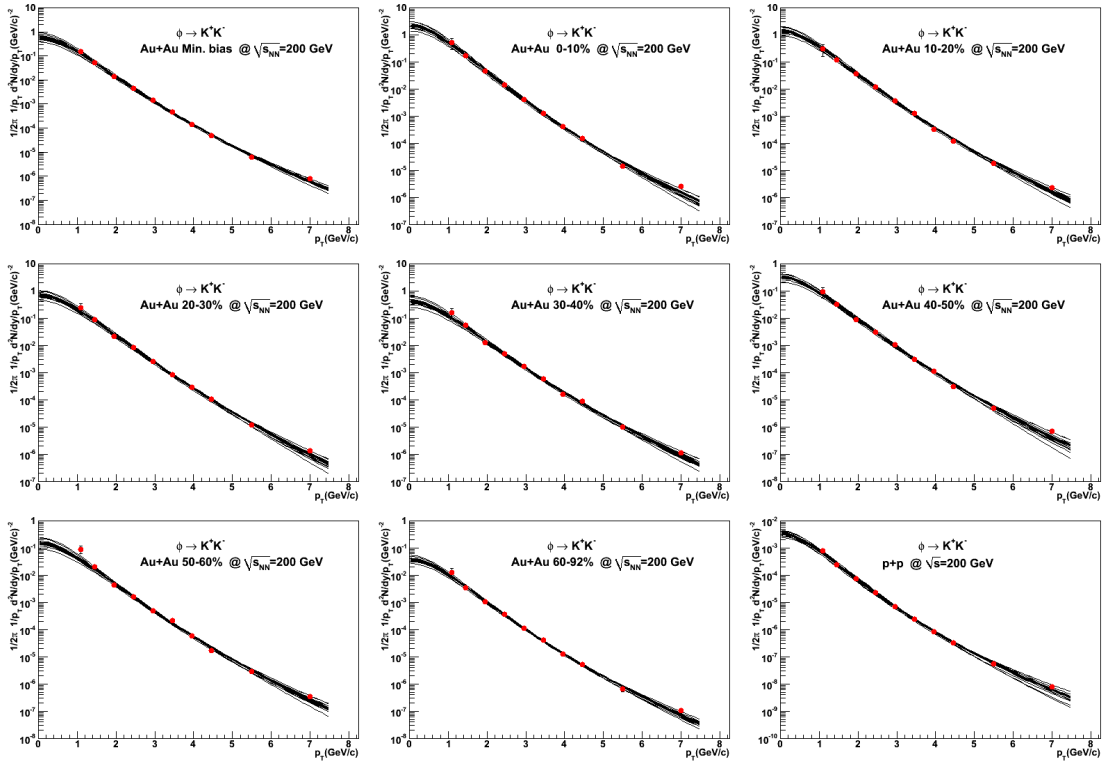

Figure B.1: Fits of the ϕ meson spectra with the Levy distribution of Eq. 4.1 for 20 data points variation trials. Red points are measured data.

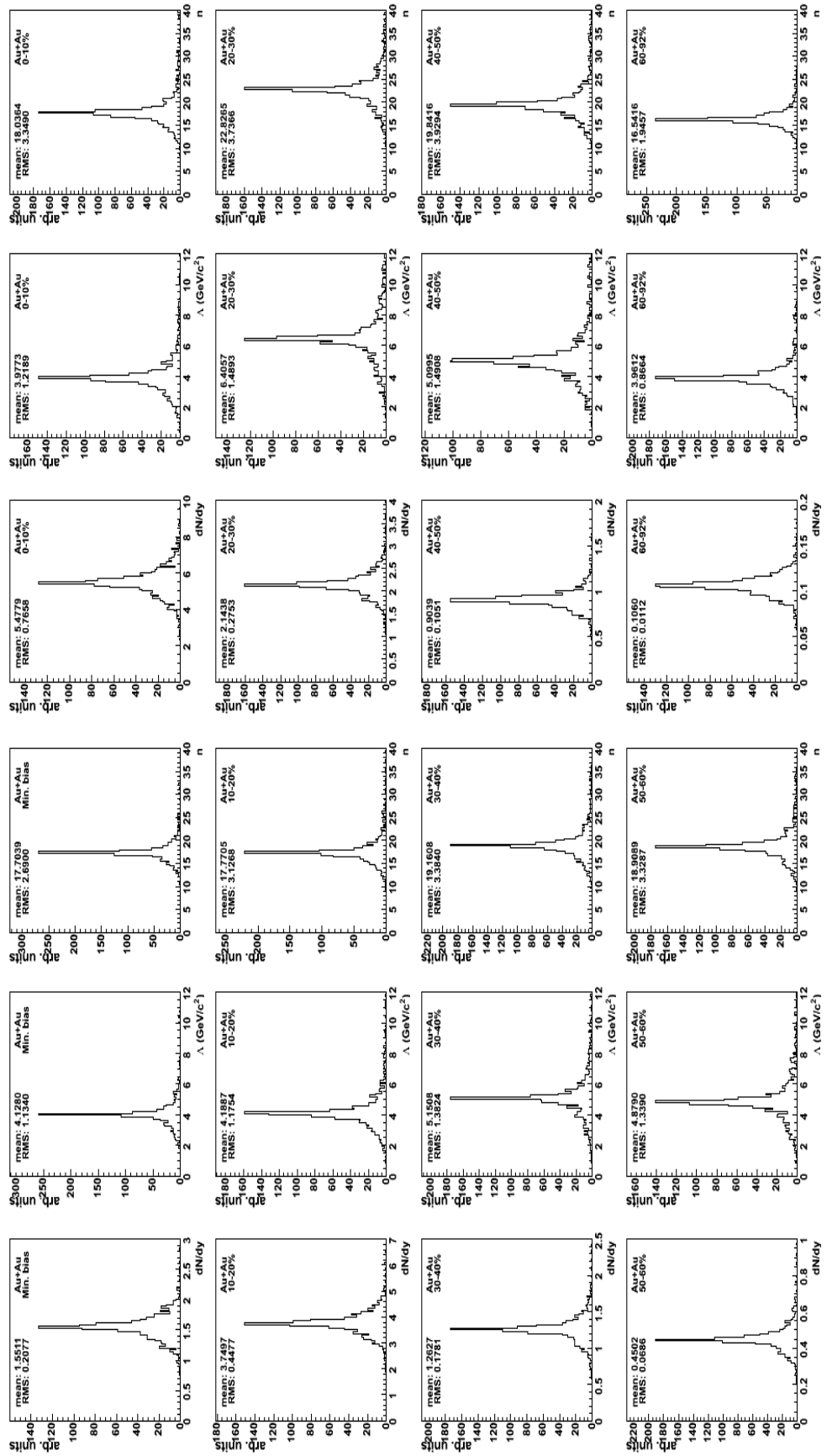

Figure B.2: Distributions of the Levy fit parameters after 1000 random data points variations.

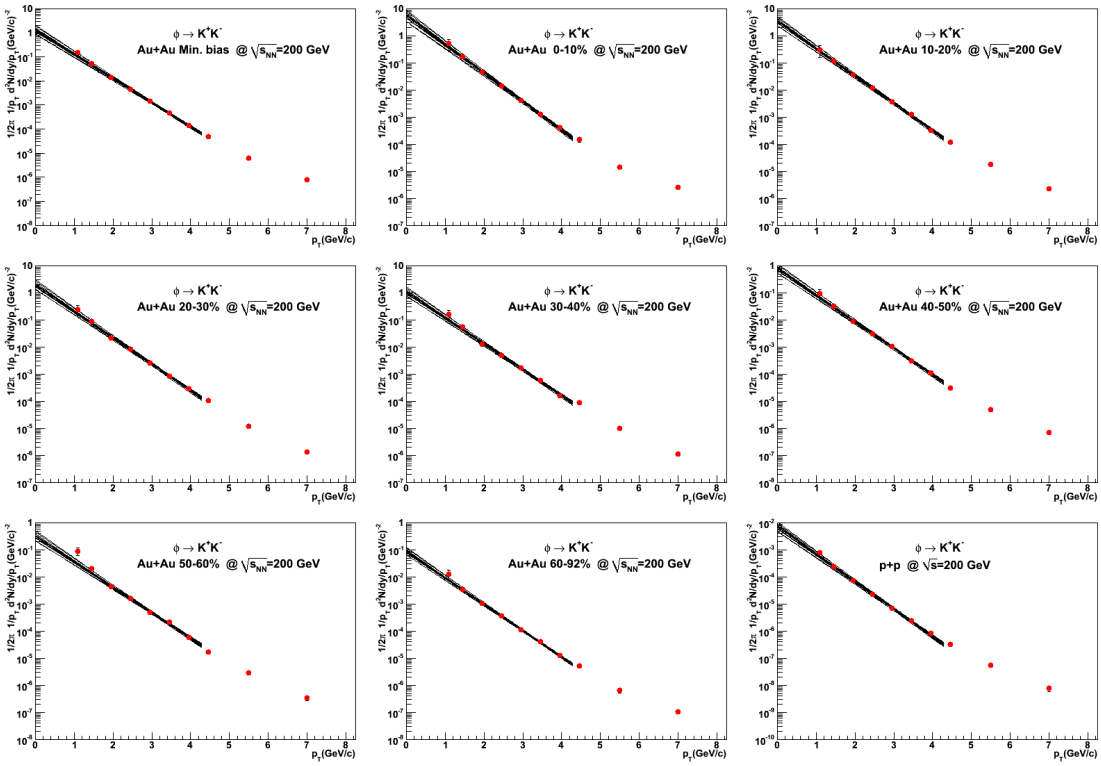

Figure B.3: Fits of the ϕ meson spectra with the p_T-exponential distribution of Eq. 4.2a for 20 data points variation trials. Red points are measured data.

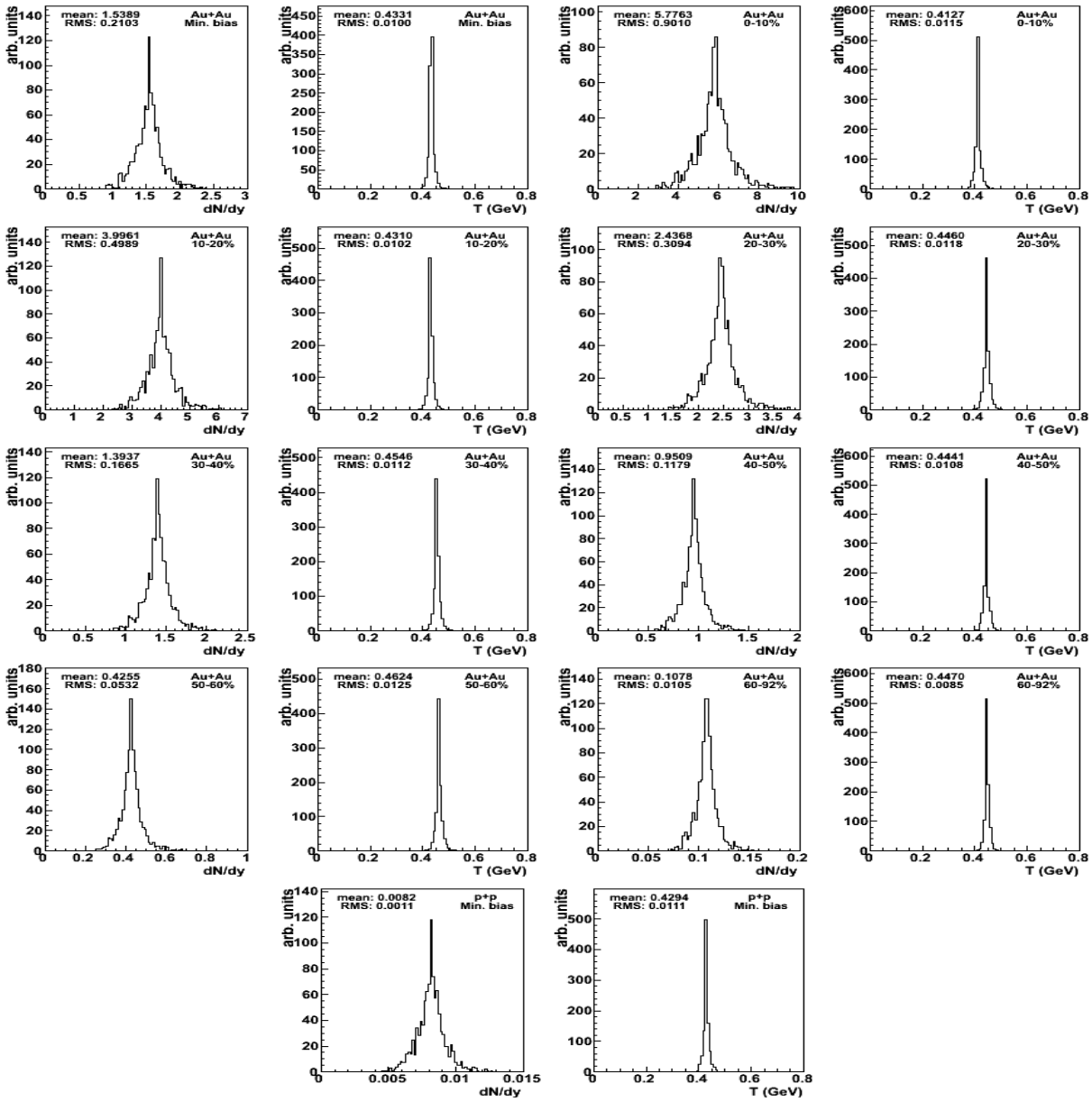

Figure B.4: Distributions of the p_T-exponential fit parameters after 1000 random data points variations.

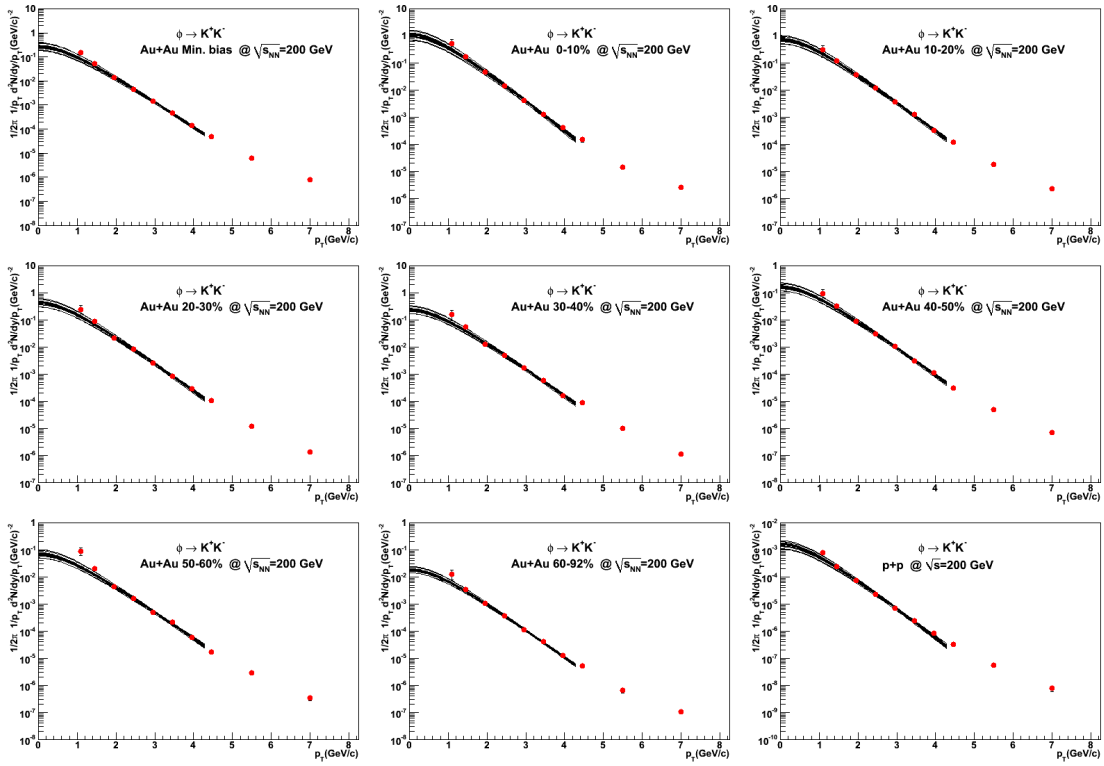

Figure B.5: Fits of the ϕ meson spectra with the m_T-exponential distribution Eq. 4.2b for 20 data points variation trials. Red points are measured data.

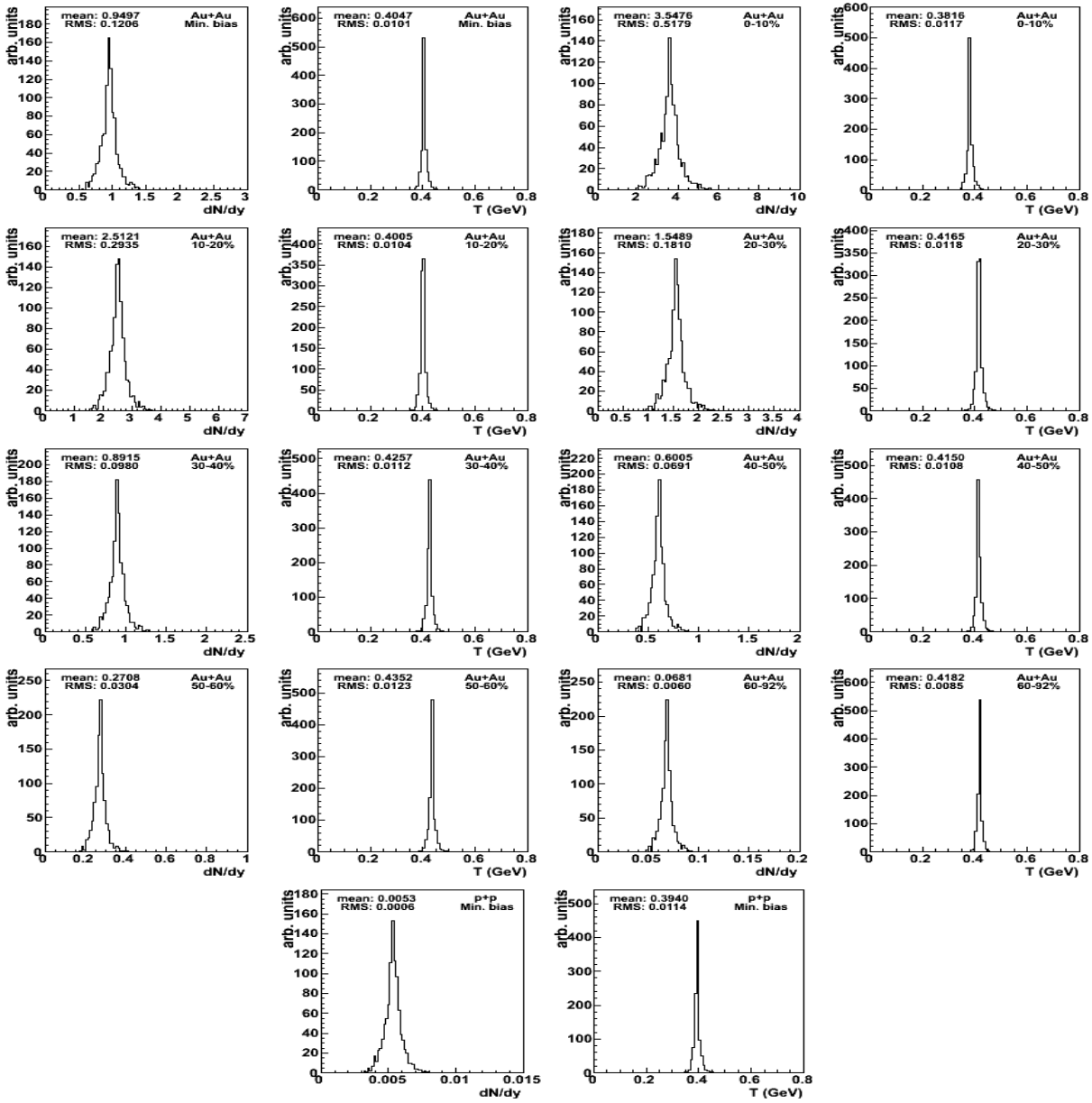

Figure B.6: Distributions of the m_T-exponential fit parameters after 1000 random data points variations.

Event class	dN/dy			
	fit range: 0.0−7.2 GeV/c	fit range: 1.2−7.2 GeV/c	fit range: 0.0−6.0 GeV/c	fit range: 0.0−5.0 GeV/c
Au+Au Min. bias	1.55±0.12(stat)	1.53±0.12(stat)	1.30±0.11(stat)	1.29±0.13(stat)
Au+Au 0-10%	5.47±0.93(stat)	5.36±0.94(stat)	4.61±0.81(stat)	4.92±1.10(stat)
Au+Au 10-20%	3.75±0.47(stat)	3.75±0.48(stat)	3.15±0.44(stat)	2.81±0.42(stat)
Au+Au 20-30%	2.14±0.27(stat)	2.11±0.27(stat)	1.93±0.26(stat)	2.02±0.35(stat)
Au+Au 30-40%	1.26±0.17(stat)	1.23±0.17(stat)	1.13±0.17(stat)	1.17±0.24(stat)
Au+Au 40-50%	0.90±0.12(stat)	0.89±0.12(stat)	0.77±0.11(stat)	0.68±0.10(stat)
Au+Au 50-60%	0.45±0.07(stat)	0.42±0.07(stat)	0.40±0.071(stat)	0.39±0.09(stat)
Au+Au 60-92%	0.106±0.014(stat)	0.103±0.014(stat)	0.091±0.014(stat)	0.091±0.016(stat)
p+p Min. bias	0.0082±0.0005(stat)	0.0073±0.0005(stat)	0.0080±0.0006(stat)	0.0080±0.0006(stat)

Table B.1: dN/dy extracted from the Levy fits with Eq. 4.1 to the ϕ meson spectra for different fitting ranges.

Event class	dN/dy			
	fit range: 0.0−3.6 GeV/c	fit range: 0.0−4.3 GeV/c	fit range: 0.0−5.0 GeV/c	fit range: 1.2−4.3 GeV/c
Au+Au Min. bias	1.53±0.09(stat)	1.55±0.08(stat)	1.52±0.07(stat)	1.53±0.08(stat)
Au+Au 0-10%	5.97±0.81(stat)	5.80±0.71(stat)	5.55±0.66(stat)	5.71±0.72(stat)
Au+Au 10-20%	3.82±0.39(stat)	3.99±0.36(stat)	3.98±0.34(stat)	3.99±0.36(stat)
Au+Au 20-30%	2.52±0.26(stat)	2.44±0.22(stat)	2.38±0.20(stat)	2.42±0.22(stat)
Au+Au 30-40%	1.26±0.14(stat)	1.40±0.13(stat)	1.28±0.11(stat)	1.38±0.13(stat)
Au+Au 40-50%	0.97±0.10(stat)	0.95±0.09(stat)	0.98±0.08(stat)	0.95±0.09(stat)
Au+Au 50-60%	0.41±0.05(stat)	0.43±0.04(stat)	0.45±0.04(stat)	0.42±0.04(stat)
Au+Au 60-92%	0.106±0.011(stat)	0.108±0.009(stat)	0.102±0.008(stat)	0.107±0.009(stat)
p+p Min. bias	0.0085±0.0004(stat)	0.0082±0.0003(stat)	0.0080±0.0003(stat)	0.0078±0.0003(stat)

Table B.2: dN/dy extracted from the p_T-exponential fits with Eq. 4.2a to the ϕ meson spectra for different fitting ranges.

Event class	dN/dy			
	fit range: 0.0−3.6 GeV/c	fit range: 0.0−4.3 GeV/c	fit range: 0.0−5.0 GeV/c	fit range: 1.2−4.3 GeV/c
Au+Au Min. bias	0.97±0.05(stat)	0.95±0.04(stat)	0.93±0.04(stat)	0.95±0.04(stat)
Au+Au 0-10%	3.73±0.43(stat)	3.56±0.38(stat)	3.40±0.35(stat)	3.51±0.38(stat)
Au+Au 10-20%	2.48±0.22(stat)	2.52±0.20(stat)	2.48±0.18(stat)	2.51±0.20(stat)
Au+Au 20-30%	1.63±0.14(stat)	1.55±0.12(stat)	1.50±0.11(stat)	1.54±0.12(stat)
Au+Au 30-40%	0.84±0.08(stat)	0.89±0.07(stat)	0.82±0.06(stat)	0.89±0.07(stat)
Au+Au 40-50%	0.63±0.05(stat)	0.60±0.05(stat)	0.61±0.04(stat)	0.60±0.05(stat)
Au+Au 50-60%	0.27±0.03(stat)	0.27±0.02(stat)	0.28±0.02(stat)	0.27±0.02(stat)
Au+Au 60-92%	0.069±0.006(stat)	0.068±0.005(stat)	0.064±0.004(stat)	0.068±0.005(stat)
p+p Min.bias	0.0056±0.0005(stat)	0.0054±0.0002(stat)	0.0052±0.0002(stat)	0.0051±0.0002(stat)

Table B.3: dN/dy extracted from the m_T-exponential fits with Eq. 4.2b to the ϕ meson spectra for different fitting ranges.

Appendix C

Publications that include results from this work

1. M. Naglis. *Anomalous ϕ meson suppression in Au+Au collisions at $\sqrt{s_{NN}} = 200$ GeV measured by the PHENIX experiment at RHIC.*, Nucl. Phys. A830, 757-760 (2009)

2. M. Naglis. *Measurement of light mesons at RHIC by the PHENIX experiment.*, Eur. Phys. J., C61, 835-840 (2009).

3. Z. Fraenkel et al. (including M. Naglis). *A Hadron Blind Detector for the PHENIX experiment at RHIC*, Nucl. Instrum. Meth. A546, 466 (2005)

4. PHENIX Collaboration. *Nuclear effects in production of ϕ meson in p+p, d+Au, Cu+Cu and Au+Au collisions at $\sqrt{s_{NN}} = 200$ GeV.*, in preparation (M. Naglis is chair of the paper preparation committee)

5. PHENIX Collaboration. *Measurement of ϕ meson in p+p, d+Au and Au+Au collisions at $\sqrt{s_{NN}} = 200$ GeV*, in preparation (M. Naglis is a member of the paper preparation committee)

6. PHENIX Collaboration. *Scaling properties of particle production in p+p collisions at $\sqrt{s} = 200$ GeV.*, in preparation (M. Naglis is a member of the paper preparation committee)

7. I. Ravinovich et al. (including M. Naglis). *A hadron blind detector for the PHENIX experiment at RHIC.*, Nucl. Phys. A774, 903 (2006)

8. A. Milov et al. (including M. Naglis). *Construction and expected performance of the Hadron Blind Detector for the PHENIX experiment at RHIC.*, J. Phys., G34, S701 (2007)

9. W. Anderson et al. (including M. Naglis). *Understanding the gain characteristics of GEMs inside the Hadron Blind Detector in PHENIX.*, IEEE Nuclear Science Symposium Conference Record NSS'07, 6, 4662-4665 (2007)

10. C. Y. Chi et al. (including M. Naglis). *A faster digitizer system for the Hadron Blind Detector in PHENIX.*, IEEE Nuclear Science Symposium Conference Record NSS'07, 3, 1997-2000 (2007)

11. C. Woody et al. (including M. Naglis). *Prototype Tests and Construction of the Hadron Blind Detector for the PHENIX Experiment.*, IEEE Nuclear Science Symposium Conference Record, NSS'06, 3, 1557-1561 (2006)

12. I. Tserruya et al. (including M. Naglis). *A Hadron Blind Detector for the PHENIX experiment at RHIC.*, IEEE Nuclear Science Symposium Conference Record NSS'04, 2, 1137-1141 (2004)

References

[1] M. Gell-Mann. *The eightfoldway: A theory of strong interaction symmetry.* Cornell preprint CTSL-20, unpublished, 1961. 1.1

[2] Y. Ne'eman. *Derivation of strong interactions from a gauge invariance*. Nucl. Phys., **26** (1961) 222–229. 1.1

[3] M. Gell-Mann. *A schematic model of baryons and mesons*. Phys. Lett., **8** (1964) 214–215. 1.1

[4] G. Zweig. *An SU(3) model for strong interaction symmetry and its breaking.* CERN preprint TH-412, unpublished, 1964. 1.1, 1.4

[5] J. J. Aubert et al. *Experimental Observation of a Heavy Particle J*. Phys. Rev. Lett., **33** (1974) 1404–1406. 1

[6] J. E. Augustin et al. *Discovery of a Narrow Resonance in e^+e^- Annihilation*. Phys. Rev. Lett., **33** (1974) 1406–1408. 1

[7] S. W. Herb et al. *Observation of a dimuon resonance at 9.5-GeV in 400-GeV proton - nucleus collisions*. Phys. Rev. Lett., **39** (1977) 252–255. 1

[8] F. Abe et al. *Observation of top quark production in $p\bar{p}$ collisions*. Phys. Rev. Lett., **74** (1995) 2626–2631. 1

[9] S. Abachi et al. *Observation of the top quark*. Phys. Rev. Lett., **74** (1995) 2632–2637. 1

[10] H. Fritzsch, M. Gell-Mann, and H. Leutwyler. *Advantages of the Color Octet Gluon Picture*. Phys. Lett., **B47** (1973) 365–368. 1.1

[11] R. Brandelik et al. *Evidence for Planar Events in e+ e- Annihilation at High-Energies*. Phys. Lett., **B86** (1979) 243. 1.1

[12] Frithjof Karsch. *Lattice QCD at high temperature and density*. Lect. Notes Phys., **583** (2002) 209–249. 1.1

[13] Edward V. Shuryak. *Quantum chromodynamics and the theory of superdense matter*. Phys. Rept., **61** (1980) 71–158. 1.1

[14] W. Weise. *Nuclear aspects of chiral symmetry*. Nucl. Phys., **A553** (1993) 59c–72c. 1.2, 1.3.2

[15] DOE/NSF Nuclear Science Advisory Committee. *The Frontiers of Nuclear Science: A Long-Range Plan for the Next Decade*, 2007. http://www.sc.doe.gov/np/nsac/docs/Nuclear-Science.Low-Res.pdf. 1.3

[16] Z. Fodor and S. D. Katz. *Finite T/mu lattice QCD and the critical point*. Prog. Theor. Phys. Suppl., **153** (2004) 86–92. 1.1

[17] Shinji Ejiri et al. *Study of QCD thermodynamics at finite density by Taylor expansion*. Prog. Theor. Phys. Suppl., **153** (2004) 118–126. 1.1

[18] P. F. Kolb. *Expansion rates at RHIC*. Heavy Ion Phys., **21** (2004) 243–248. 1.2

[19] K. Yagi, T. Hatsuda, and Y. Miake. *Quark-gluon plasma: From big bang to little bang*. Camb. Monogr. Part. Phys. Nucl. Phys. Cosmol., **23** (2005) 1–446. 1.4

[20] Johann Rafelski and R. Hagedorn. *From Hadron Gas to Quark Matter. 2*. Invited talk given at Int. Symp. on Statistical Mechanics of Quarks and Hadrons, Bielefeld, West Germany Aug 24-31, 1980. 1.3.1

[21] Johann Rafelski and Berndt Muller. *Strangeness Production in the Quark - Gluon Plasma*. Phys. Rev. Lett., **48** (1982) 1066. 1.3.1, 1.4

[22] Johann Rafelski. *Strangeness Production in the Quark Gluon Plasma*. Nucl. Phys., **A418** (1984) 215c–235c. 1.3.1

[23] John B. Kogut and D. K. Sinclair. *Simulating SU(3) Gauge Theory with a Realistic Quark Spectrum: Strangeness Production in Heavy Ion Collisions*. Phys. Rev. Lett., **60** (1988) 1250–1253. 1.3.1

[24] B. I. Abelev et al. *Enhanced strange baryon production in Au+Au collisions compared to p+p at sqrt(s_{NN})= 200 GeV*. Phys. Rev., **C77** (2008) 044908. 1.3.1, 1.5, 4.2.3

[25] Michael K. Mitrovski et al. *Strangeness production at SPS energies*. J. Phys., **G32** (2006) S43–S50. 1.3.1

[26] E. Andersen et al. *Strangeness enhancement at mid-rapidity in Pb Pb collisions at 158 A GeV/c*. Phys. Lett., **B449** (1999) 401–406. 1.3.1

[27] G. E. Bruno. *NA57 main results*. J. Phys., **G35** (2008) 044005. 1.3.1

[28] A. Tounsi, A. Mischke, and K. Redlich. *Canonical aspects of strangeness enhancement*. Nucl. Phys., **A715** (2003) 565–568. 1.3.1

[29] A. Tounsi and K. Redlich. *Strangeness enhancement and canonical suppression*. (2007). arXiv:hep-ph/0111159. 1.3.1

[30] Johann Rafelski. *Strange and hot matter*. Nucl. Phys., **A544** (1992) 279–292. 1.3.1

[31] Masashi Kaneta and Nu Xu. *Centrality Dependence of Chemical Freeze-out in Au+Au Collisions at RHIC*. (2007). arXiv:nucl-th/0405068. 1.3.1

[32] J. Goldstone. *Field Theories with Superconductor Solutions*. Nuovo Cim., **19** (1961) 154–164. 1.3.2

[33] R. Rapp and J. Wambach. *Chiral symmetry restoration and dileptons in relativistic heavy-ion collisions*. Adv. Nucl. Phys., **25** (2000) 1. 1.6

[34] Michael C. Birse. *Chiral symmetry in nuclei: Partial restoration and its consequences*. J. Phys., **G20** (1994) 1537–1576. 1.3.2

[35] G. E. Brown and Mannque Rho. *Chiral restoration in hot and/or dense matter*. Phys. Rept., **269** (1996) 333–380. 1.3.2

[36] G. E. Brown and M. Rho. *Scaling effective Lagrangians in a dense medium*. Phys. Rev. Lett., **66** (1991) 2720–2723. 1.3.2

[37] T. Hatsuda and S. H. Lee. *QCD sum rules for vector mesons in nuclear medium*. Phys. Rev., **C46** (1992) 34–38. 1.3.2

[38] R. Arnaldi et al. *First measurement of the rho spectral function in high- energy nuclear collisions*. Phys. Rev. Lett., **96** (2006) 162302. 1.3.2

[39] D. Adamova et al. *Modification of the rho meson detected by low-mass electron-positron pairs in central Pb-Au collisions at 158 A GeV/c*. Phys. Lett., **B666** (2008) 425–429. 1.3.2

[40] Xin-Nian Wang and Miklos Gyulassy. *Gluon shadowing and jet quenching in A + A collisions at s**(1/2) = 200-GeV*. Phys. Rev. Lett., **68** (1992) 1480–1483. 1.3.3

[41] R. Baier, D. Schiff, and B. G. Zakharov. *Energy loss in perturbative QCD*. Ann. Rev. Nucl. Part. Sci., **50** (2000) 37–69. 1.3.3

[42] M. Gyulassy, P. Levai, and I. Vitev. *Non-Abelian energy loss at finite opacity*. Phys. Rev. Lett., **85** (2000) 5535–5538. 1.3.3

[43] M. Gyulassy, P. Levai, and I. Vitev. *Reaction operator approach to non-Abelian energy loss*. Nucl. Phys., **B594** (2001) 371–419. 1.3.3

[44] Urs Achim Wiedemann. *Gluon radiation off hard quarks in a nuclear environment: Opacity expansion*. Nucl. Phys., **B588** (2000) 303–344. 1.3.3

[45] Miklos Gyulassy and Xin-nian Wang. *Multiple collisions and induced gluon Bremsstrahlung in QCD*. Nucl. Phys., **B420** (1994) 583–614. 1.3.3

[46] R. Baier, Yuri L. Dokshitzer, Alfred H. Mueller, S. Peigne, and D. Schiff. *Radiative energy loss of high energy quarks and gluons in a finite-volume quark-gluon plasma*. Nucl. Phys., **B483** (1997) 291–320. 1.3.3

[47] R. Baier, Yuri L. Dokshitzer, Alfred H. Mueller, and D. Schiff. *Radiative energy loss of high energy partons traversing an expanding QCD plasma*. Phys. Rev., **C58** (1998) 1706–1713. 1.3.3

[48] K. Adcox et al. *Formation of dense partonic matter in relativistic nucleus nucleus collisions at RHIC: Experimental evaluation by the PHENIX collaboration*. Nucl. Phys., **A757** (2005) 184–283. 1.7

[49] John Adams et al. *K*(892) resonance production in Au + Au and p + p collisions at s(NN)**(1/2) = 200-GeV at STAR*. Phys. Rev., **C71** (2005) 064902. 1.8, 1.3.3, 4.2

[50] K. Adcox et al. *Suppression of hadrons with large transverse momentum in central Au + Au collisions at s**(1/2)(N N) = 130-GeV*. Phys. Rev. Lett., **88** (2002) 022301. 1.3.3

[51] K. Adcox et al. *Centrality dependence of the high p(T) charged hadron suppression in Au + Au collisions at s(NN)**(1/2) = 130- GeV*. Phys. Lett., **B561** (2003) 82–92. 1.3.3

[52] Stephen Scott Adler et al. *Common suppression pattern of eta and pi0 mesons at high transverse momentum in Au + Au collisions at s(NN)**(1/2) = 200-GeV*. Phys. Rev. Lett., **96** (2006) 202301. 1.3.3, 4.3.1

[53] Stephen Scott Adler et al. *Suppressed pi0 production at large transverse momentum in central Au + Au collisions at s(NN)**(1/2) = 200-GeV*. Phys. Rev. Lett., **91** (2003) 072301. 1.3.3

[54] Stephen Scott Adler et al. *High p_T charged hadron suppression in Au + Au collisions at $\sqrt{s_{NN}} = 200$ GeV*. Phys. Rev., **C69** (2004) 034910. 1.3.3

[55] John Adams et al. *Transverse momentum and collision energy dependence of high p(T) hadron suppression in Au + Au collisions at ultrarelativistic energies*. Phys. Rev. Lett., **91** (2003) 172302. 1.3.3

[56] B. B. Back et al. *Charged hadron transverse momentum distributions in Au + Au collisions at s(NN)**(1/2) = 200-GeV*. Phys. Lett., **B578** (2004) 297–303. 1.3.3

[57] Stephen Scott Adler et al. *Absence of suppression in particle production at large transverse momentum in s(NN)**(1/2) = 200-GeV d + Au collisions*. Phys. Rev. Lett., **91** (2003) 072303. 1.3.3

[58] I. Arsene et al. *Transverse momentum spectra in Au + Au and d + Au collisions at s(NN)**(1/2) = 200-GeV and the pseudorapidity dependence of high p(T) suppression*. Phys. Rev. Lett., **91** (2003) 072305. 1.3.3

[59] B. B. Back et al. *Centrality dependence of charged hadron transverse momentum spectra in d + Au collisions at s(NN)**(1/2) = 200-GeV*. Phys. Rev. Lett., **91** (2003) 072302. 1.3.3

[60] John Adams et al. *Evidence from d + Au measurements for final-state suppression of high p(T) hadrons in Au + Au collisions at RHIC*. Phys. Rev. Lett., **91** (2003) 072304. 1.3.3

[61] Klaus Reygers. *Characteristics of Parton Energy Loss Studied with High-p_T Particle Spectra from PHENIX*. J. Phys., **G35** (2008) 104045. 1.3.3, 4.3.1, 4.17

[62] Stephen Scott Adler et al. *Centrality dependence of direct photon production in s(NN)**(1/2) = 200-GeV Au + Au collisions*. Phys. Rev. Lett., **94** (2005) 232301. 1.3.3

[63] Stephen Scott Adler et al. *Scaling properties of proton and anti-proton production in s(NN)**(1/2) = 200-GeV Au + Au collisions*. Phys. Rev. Lett., **91** (2003) 172301. 1.3.3

[64] Stephen Scott Adler et al. *High transverse momentum η meson production in p+p, d+Au and Au+Au collisions at s(NN)**(1/2) = 200-GeV*. Phys. Rev., **C75** (2007) 024909. 1.3.3, 2.6

[65] A. Adare et al. *Suppression pattern of neutral pions at high transverse momentum in Au+Au collisions at sqrt(s_{NN}) = 200 GeV and constraints on medium transport coefficients*. Phys. Rev. Lett., **101** (2008) 232301. 1.3.3, 4.3.1, 4.17

[66] B. I. Abelev et al. *Identified baryon and meson distributions at large transverse momenta from Au + Au collisions at s(NN)**(1/2) = 200-GeV*. Phys. Rev. Lett., **97** (2006) 152301. 1.3.3

[67] John Adams et al. *Particle dependence of azimuthal anisotropy and nuclear modification of particle production at moderate p(T) in Au + Au collisions at s(NN)**(1/2) = 200-GeV*. Phys. Rev. Lett., **92** (2004) 052302. 1.3.3

[68] W. M. Yao *et.al. Review of particle physics*. J. Phys., **G33** (2006) 1–1232. 1.1, 3.5

[69] P. L. Connolly et al. *Existence and Properties of the Phi Meson*. Phys. Rev. Lett., **10** (1963) 371–376. 1.4

[70] S. Okubo. *ϕ meson and unitary symmetry model*. Phys. Lett., **5** (1963) 165–168. 1.4

[71] J. Iizuka. *Systematics and phenomenology of meson family*. Prog. Theor. Phys. Suppl., **37** (1966) 21–34. 1.4

[72] P. Koch, B. Muller, and J. Rafelski. *Strangeness in Relativistic Heavy Ion Collisions*. Phys. Rept., **142** (1986) 167–262. 1.4

[73] A. Shor. *Phi meson production as a probe of the Quark Gluon Plasma*. Phys. Rev. Lett., **54** (1985) 1122–1125. 1.4, 4.2.3

[74] Itzhak Tserruya. *Electromagnetic Probes*. (2009). arXiv:0903.0415. 1.4

[75] D. Lissauer and Edward V. Shuryak. *K meson modification in hot hadronic matter may be detected via Phi meson decays*. Phys. Lett., **B253** (1991) 15–18. 1.4

[76] S. Pal, C. M. Ko, and Zi-wei Lin. *Phi meson production in relativistic heavy ion collisions*. Nucl. Phys., **A707** (2002) 525–539. 1.4

[77] Stephen Scott Adler et al. *Production of Phi mesons at mid-rapidity in s**(1/2)(NN) = 200-GeV Au + Au collisions at RHIC*. Phys. Rev., **C72** (2005) 014903. 1.4, 1.10, 4.2.1, 4.8, 4.9

[78] Maxim Naglis. *Anomalous ϕ Meson Suppression in Au+Au Collisions at $\sqrt{s_{NN}}$=200 GeV Measured by the PHENIX Experiment at RHIC*. (2009). arXiv:0907.4461. 1.5, 4.3.3

[79] Alexander Kozlov. *Phi production as seen in e+ e- and K+ K- decay channels in Au + Au collisions by PHENIX at s(NN)**(1/2) = 200- GeV*. Nucl. Phys., **A774** (2006) 739–742. 1.5, 4.2.2

[80] Alberica Toia. *e+e- Pairs: a clock and a thermometer of heavy ion collisions*. J. Phys., **G35** (2008) 104037. 1.5

[81] M. Harrison, T. Ludlam, and S. Ozaki. *RHIC project overview*. Nucl. Instr. and Meth., **A499** (2003) 235–244. 2.1

[82] K. H. Ackermann et al. *STAR detector overview*. Nucl. Instrum. Meth., **A499** (2003) 624–632. 2.1

[83] B. B. Back et al. *The PHOBOS detector at RHIC*. Nucl. Instrum. Meth., **A499** (2003) 603–623. 2.1

[84] M. Adamczyk et al. *The BRAHMS experiment at RHIC*. Nucl. Instrum. Meth., **A499** (2003) 437–468. 2.1

[85] K. Adcox et al. *PHENIX detector overview*. Nucl. Instrum. Meth., **A499** (2003) 469–479. 2.1, 5.1

[86] K. Adcox et al. *PHENIX central arm tracking detectors*. Nucl. Instrum. Meth., **A499** (2003) 489–507. 2.2

[87] K. Ikematsu et al. *A start-timing detector for the collider experiment PHENIX at RHIC-BNL*. Nucl. Instrum. Meth., **A411** (1998) 238–248. 2.3.1

[88] M. Allen et al. *PHENIX inner detectors*. Nucl. Instrum. Meth., **A499** (2003) 549–559. 2.3.1

[89] Clemens Adler et al. *The RHIC zero degree calorimeters*. Nucl. Instrum. Meth., **A470** (2001) 488–499. 2.3.1

[90] R. J. Glauber. *Cross-sections in deuterium at high-energies*. Phys. Rev., **100** (1955) 242–248. 2.3.2

[91] Beat Hahn, D. G. Ravenhall, and Robert Hofstadter. *High-energy electron scattering and the charge distributions of selected nuclei*. Phys. Rev., **101**(3) (1956) 1131–1142. 2.3.2

[92] M. L. Miller, K. Reygers, S. J. Sanders, and P. Steinberg. *Glauber modeling in high energy nuclear collisions*. Ann. Rev. Nucl. Part. Sci., **57** (2007) 205–243. 2.3.2, 4.3.3

[93] V. G. Ryabov. *Drift chambers for the PHENIX central tracking system*. Nucl. Instrum. Meth., **A419** (1998) 363–369. 2.4.1

[94] K. Adcox et al. *Construction and performance of the PHENIX pad chambers*. Nucl. Instrum. Meth., **A497** (2003) 263–293. 2.4.1

[95] J. T. Mitchell et al. *Event reconstruction in the PHENIX central arm spectrometers*. Nucl. Instrum. Meth., **A482** (2002) 491–512. 2.4.2, 3.6

[96] M. Aizawa et al. *PHENIX central arm particle ID detectors*. Nucl. Instrum. Meth., **A499** (2003) 508–520. 2.5, 1

[97] S. Van der Meer. *Calibration of the effective beam height in the ISR*, 1968. CERN Int. Report ISR-P0/68-31. Available at:http://ccdb4fs.kek.jp/cgi-bin/img_index?196800064;. 2.6

[98] Stephen Scott Adler et al. *Mid-rapidity neutral pion production in proton proton collisions at* $\sqrt{s} = 200GeV$. Phys. Rev. Lett., **91** (2003) 241803. 2.6

[99] A. Adare et al. *Inclusive cross section and double helicity asymmetry for* π^0 *production in p+p collisions at* $\sqrt{s} = 200$ *GeV: Implications for the polarized gluon distribution in the proton*. Phys. Rev., **D76** (2007) 051106. 2.6

[100] Sebastian N. White. *Diffraction dissociation - 50 years later*. AIP Conf.Proc., **792** (2005) 527–531. 2.6

[101] S. R. Klein and R. Vogt. *Nuclear shadowing and high-p(T) hadron spectra in relativistic heavy ion collisions*. Phys. Rev., **C67** (2003) 047901. 2.6

[102] S. S. Adler et al. *PHENIX on-line systems*. Nucl. Instrum. Meth., **A499** (2003) 560–592. 2.7

[103] S. S. Adler et al. *PHENIX on-line and off-line computing*. Nucl. Instrum. Meth., **A499** (2003) 593–602. 2.7

[104] A. Campbell, T. Hemmick, A. Toia, A. Drees, T. Dahms, R. Averbeck, and B. Jacak. *Dielectron Mass Spectra in Cu+Cu Collisions at* $\sqrt{s_{NN}}$ *= 200 GeV*. (2007). PHENIX Internal Analysis Note 585. 3.3

[105] Mohammed Muniruzzman. *Phi Meson Production in Au-Au Collisions at 200 GeV Measured by the PHENIX Experiment at the Relativistic Heavy Ion Collider*. (2003). PhD thesis, University of California - Riverside, http://www.phenix.bnl.gov/WWW/publish/munir/Thesis/Thesis.ps.gz. 3.3

[106] G. I. Kopylov. *Like particle correlations as a tool to study the multiple production mechanism*. Phys. Lett., **B50** (1974) 472–474. 3.4.1

[107] D. Drijard, H. G. Fischer, and T. Nakada. *Study of event mixing and its application to the extraction of resonance signals*. Nucl. Instr. Meth., **A225** (1984) 367. 3.4.1

[108] D. L'Hote. *About Resonance signal extraction from multiparticle data: combinatorics and event mixing methods*. Nucl. Instrum. Meth., **A337** (1994) 544–556. 3.4.1

[109] Torsten Dahms. *Dilepton spectra in p+p and Au+Au collisions at RHIC*. (2008). PhD thesis, Stony Brook University, arXiv:0810.3040. 1

[110] A. Toia, T. Dahms, A. Drees, and T. Hemmick. *Combinatorial Background: Event Mixing and Normalization*. (2006). PHENIX Internal Analysis Note 495. 1

[111] M. Naglis, A. Dubey, Z. Fraenkel, A. Kozlov, I. Ravinovich, D. Sharma, and I. Tserruya. *Run-4 Au+Au* $\phi \rightarrow K^+K^-$. (2005). PHENIX Internal Analysis Note 416. 1

[112] S. S. Adler et al. *Systematic studies of the centrality and* $\sqrt{s_{NN}}$ *dependence of* $\frac{dE_T}{d\eta}$ *and* $\frac{dN_{ch}}{d\eta}$ *in heavy ion collisions at mid-rapidity*. Phys. Rev., **C71** (2005) 034908. 3

[113] *GEANT manual, v.3.2.1*. (1994). CERN program Library W5013. 3.6, 3.9, 5.6

[114] *HIJING event generator*. http://www-nsdth.lbl.gov/~xnwang/hijing. 3.6

[115] *PYTHIA event generator*. http://home.thep.lu.se/~torbjorn/Pythia. 3.6

[116] G. J. Gounaris and J. J. Sakurai. *Finite width corrections to the vector meson dominance prediction for rho* $\rightarrow$ *e+ e-*. Phys. Rev. Lett., **21** (1968) 244–247. 3.6.1

[117] C. Amsler et al. *Review of particle physics*. Phys. Lett., **B667** (2008) 1. 3.11

[118] G. Wilk and Z. Wlodarczyk. *On the interpretation of nonextensive parameter q in Tsallis statistics and Levy distributions*. Phys. Rev. Lett., **84** (2000) 2770. 4.2

[119] K. M. Kijima, Z. Fraenkel, S. Milov, M. Naglis, K. Ozawa, R. Seto, D. Sharma, K. Shigaki, I. Ravinovich, I. Tserruya, and Y. Tsuchimoto. *Final results on* $\omega/\phi \rightarrow e^+e^-$ *in Run5 p+p collisions at* $\sqrt{s}$ *= 200 GeV*. (2009). PHENIX Internal Analysis Note 825. 4.2, 4.2.2

[120] Stephen Scott Adler et al. *Identified charged particle spectra and yields in Au + Au collisions at s(NN)**(1/2) = 200-GeV*. Phys. Rev., **C69** (2004) 034909. 4.2.3, 4.11

[121] Stephen Scott Adler et al. *Nuclear effects on hadron production in d + Au and p + p collisions at* s_{NN}*(1/2) = 200-GeV*. Phys. Rev., **C74** (2006) 024904. 4.3, 4.3.1, 4.17, 4.3.2, 4.18

[122] J. W. Cronin et al. *Production of Hadrons with Large Transverse Momentum at 200-GeV and 300-GeV*. Phys. Rev. Lett., **31** (1973) 1426–1429. 4.3, 4.3.2

[123] J. W. Cronin et al. *Production of Hadrons with Large Transverse Momentum at 200-GeV, 300-GeV, and 400-GeV*. Phys. Rev., **D11** (1975) 3105. 4.3, 4.3.2

[124] D. Antreasyan et al. *Production of Hadrons at Large Transverse Momentum in 200- GeV, 300-GeV and 400-GeV p p and p n Collisions*. Phys. Rev., **D19** (1979) 764. 4.3, 4.3.2

[125] P. B. Straub et al. *Nuclear dependence of high x(t) hadron and high tau hadron pair production in p A interactions at s**(1/2) = 38.8- GeV*. Phys. Rev. Lett., **68** (1992) 452–455. 4.3, 4.3.2

[126] P. B. Straub et al. *Particle ratios of high x(t) hadrons in p A interactions at s**(1/2) = 38.8-GeV*. Phys. Rev., **D45** (1992) 3030–3037. 4.3, 4.3.2

[127] R. C. Hwa, (ed.) and X. N. Wang, (ed.). *Quark-gluon plasma. Vol. 3*. River Edge, USA: World Scientific (2004) 777 p. 4.3.1

[128] John C. Collins, Davison E. Soper, and George Sterman. *Factorization for Short Distance Hadron - Hadron Scattering*. Nucl. Phys., **B261** (1985) 104. 4.3.1

[129] David d'Enterria. *Jet quenching*. (2009). arXiv:0902.2011/nucl-ex. 4.3.1

[130] Urs Achim Wiedemann. *Theoretical overview QM '04*. J. Phys., **G30** (2004) S649–S658. 4.3.1

[131] R. J. Fries, Berndt Muller, C. Nonaka, and S. A. Bass. *Hadron production in heavy ion collisions: Fragmentation and recombination from a dense parton phase*. Phys. Rev., **C68** (2003) 044902. 4.3.1

[132] Rudolph C. Hwa and C. B. Yang. *Recombination of shower partons at high p(T) in heavy-ion collisions*. Phys. Rev., **C70** (2004) 024905. 4.3.1

[133] Rudolph C. Hwa and C. B. Yang. *Production of strange particles at intermediate pT in central Au+Au collisions at high energies*. Phys. Rev., **C75** (2007) 054904. 4.3.1

[134] V. Greco, C. M. Ko, and P. Levai. *Parton coalescence at RHIC*. Phys. Rev., **C68** (2003) 034904. 4.3.1

[135] V. Greco, C. M. Ko, and P. Levai. *Parton coalescence and antiproton/pion anomaly at RHIC*. Phys. Rev. Lett., **90** (2003) 202302. 4.3.1

[136] Stephen Scott Adler et al. *Centrality dependence of pi0 and eta production at large transverse momentum in* $\sqrt{s_{NN}} = 200$ *GeV d+Au collisions*. Phys. Rev. Lett., **98** (2007) 172302. 4.3.2, 4.18

[137] Stephen Scott Adler et al. *Production of omega mesons at large transverse momenta in p + p and d + Au collisions at* $\sqrt{s_{NN}} = 200$ *GeV*. Phys. Rev., **C75** (2007) 051902. 4.3.2, 4.18

[138] John W. Harris and Berndt Muller. *The search for the quark-gluon plasma*. Ann. Rev. Nucl. Part. Sci., **46** (1996) 71–107. 5.1

[139] S. A. Bass, M. Gyulassy, Horst Stoecker, and W. Greiner. *Signatures of quark-gluon-plasma formation in high energy heavy-ion collisions: A critical review*. J. Phys., **G25** (1999) R1–R57. 5.1

[140] Alberica Toia. *Measurement of low mass dielectron continuum in s(NN)**(1/2) = 200-GeV Au + Au collisions in the PHENIX experiment at RHIC*. Eur. Phys. J., **C49** (2007) 243–247. 5.1, 5.1

[141] Z. Fraenkel et al. *The PHENIX Collaboration. Technical Note* 391. http://www.phenix.bnl.gov/phenix/WWW/publish/tserruya/1-06-HBD-proposal.ps, 2001. 5.1, 5.2

[142] C. Aidala et al. *A hadron blind detector for PHENIX*. Nucl. Instrum. Meth., **A502** (2003) 200–204. 5.1

[143] B. Azmoun et al. *The PHENIX Collaboration. Technical Note* 415. http://www.phenix.bnl.gov/phenix/WWW/publish/tserruya/5-08-HBD-CDR/HBD-CDR.pdf, 2005. 5.1, 5.5.1

[144] F. Sauli. *GEM: A new concept for electron amplification in gas detectors*. Nucl. Instr. and Meth., **A386** (1997) 531–534. 5.2

[145] B. K. Singh, E. Shefer, A. Breskin, R. Chechik, and N. Avraham. *CsBr and CsI UV photocathodes: New results on quantum efficiency and aging*. Nucl. Instrum. Meth., **A454** (2000) 364–378. 5.3

[146] D. Mormann, A. Breskin, R. Chechik, and B. K. Singh. *On the efficient operation of a CsI-coated GEM photon detector*. Nucl. Instrum. Meth., **A471** (2001) 333–339. 5.3, 5.4.4

[147] Dirk Mörmann. *Study of novel gaseous photomultipliers for UV and visible light.* (2005). PhD thesis, Weizmann Institute of Science. 5.5

[148] Archana Sharma. *Properties of some gas mixtures used in tracking detectors*. (1998). 5.4.1

[149] A. Breskin, R. Chechik, and A. Buzulutskov. *GEM photomultiplier operation in CF-4*. Nucl. Instrum. Meth., **A483** (2002) 670–675. 5.4.1

[150] Z. Fraenkel *et.al. A hadron blind detector for the PHENIX experiment at RHIC*. Nucl. Instr. and Meth., **A546** (2005) 466–480. 5.4.2, 5.5.3

[151] B. Azmoun, N. Smirnov, S. P. Stoll, and C. L. Woody. *Test of a GEM detector in the PHENIX experiment at RHIC*. In *IEEE Nuclear Science Symposium Conference Record*, volume 1, 480–484, 2004. 5.4.2

[152] L. Landau. *On the energy loss of fast particles by ionization*. J. Phys. (USSR), **8** (1944) 201–205. 5.4.5

[153] D. S. Denisov. *On using CF-4 as a working gas for drift tubes*. Nucl. Instrum. Meth., **A306** (1991) 200–206. 5.4.5

[154] J. A. Kamin. *A hadron blind detector for the PHENIX experiment at RHIC*. Eur. Phys. J., **C49** (2007) 177–180. 5.5.3

[155] W. Anderson, B. Azmoun, C. Y. Chi, Z. Citron, A. Dubey, J. M. Durham, Z. Fraenkel, T. Hemmick, J. Kamin, A. Kozlov, A. Milov, M. Naglis, R. Pisani, I. Ravinovich, T. Sakaguchi, D. Sharma, A. Sickles, I. Tserruya, and C. Woody.

Understanding the gain characteristics of GEMs inside the Hadron Blind Detector in PHENIX. In *IEEE Nuclear Science Symposium Conference Record NSS '07*, volume 6, 4662–4665, 2007. 5.8

[156] PHENIX Collaboration. *PHENIX Beam Use Proposal for RHIC Run-10 and Run-11*. (2009). http://www.bnl.gov/npp/docs/pac0609/Phenix_RBUP09.pdf. 5.8